 doi:10.20944/preprints202210.0357.v1

Physical and chemical characteristics of dew and rain in north-west Africa with focus on Morocco: Past and future evolution (2005 – 2100)

M. Muselli[1,2], I. Lekouch[3], D. Beysens[2,4,*]

[1] Università di Corsica Pasquale Paoli, Avenue du 9 septembre, BP 52, 20250 Corte, France, marc.muselli@univ-corse.fr

[2] OPUR, 2 rue Verderet, 75016 Paris, France

[3] Department of Geography, Université du Québec à Montréal, Montréal, Québec H3C 3P8, Canada, lekouch.imad@uqam.ca

[4] Physique et Mécanique des Milieux Hétérogènes, CNRS, ESPCI Paris - PSL University, Sorbonne Université, Sorbonne Paris Cité, 10 rue Vauquelin, 75005 Paris, France, daniel.beysens@espci.fr

*: Corresponding author: Daniel Beysens, daniel.beysens@espci.fr

Abstract: In the context of global warming and reduction in fresh water availability is presented a study of the evolution of dew, rain and evapotranspiration in the NW of Africa. The time periods are concerned with the years 2005-2020, using existing data, and years 2020-2100, using the low and high emissions representative concentration pathway scenarios RCP 2.6/8.5 from the Cordex database.

A continuous decrease in rain precipitation is observed, on order of -14 mm.decade^{-1} for the more credible scenario RCP 8.5. The amplitude is maximum on the coast and on the foothills of Atlas. A clear decrease in dew yields is also observed along a NW/SE axis, strongly correlated with a corresponding decrease in relative humidity (up to 7%).

Chemical dew and rain data in the representative site of Mirleft correspond to the major cations $Na^+ > Ca^{2+} > Mg^{2+} > K^+$, similar to a local spring water. Concentrations in rain are about two times less than in dew water. Ionic concentrations are compatible with WHO standards. The seasonal variations of the ionic concentrations in dew and rain follow a volume dilution dependence. The expected diminution in dew and rain volumes according to the RCPs 2.6 and 8.5 should increase the dew and rain ionic concentrations in the future.

Keywords: dew rain evolution map; evapotranspiration evolution map; climate change; dew rain chemistry; northwestern Africa; Morocco

Preprints (www.preprints.org) | NOT PEER-REVIEWED | Posted: 24 October 2022 doi:10.20944/preprints202210.0357.v1

1. Introduction

North Africa is considered a hot spot for climate change. North West Africa (Morocco, Canaria islands, West Algeria) is an area highly vulnerable to extreme precipitation events [1]. Schilling et al. [2] demonstrated the vulnerability of this part of the world with regard to proven climate change. The combination of climate change and strong population growth is very likely to further aggravate the already scarce water situation. In Morocco, Schilling et al. [3] show that precipitation is likely to decrease by 2050 between 10 and 20%, while temperatures are likely to rise between 2 and 3°C. Terink et al. [4] considered this part of Africa as the most water-scarce region of the World. With 9 global circulation models, they investigated two meteorological future periods up to 2050 by comparison with the current climate. The simulations exhibited a large decrease of yearly precipitation for the majority of the country by 15-20%.

Over the whole of its territory, Morocco receives a yearly rainfall of 140 billion m^3. The potential of water resources is estimated at 22 billion m^3, divided into 18 billion m^3 of inputs in surface water and 4 billion m^3 of groundwater. This corresponds to around 700 m^3/inhabitant/year, which places Morocco in a situation of structural water stress [5]. According to [6], climate change and water resource scarcity can lead to population conflicts or migration in the near future. This region presents a particular challenge [7] with regards to transboundary or – cascading – climate risks, particularly given its high levels of water stress (and the importance of water in several key sectors and systems in the region).

In contrast, dew water exhibits a frequent occurrence in many geographical locations. It is indeed less constrained by specific climatological and geographic conditions than other meteorological phenomena like fog [8]. It is mostly dependent on certain common atmospheric conditions frequently found in Morocco during night, such as high relative humidity, low wind speed and little cloud cover facilitating efficient radiative cooling of the earth surface and the adjacent air (see e.g. [9-10]).

The first studies concerning dew (with rain and fog) were carried out in Morocco by [11]. Dew, fog and rain collection systems were implemented in the southwestern Morocco (Mirleft and Id Ouasskssou), a representative site of arid environment, during one year (May 1, 2007 to April 30, 2008). They have demonstrated the interest of passive radiative cooling to extract water from the atmospheric air. The dew potential resource was extrapolated in several cities throughout Morocco during the dry season (May-October 2008). The authors also carried out in the representative site of Mirleft the first chemical and biological study of dew and rain samples. They concluded to a large concentration of total dissolved solids in dew samples due to the deposition of marine salts and aerosols.

It is the object of this paper to study the evolution of dew, rain and evapotranspiration from either meteo data (rain, evapotranspiration) and calculations (dew) using a formulation [12] which needs only a few meteo data. The study deals firstly with the past period 2005-2020 using meteo data recorded on several sites, and secondly with the period 2020-2100, with data from two low and high emissions representative concentration pathway (RCP)

Preprints (www.preprints.org) | NOT PEER-REVIEWED | Posted: 24 October 2022 doi:10.20944/preprints202210.0357.v1

scenarios, RCP 2.6 and RCP 8.5 ([13-16]. They correspond to climate simulations from CNRM Météo-France model CM5-ALADIN63 downloaded from the Cordex database [17]. In order to serve as a reference for future studies dealing with the evolution of the chemical properties of dew and rain, chemical data of the representative site of Mirleft (Morocco) are also reported. They were obtained by [18] and analyzed differently, accounting particularly for future evolutions from the RCP predictive models.

The paper is organized as follows. After having detailed the methods used for evaluating the past and future rain, dew and evapotranspiration data, the results are presented and discussed; in particular maps are given concerning the volume and the frequency of dew and rain events. Evapotranspiration is also analyzed together with its evolution. A specific section is then devoted to chemistry of dew and rain.

2. Meteorological data and methods

2.1. Studied area

The study area (NW of Africa; Fig. 1) is characterized by Morocco and a part of desert and coastal Algeria. It represents about 710 850 km^2 between 20° to 36° north latitude and 0° to 17° for west longitude. According to [19], the country exhibits 8 different climates according to the Köppen-Geiger classification (Fig. 1). Both prevalent climates are arid hot desert (BWh) and temperate (Csa) with dry and hot summer. BWh climate is mainly located in the south-west and east of the country (Sahara Desert) while the Csa climate is located mainly in the north and north-west of Morocco. Next come the cold desert (BWk) on the highlands close to the border with Algeria and the hot arid steppe (BSh) near the Atlantic Ocean coast in the middle of the country. The Atlas Mountains are mainly marked by a cold dry and warm (Dsh) or cold (Dsc) summer. Finally, polar tundra (ET) is found at very high elevation.

Preprints (www.preprints.org) | NOT PEER-REVIEWED | Posted: 24 October 2022 doi:10.20944/preprints202210.0357.v1

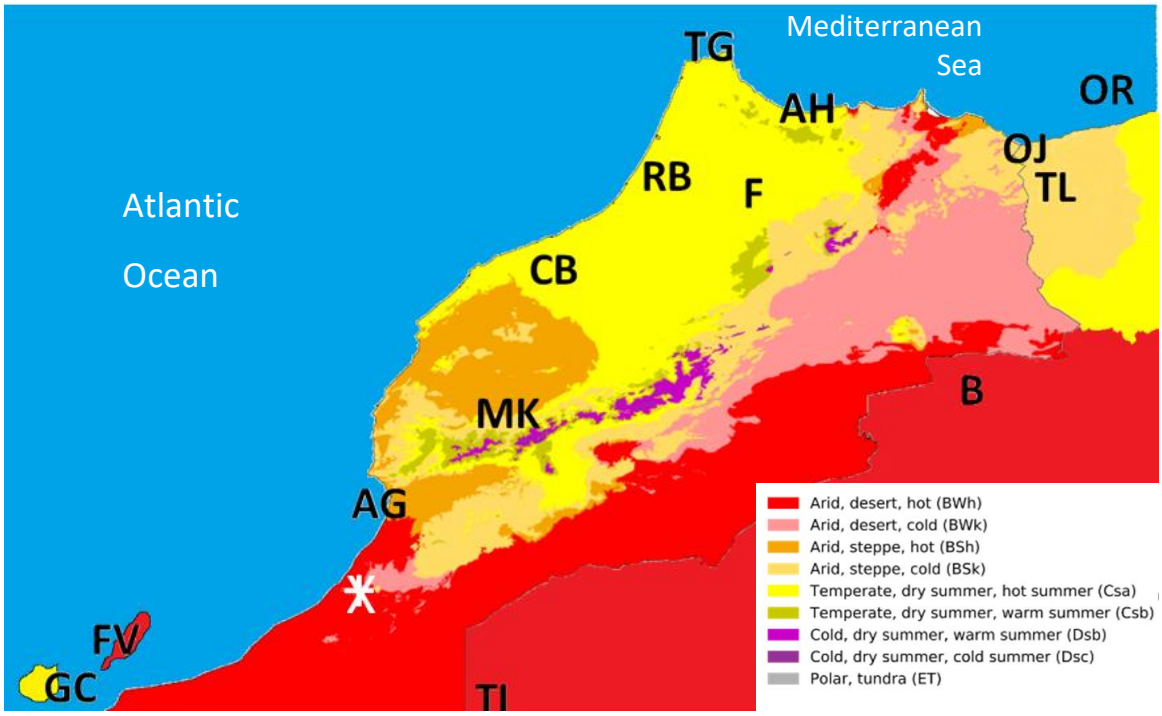

Figure 1. Köppen-Geiger climate classification map for the studied area concerning the period 1980-2016, from [19] and [20]. Meteo sites are indicated (see Table 1 for the abreviations). The figure does not show the entire arid desert region (BWh climate) located at the south of the country. Right and inclined crosses (very close) represent Mirleft and Id Ouasskssou dew measurement sites.

The climate is characterized by pronounced spatial and temporal differences in day and nighttime temperatures, humidity or rainfall. The plains in north Atlantic experience a Mediterranean climate with oceanic influence. Summer is dry and sunny, but this does not prevent the existence of dew at night, quite frequent during this period. The cumulative yearly precipitation ranges between 450 mm (Casablanca) to 810 mm (Tanger).

From Safi to the south of Agadir (Doukkala plain, Essaouira coast and the Souss basin), the climate is characterized by an increasing aridity when going south, due to the Sahara influence. The mean yearly cumulative rainfall is 400 mm in Safi, 300 mm in Essaouira and 270 mm in Agadir. The rainy period is less than six months and is mainly concentrated between November and March. On the North Atlantic coast, morning fogs and nightly dews are frequent. The number of clear, sunny days (200 per year in Agadir) is exceptionally high.

The highlands area forms a crescent stretching from Fez in the northeast to Marrakech in the southwest. It includes the plains and plateaus of Saïss, Chaouia, Abda and Haouz. The climate is essentially a degradation of the two previous climates with a relatively marked continentality. This area could be divided in two parts, a semi-arid region in the south and a more humid area in the north. Fès and Meknes receive between 500 and 600 mm of rain per year; this quantity drops drastically, below 350 mm, in south of Settat with in particular 280

Preprints (www.preprints.org) | NOT PEER-REVIEWED | Posted: 24 October 2022 doi:10.20944/preprints202210.0357.v1

mm in Marrakech. The continentality of this region has two consequences: low air humidity and important thermal amplitude both over the day and the year.

The Mediterranean coast and the Rif (with elevation over 2000 m asl) exhibits typically a Mediterranean climate on the coast with a mild winter (9-12 °C), moderately watered, coupled with a hot, dry summer (24-26 °C). In the hinterland reliefs, precipitations can reach a maximum of over 1500 mm per year with snow and cold temperatures in winter.

The Middle and High Atlas form a mountain range oriented south-west north-east, with elevation ranging from 2500 m to 4165 m. The highest point is Jebel Toubkal (4165 m), the highest peak in North Africa. It forms a barrier between a Mediterranean Morocco and a Morocco-Algeria desert. The climate is mountainous in the central part of the chain. If the Middle Atlas receives between 1000 and 1500 mm of precipitation on average per year, the High Atlas receives only 600 to 900 mm, or even less on the slopes (400-500 mm).

In the foothills of the Sahara of the Middle Atlas and the High Atlas, the climate is desert, with mountain influences given the elevation, as well as in the Anti-Atlas, which is the northernmost diversion of the Moroccan Atlas. The area receives between 100 and 200 mm of precipitation (120 mm in Ouarzazate). The average temperatures are much contrasted, between 6 and 11 °C in winter and 27 to 32 °C in summer. In Ouarzazate the minimum and maximum average temperatures are 1 °C and 17 °C, respectively, during the coldest winter month and 21 °C and 40 °C during the hottest summer months.

The Sahara Desert is located in the south of the Atlas Mountains. The climate is typically arid desert, with very rare precipitation, long and torrid summers, mild and pleasant winters. Rainfall is almost absent all year round, with much less than 100 mm per year (61 mm in Zagora, 59 mm in Merzouga, 33 mm in Dakhla). The average minimum and maximum temperatures are 3.8 °C and 20.8 °C, respectively, during the coldest month of winter and 25.7 °C and 44.3 °C during the hottest month of summer in Zagora, whose elevation is almost 700 m asl.

2.2. Data extraction

2.2.1 Measured data (years 2005-2020)

All weather stations used in this study are installed at international or national airports. Typical meteorological parameters are systematically measured according to the standards of the World Meteorological Organization. Air temperature (T_a, °C), relative humidity (RH, %), atmospheric pressure (P, Pa) are measured in a meteorological shelter, 1.5 m from the ground. Wind speed (V, km.h^{-1}, to be transformed in m.s^{-1}) and direction (sectors or degrees) are measured at 10 m from the ground.

Wind speed can be extrapolated at any height z above the ground by the classical logarithmic variation (see e.g. [21])

Preprints (www.preprints.org) | NOT PEER-REVIEWED | Posted: 24 October 2022 doi:10.20944/preprints202210.0357.v1

$$V_z = V_{10} \ln (z/z_c) / \ln (10/z_c) \quad (1)$$

where V_{10} is wind speed at 10 m and z_c is the roughness length where $V = 0$ (generally $z_c = 0.1$ m in flat areas like airports). Available data on 14 sites were extracted from the online database "Weather Underground" [22] during the period 2005-2020 (Table 1).

Country	Airport	Abbreviations	Köppen-Geiger climate	Lat	Long	Lat dec.	Long dec.	Alt (m)	Missing data (%)	Distance from the sea (km)
Spain	Gran Canaria	GC	Csa	27° 55′ 55″ N	15° 23′ 12″ W	27.932	-15.387	24	0.0	1
Spain	Fuerteventura	FV	BWh	28° 27′ 10″ N	13° 51′ 50″ W	28.453	-13.864	26	0.0	1
Morocco	Agadir	AG	BSh	30° 19′ 30″ N	9° 24′ 47″ W	30.325	-9.413	69	0.2	2
Algeria	Tindouf	TI	Csa	27° 42′ 00″ N	8° 10′ 00″ W	27.700	-8.167	443	0.1	275
Morocco	Marrakech	MK	BSh	31° 36′ 54″ N	8° 02′ 17″ W	31.615	-8.038	471	0.1	137
Morocco	Casablanca	CB	Csa	33° 22′ 05″ N	7° 35′ 17″ W	33.368	-7.588	200	0.2	1
Morocco	Rabat	RB	Csa	34° 03′ 04″ N	6° 45′ 05″ W	34.051	-6.751	84	0.1	4
Morocco	Tanger	TG	Csa	35° 43′ 43″ N	5° 55′ 01″ W	35.729	-5.917	19	0.2	4
Morocco	Fès	F	Csa	33° 55′ 39″ N	4° 58′ 41″ W	33.927	-4.978	579	0.4	134
Morocco	Al-Hoceima	AH	Csa	35° 10′ 37″ N	3° 50′ 23″ W	35.177	-3.840	27	0.7	1
Algeria	Béchar	B	Csa	31° 39′ 02″ N	2° 15′ 11″ W	31.651	-2.253	811	0.1	393
Morocco	Oujda	OJ	BSk	34° 47′ 15″ N	1° 55′ 26″ W	34.788	-1.924	468	0.2	44
Algeria	Tlemcen	TL	Csa	35° 00′ 55″ N	1° 27′ 03″ W	35.015	-1.451	248	0.0	27
Algeria	Oran	OR	Csa	35° 37′ 38″ N	0° 36′ 41″ W	35.627	-0.611	91	0.0	11

Table 1. Meteorological sites (airports) where atmospheric data are collected (8 stations in Morocco, 4 stations in Algeria and 2 stations in Spain) with typical climate and distance from the sea. They are sorted according to their longitude (west to east). The missing data fractions, in % of the total data, are also reported.

Dew yields have been computed from Eqs. 2-3 in section 2.3 with time period $\Delta t = 0.5$ h. for all sites except in Al-Hoceima / Béchar / Tindouf (1 h.) and Fès / Oujda where two time-steps are available (0.5 and 1 h.). The wind directions are computed from the sectors (N, NNE, NE, E, ESE, SE, S, etc.) by using a standard law of proportionality: 0° for north, 180° for south and calculation of all intermediate values with respect to these references. Cloud cover in oktas was computed from the observation of sky cover using the correspondence listed in Table 2 from national weather service glossary [23], as used in a previous work [24]. The rainfall data, available on a daily time-step, are extracted from the meteorological data base [25] at the stations reported in Table 1.

Preprints (www.preprints.org) | NOT PEER-REVIEWED | Posted: 24 October 2022 doi:10.20944/preprints202210.0357.v1

Observation	*N* (oktas)
CLR	0
FEW	1
SCT	3
BKN	5
OVC	8

Table 2. Correlation between sky observation and cloud cover according to [23]. The abbreviations for sky conditions are the following: CLR = Clear; FEW = few; SCT = Scattered; BKN = Broken; OVC = Overcast.

2.2.2 Climate model data CNRM-CM5/ALADIN63 (years 2006-2100)

Regional climate models (RCM) data are provided by the Cordex/Copernicus database [17]. Meteorological data are computed from a single level (earth surface). High resolution CNRM-ALADIN 63 Regional Climate Model coupled with the CNRM-CERFACS-CM5 Global Climate Model provides climate change information on regional and local scales in relatively fine detail. Gridded data present a 0.11° × 0.11° horizontal resolution (12.5 × 12.5 km²). Net CDF4 files with air temperature (T_a, K) and relative humidity (RH, %) at 2 m from the ground, wind speed (V, m.s^{-1}) at 10 m from the ground, mean precipitation flux (H_r, kg.m^{-2}.s^{-1}), orography (m), surface solar radiation downwards (W.m^{-2}) and total cloud cover (N, % of cloudy sky) are registered all 5 years (2006, 2010, 2015, …, 2100) with a 3 h. time step. The CORDEX climate projection uses RCP (Representative Concentration Pathways) forcing scenarios. The RCP hypothesis correspond to a variation in the radiative balance (difference between incoming and outgoing radiation) at the top of the troposphere (located between 10 and 16 km elevation), due to a change in one of the factors of climate change such as the concentration of greenhouse gases. In this study are considered RCP 2.6 (~ 3 W.m^{-2}, 490 ppm eq. CO_2) and RCP 8.5 (> 8.5 W.m^{-2}, > 1370 ppm eq. CO_2) extreme scenarios, thus providing two different pathways of the future climate forcing.

2.3. Dew yield estimation

In order to investigate the dew resource (mm), one uses the energy balance model [12]. This model allows daily or hourly dew yields to be computed from only a few classical meteorological data without adjustable parameters: Air temperature (T_a, °C), dew point temperature (T_d, °C), cloud cover (N, oktas), wind speed at 10 meters from the ground (V, m.s^{-1}). The results are concerned with the dew yield Δh (in mm) per unit time Δt (in h.), $\dot{h} = \Delta h/\Delta t$. The time Δt corresponds to the period of the analyzed data. It is assumed that the substrate is planar, tilted 30° from horizontal and thermally insulated from below. Its

Preprints (www.preprints.org) | NOT PEER-REVIEWED | Posted: 24 October 2022 doi:10.20944/preprints202210.0357.v1

emissivity is assumed to be unity (which is close to the emissivity ≈ 0.98 of a wet substrate during dew condensation, see [26]). The details of the formulation are as follows:

$$\dot{h} = \left(\frac{\Delta t}{12}\right)(HL + RE) \tag{2}$$

The data for $\dot{h} > 0$ correspond to condensation and $\dot{h} < 0$ to evaporation; the latter have to be discarded. The measurement period of the data in the present study is $\Delta t = 0.5$ or 1 h., depending on the stations. The quantity *HL* represents the convective heat losses between air and condenser, with a cut-off for wind speed $V > V_0 = 4.4$ m.s^{-1} where condensation vanishes:

$$\dot{h} = \begin{cases} \left(\frac{\Delta t}{12}\right)[0.06(T_d - T_a) + RE] & \text{if } V < V_0 \\ 0 & \text{if } V > V_0 \end{cases} \tag{3}$$

The quantity RE is the available radiative energy, which depends on air water content (measured by T_d, in °C), site elevation *H* (in km) and cloud cover *N* (in oktas):

$$RE = 0.37(1 + 0.204323H - 0.0238893H^2 - (18.0132 - 1.04963H + 0.21891H^2) \times 10^{-3}T_d)\left(\frac{T_d+273.15}{285}\right)^4(1 - \frac{N}{8}) \tag{4}$$

By filtering the data without rain or fog events and integrating the time series on a daily time-step corresponding to $\dot{h} > 0$, the calculated daily yields and their cumulated values can be readily obtained. When comparing the calculated values with the measurements, the agreement is better than 20-30% [12] [24], the deviation being mainly due to the unavoidable local differences in air flow geometries, which modify the convective heat exchange condenser/air.

2.4. Kriging maps

Kriging methodologies are mostly used for mapping spatial distribution of a given variable. The classical algorithm is presented in Appendix A. Tomaszkiewicz et al. [27] used ordinary Kriging to develop dew maps integrating projected climate changes in the Mediterranean basin. Martinez et al. [28] presented median polish Kriging (MPK) for space-time analysis of monthly precipitation in Colombia. Pue et al. [29] introduced a Kriging-based Gaussian process for the prediction of soil water retention in tropical and temperate climates. Muselli and Beysens [30] used kriging to study the biocrust sustainability with dew and rain

Preprints (www.preprints.org) | NOT PEER-REVIEWED | Posted: 24 October 2022 doi:10.20944/preprints202210.0357.v1

availability in southern Africa. Other studies combine Kriging models for the estimation of rainfall with Lagrangian approaches [31] or Bayesian [32].

2.5 Monthly evapotranspiration

Potential evapotranspiration *PET* is the water vapor flux under ideal conditions of complete ground cover by plants, uniform plant height and leaf coverage and suitable water supply. In order to estimate *PET* (mm.month^{-1}) for the studied area, the classical Turc's formulae were used [33]:

$$PET = \begin{cases} PET_{RH\geq 50\%} = 0.013\, J\, (R_g + 50)\left(\frac{T}{T+15}\right) \\ PET_{RH<50\%} = PET_{RH\geq 50\%}\left(1 + \frac{50-RH}{70}\right) \end{cases} \quad (5)$$

Here, for the considered month, *J* corresponds to the number of days, *T* is the mean ambient temperature of the month (°C), *RH* is the relative humidity and R_g is the mean daily horizontal solar radiation (cal.cm^{-2}.day^{-1}).

Actual evapotranspiration (*ET*) is the sum of water evaporation and transpiration to the atmosphere from a surface area. Evaporation and transpiration occur simultaneously and there is no easy way of distinguishing between the two processes. Apart from the water availability in the top soil, the evaporation from a cropped soil is mainly determined by the fraction of the solar radiation reaching the soil surface. This fraction decreases over the growing period as the crop develops and the crop canopy shades more and more of the ground area. When the crop is of small size, water is predominately lost by soil evaporation, but once the crop is well developed and completely covers the soil, transpiration becomes the main process.

To determine *ET*, one needs to define at the beginning of the year the useful reserve of the soil (UR_{base}, mm). *UR* varies each month, one thus needs a reference or base value taken the first month of the year. The latter is obtained by the classical equations of Rawls [34]:

$$UR_{base} = (W330 - W15000) \times H_g \quad (6)$$

Here H_g is the prospecting soil horizon thickness. The quantity *W*330 is defined as the water content in mm.m^{-1} for the predefined soil suction -330 hPa and *W*15000 is the water content for -15000 hPa. With a relatively low coarse element content, i.e. 49.5% sand (*Sa*, %), 1.2% of organic material (*MO*, %) and with a fine element of 17% clay (*Ar*, %), the equations are:

Preprints (www.preprints.org) | NOT PEER-REVIEWED | Posted: 24 October 2022 doi:10.20944/preprints202210.0357.v1

$$\begin{cases} W330 = 257.6 - (2Sa) + (3.6Ar) + (29.9MO) \\ W15000 = 26 + (5Ar) + (15.8MO) \end{cases} \quad (7)$$

Taking into account H_g = 0.4 m for the horizon thickness in Eq. 6, one considers a presumed UR_{base} ~ 50 mm. This ground *UR* value corresponds to the scale chosen by [35] to determine a rational management of irrigation water in Morocco. The value 50 mm corresponds to "stratified" floors, between fersiallitic (54 to 65 mm) and hydromorphic (≈ 0 mm), shallow to superficial and poor in organic matter [36]. For a given year, the monthly ET_i for each month *i* with i = 1, 2, …, 12 is computed by the following. Using the monthly rain $H_{r,i}$ yield (mm.month^{-1}), the water stock WST_i (mm.month^{-1}) for the month *i* is obtained by:

$$WST_i = UR_i + H_{r,i} \quad (8)$$

For $WST_i \geq PET_i$, the evapotranspiration (mm.month^{-1}) is:

$$ET_i = PET_i, \quad (9)$$

corresponding to $UR_i = UR_{base}$. This is the case when the soil (having a water reserve) can compensate for evapotranspiration. Consequently, the useful reserve of the previous month plus the rain of the studied month compensate the ETP and maintains the reserve to its base value calculated at the beginning of the evaluation. The volume of infiltrated water (mm.month^{-1}) is obtained by

$$WINF_i = WST_i - PET_i - UR_{base} \quad (10)$$

When $WST_i < PET_i$, the evapotranspiration is

$$ET_i = WST_i \quad (11)$$

With

$$UR_i = 0 \quad \text{and} \quad WINF_i = 0. \quad (12)$$

Preprints (www.preprints.org) | NOT PEER-REVIEWED | Posted: 24 October 2022 doi:10.20944/preprints202210.0357.v1

One notes from Eqs. 9-12 that $ET \leq PET$ because the soil reserve cannot provide the water needs for ETP.

3. Results and discussion

3.1. Past evolution (2005-2020)

Monthly dew or rain yields, noted $H_{d/r,i}$ (mean, min., max. values, in mm.mth^{-1}), are computed for each site by summing the daily data. Dew data are denoted with subscript *d* and rain data, with subscript *r*. Yearly dew or rain yields, noted $H_{d/r,y}$ (mm.yr^{-1}), are deduced by adding the monthly $H_{d/r,i}$:

$$H_{d/r,y} = \sum_{i=1}^{12} H_{d/r,i} \quad (13)$$

In order to estimate the dew or rain evolution, monthly and yearly yields are fitted to a linear regression on the measured period:

$$\begin{cases} H_{d/r,i}(t) = \alpha_{d/r,i} t + H^0_{d/r,i} \\ H_{d/r,y}(t) = \alpha_{d/r,y} t + H^0_{d/r,y} \end{cases} \quad (14)$$

When *t* is in month or year, the corresponding coefficients $\alpha_{d/r,i}$ or $\alpha_{d/r,y}$ represent the monthly or yearly evolution rate. The corresponding initial values are $H^0_{d/r,i}$ (monthly values) or $H^0_{d/r,y}$ (yearly values).

3.1.1. Dew yield

Mean, minimum and maximum dew yields are calculated on monthly and yearly time bases and reported in Table 3. The calculated yearly dew yields exhibit significant variations depending on the sites studied (Fig. 2 and Table 3), as discussed in the following.

Preprints (www.preprints.org) | NOT PEER-REVIEWED | Posted: 24 October 2022 doi:10.20944/preprints202210.0357.v1

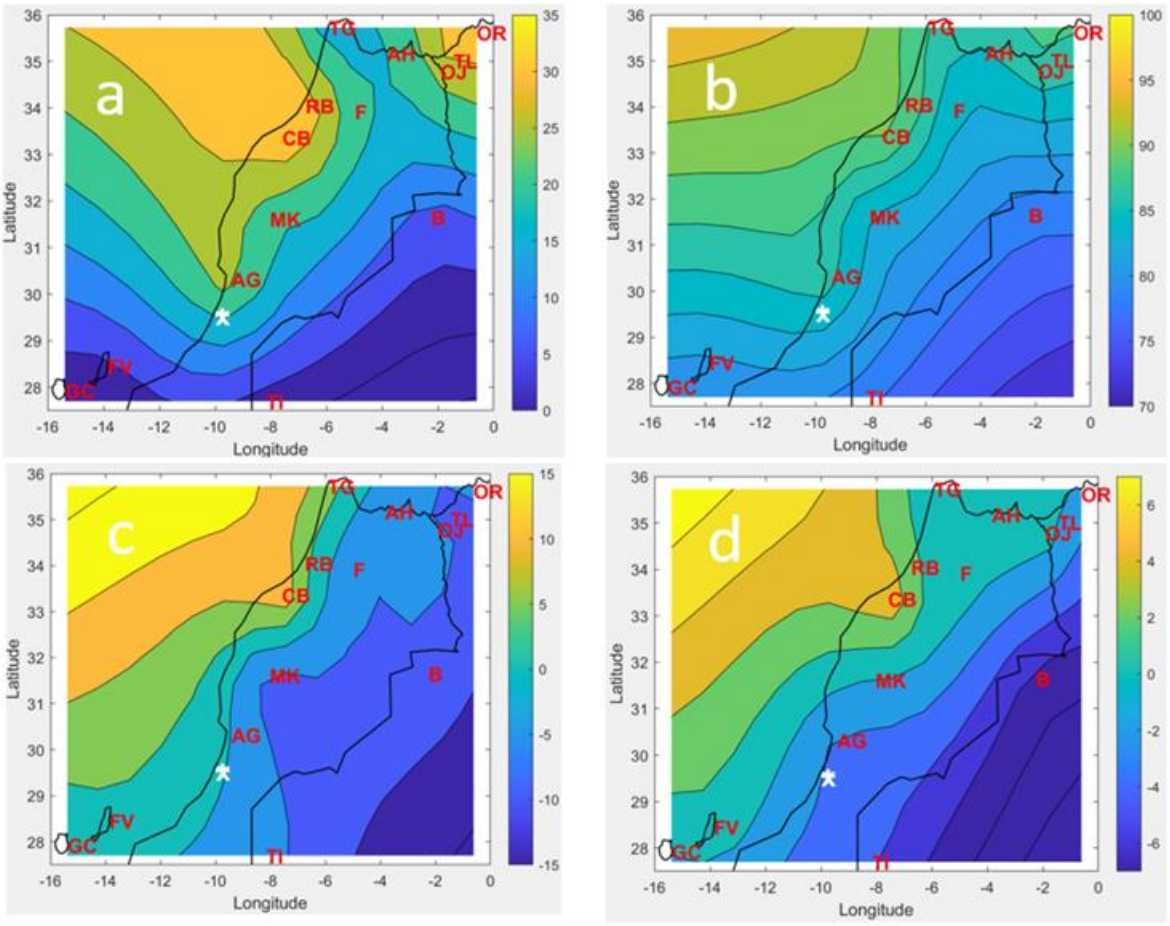

Figure 2. (a): Map of mean yearly dew yield $H_{d,y}$ (mm.yr^{-1}) for the period 2005 – 2020 (see text and Table 2). (b): Mean yearly nocturnal RH (%) during dew events during the same period. (c) Variations between years 2005 and 2020 of the yearly dew yield $H_{d,y}$ (mm.yr^{-1}). (d): Variations between years 2005 and 2020 of relative humidity RH (%). Red letters: Meteo sites (see Table 1). Right and inclined white crosses (very close) are, respectively, the sites of Mirleft (43 m asl, 200 m from the coast) and Id Ouasskssou (240 m asl, 8 km from the coast) as studied by [11].

Preprints (www.preprints.org) | NOT PEER-REVIEWED | Posted: 24 October 2022 doi:10.20944/preprints202210.0357.v1

Site	$H_{d,y}$ (mm.year^{-1})			$H_{d,i}$ (mm.mth^{-1})			$\alpha_{d,y}$ (mm.yr^{-1})	$H^0_{d,y}$ (mm.yr^{-1})	$\alpha_{d,i}$ (mm.mth^{-1})	$H^0_{d,i}$ (mm.mth^{-1})	Yearly frequency (%)
	Mean	Minimum	Maximum	Mean	Minimum	Maximum					
Gran Canaria	1.3	0.6	1.9	0.08	0.0	0.9	0.02	1.13	0.002	0.094	18.4
Fuerteventura	3.7	1.1	9.9	1.57	0.0	5.7	0.18	2.24	0.001	0.186	37.9
Agadir	28.0	20.8	35.9	2.67	0.5	5.6	-0.08	28.71	-0.001	2.398	80.7
Tindouf	1.0	0.1	2.7	0.09	0.0	1.4	-0.09	1.83	-0.001	0.147	8.3
Marrakech	18.8	4.7	32.8	1.24	0.0	11.1	-0.69	24.64	-0.005	2.028	60.4
Casablanca	32.1	18.9	54.3	1.82	0.4	8.9	2.05	14.69	0.014	1.314	78.3
Rabat	34.9	25.6	47.3	1.62	1.0	6.6	-0.22	36.82	-0.002	3.056	75.9
Tanger	14.9	10.3	24.8	0.53	0.2	4.2	-0.03	15.13	-0.003	1.281	55.8
Fès	21.9	14.2	36.5	2.13	0.0	9.0	-0.06	22.45	-0.001	1.898	58.7
Al-Hoceima	19.5	5.1	39.9	2.78	0.1	6.1	1.02	10.79	0.007	0.929	70.0
Béchar	6.4	0.8	11.6	2.64	0.0	6.5	-0.43	10.06	-0.003	0.801	22.1
Oujda	25.6	19.5	34.8	0.08	0.2	7.1	0.50	21.28	0.003	1.798	65.3
Tlemcen	33.4	23.6	43.8	1.57	0.4	6.9	-0.83	40.48	-0.006	3.345	71.7
Oran	31.7	23.6	40.9	2.67	0.4	7.5	0.15	30.49	0.001	2.542	74.2

Table 3. Monthly ($H_{d,i}$) and yearly ($H_{d,y}$) dew yields calculated from meteorological data. Mean (arithmetic, with $\overline{H}_{d,y} = 12\overline{H}_{d,i}$), minimum and maximum values are reported for the 16 years period (2005 – 2020). The evolution of the yearly and monthly mean values are fitted to Eq. 14 with $\alpha_{d,y}$ and $H^0_{d,y}$ (yearly means) and $\alpha_{d,i}$ and $H^0_{d,i}$ (monthly means) as free parameters. Red values correspond to a decrease, blue values to an increase.

Preprints (www.preprints.org) | NOT PEER-REVIEWED | Posted: 24 October 2022 doi:10.20944/preprints202210.0357.v1

The Atlantic Ocean coast of Morocco (Agadir, Casablanca, Rabat) exhibit high dew yields (> 28 mm.yr^{-1}), due to a high humidity related to the vicinity of the sea. The same behavior is observed for the coastal sites of the Mediterranean Sea in Algeria (Oran, Tlemcen) with large yearly dew yields (respectively 31.7 and 33.4 mm.yr^{-1}). For these sites, more than 70% of dewy days are observed on a year (min: 71.7% in Tlemcen; max: 80.7% in Agadir). The further from the sea, the less the dew yield, due the decrease of relative humidity. As a matter of fact, mean dew yields in the range 14.9 - 25.6 mm.yr^{-1} are obtained in Al-Hoceima, Fès, Marrakech, Oujda and Tanger. For two stations, dewy days are present between 55.8% (Tanger) and 70.0% (Al-Hoceima) of the year.

In contrast, the stations established in the interior of the country (Béchar, Tindouf) or located on Spanish islands (Fuerte Ventura, Gran Canaria) suffer from very low yearly dew yield (< 7 mm.yr^{-1}). For example, Tindouf and Béchar, respectively located at about 275 and 393 km from the sea, exhibit yearly dew yields of 1 mm and 6.4 mm. For Spanish islands, the yearly dew yields do not exceed 3.7 mm with a minimum of 1.3 mm at Gran Canaria. In these locations (the two islands, Béchar, Tindouf), daily dew yields are very weak with a mean of 0.1-0.5 mm and a monthly maximum of up to 6.5 mm. For these locations, only 8-38% of the days are dewy (min = 8.3% at Tindouf and max = 37.9% at Fuerte Ventura). Concerning the Canaria islands, the predominant winds are trade winds, which blow from the continent with low RH. The dew events correspond to other (west) wind directions with larger RH.

Table 3 shows that the yearly (and monthly) trend on the period 2005-2020 is positive for 50 % of the sites, with mean arithmetic value $\bar{\alpha}_{d,y} = 0.65 \pm 0.32\ \mathrm{mm.\,yr^{-1}}$. The increase in dew yield is mainly concerned with the sites located in the north of the country (Al-Hoceima, Casablanca, Oran, Oujda) and to a lesser extent the Canaria islands (Gran Canaria and Fuerte Ventura). In contrast, the inland sites show a weak decrease ($\bar{\alpha}_{d,y} = -0.30 \pm 0.11\ \mathrm{mm.\,yr^{-1}}$), strongly correlated with a decrease in RH as can be seen in Fig.2d.

The spatial distribution of dew yields was determined by Kriging (Fig. 2). Map of mean yearly dew yields are presented in (Fig. 2a). As expected and described in the literature [27], dew exhibits the highest yields along the coasts of Atlantic Ocean and Mediterranean Sea. Due to the spatial repartition of RH (Fig. 2b), the Atlas Mountains delineate a meteorological limit with the higher yields in the North-West and the lower yields in the South-East of Morocco. The maps of Fig.2 are in close agreement with the trends determined above with the mean evolution factor $\bar{\alpha}_y$. As a consequence, and in agreement with the values of the evolution factor $\bar{\alpha}_y$, one observes between 2005 and 2020 a clear decrease in dew yields along a northwest/southeast axis, exceeding 10 mm.year^{-1} in some places, see Fig.2c. This decrease is strongly correlated with the corresponding decrease in RH (up to 7%, see Fig.2d). The areas from the Atlantic coast to the Saharan desert are gradually impacted by this decrease.

Let us consider more specifically the Sahara Desert, which represents about 8.6 million of km² and extends over ten countries (Morocco, Algeria, Tunisia, Libya, Egypt, Sudan, Chad, Niger, Mali, Mauritania). In the spatial area considered in this study, the fraction of Sahara

Preprints (www.preprints.org) | NOT PEER-REVIEWED | Posted: 24 October 2022 doi:10.20944/preprints202210.0357.v1

Desert stretches over about 386 000 km² (2/5 in Morocco and 3/5 in Algeria). One also clearly observes a decrease in dew yields, especially from the highlands (Atlas Mountains) towards south-west. However, one notes that in these areas, the monthly dew yields can reach mean and maximal values up to 2.4 – 6.5 mm and 0.09 – 1.4 mm, respectively (Béchar and Tindouf, see Table 3). More generally, there is a tendency to see a decrease in dew yield with increasing distance from the sea, located W and N. A clear decrease in nocturnal RH from north-west to south-east is obvious (Fig. 2b), with the largest dew yields (Fig. 2a) corresponding to the regions of highest RH (80% to 90% on Atlantic and Mediterranean coasts but only 70% in the Sahara Desert). The tendency over the years 2005 – 2020 is a weak decrease, with (Béchar) a decrease of 0.43 $mm.yr^{-1}$ and (Tindouf), 0.09 $mm.yr^{-1}$.

3.1.2. Comparison with direct dew yield measurements

The calculated dew yields can be compared with previous measurements carried out by [11] in two neighboring sites of S-Morocco, Mirleft (right cross in maps) and Id-Ouakssou (inclined cross in maps). These authors reported dew and rainfall measurements from weather stations, located on the Atlantic Ocean coast of southwestern Morocco (Mirleft: 29°35'17 N, 10°02'20 W, 43 m asl, 200 m from the coast; Id-Ouakssou: (29°34'03 N, 9°59'51 W, 240 m asl, 8 km from Mirleft in the E direction)). Mirleft and Id-Ouakssou are about 100 km SSW from Agadir.

During the studied period (May 2007-April 2008) the yearly percentage of dew days in Mirleft was 48.6%, with a mean dew amount of 18.9 mm (data from the N-oriented condenser in [11]). The estimation from Eq. 3 for the same period is 31.9 mm in Agadir. When comparing in the same time period (May 2007-April 2008) the Mirleft data with the closest kriging grid point (29°33'00" N, 9°42'14" W, 27 km apart), the calculated mean dew yield is 23.9 mm, about 25% more than the measurements. Between 2005 and 2020, the mean is 20.8 mm.

According to [25], rainfall was 119.8 mm at Agadir during the period May 2007-April 2008, to be compared with a cumulative rainfall of 48.7 mm measured at Mirleft during the same period ([11]). At the nearest kriging grid point, the value is 86.0 mm between May 2007 and April 2008, considerably larger than measured in Mirleft. The fact that rain volume was measured on the dew collector instead of using a standard rain gauge might explain the discrepancy.

In Mirleft, the cumulated amount of the ratio dew/rain, calculated from the data in [11], is $\left(\overline{H}_{d,y}/\overline{H}_{r,y}\right)_{meas.} = 38.8\%$. The present kriging study gives a value $\left(\overline{H}_{d,y}/\overline{H}_{r,y}\right)_{calc.} = 28\%$, in reasonable agreement with the measurements.

The second site, Id Ouasskssou, was studied between July 1 and September 30, 2007. 50 dew events (54.3% of the period) are observed for a dew yield of 7.1 ± 0.3 mm. There was no rain collection at Id Ouasskssou and the data were taken from the Mirleft site. Six rainy events were reported (15.6 ± 2 mm, 6.5% frequency for the period). Located between two grid points, the results for Id Ouasskssou is interpolated. On the period July-Sept 2007, the kriging

Preprints (www.preprints.org) | NOT PEER-REVIEWED | Posted: 24 October 2022 doi:10.20944/preprints202210.0357.v1

methodology allows 5.5 mm to be obtained for dew and 14.4 mm for rain. The agreement with the measured rainfall is good (measured: 15.6 mm); the dew yield obtained by kriging presents an acceptable error of 23%, compatible with the uncertainty of the model ([12]).
Figure 3 compares for the period May – October 2007 the dew yields obtained by the physical model (this study) with the yields calculated in Mirleft by a neural networks approach (ANN) via a learning method ([11]). The ANN result for Mirleft was assumed to be also valid for the other Morocco cities. On 8 sites, it shows that the calculated $H_{d,y}$ values computed from ANN somewhat underestimate the values estimated from the physical model (Eq. 3), presumably because the ANN extrapolation from Mirleft to other cities is not fully justified. The correlation shows a proportionality factor of 0.75 (± 0.06) and $R^2 = 0.753$ (uncertainty: One standard deviation).

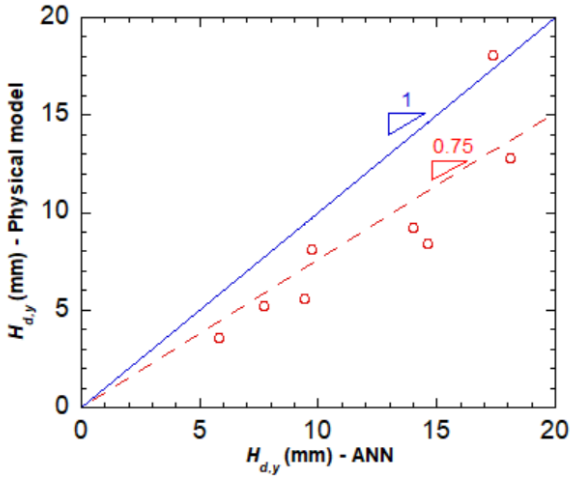

Figure 3. Yearly dew yields ($mm.yr^{-1}$) for 8 cities of Morocco as obtained from the physical model estimation (ordinate, Eq. 3) compared with the data obtained from an artificial neural network approach using the Mirleft data (abscissa, [11]). The full line corresponds to the equality of both calculations.

3.1.3. Rain

Table 4 and Fig. 4 present the yearly and monthly mean (yearly mean = monthly mean ×12), min and max rainfall data extracted from [25]. From a general point of view, rain decreases towards SE (except the Spanish islands, Fuerte Ventura and Gran Canaria, located SW). As described below, the cities located in the Sahara Desert exhibit the lowest yearly rain precipitations: 58 mm in Tindouf and 116 mm in Béchar (i.e. respectively 3.2 % and 7.6 % of rainfall events by year). In these areas (Fig. 4a), precipitations are very erratic, with no rain for several months and only a few intense precipitations events (see also section 3.3.2).

Inland rainfalls, although remaining relatively weak, are more abundant than above, with yearly averages of 184 and 255 $mm.year^{-1}$ for Marrakech and Oujda, respectively, although these areas can exhibit months without any rain (Table 4). However, one notes that less than

Preprints (www.preprints.org) | NOT PEER-REVIEWED | Posted: 24 October 2022 doi:10.20944/preprints202210.0357.v1

16% of the days of the year are rainy days (11.9% and 15.6% in Marrakech and Oujda, respectively). The closer to the coast, the heavier the rainfall precipitations (Fig. 4a).

Figure 4b exhibits the yearly difference in rainfall (mm) between years 2020 and 2005. The whole area suffers from a drop in precipitation with the exception of the region of Al-Hoceima near the Mediterranean Sea. This is due to an exceptional year of rain (457 mm in 2020 against an average of 302 mm over 16 years). As observed in Table 4, Agadir, Casablanca, Rabat, Tanger, Al-Hoceima and Oran exhibit mean yearly rainfall between 294 $mm.yr^{-1}$ (Agadir) and 549 $mm.yr^{-1}$ (Tanger), with mean monthly rainfall ranging from 24.5 $mm.mth^{-1}$ (Al-Hoceima) to 45.8 $mm.mth^{-1}$ (Tanger). In these locations, less than 21.5% of days of the year are rainy days with a minimum of 8.2% for Agadir, corresponding to intense rainfalls.

One notes than the ratio between the yearly cumulative dew and rainfall volumes, averaged over 16 years (2005-2020),

$$r = \left(\frac{1}{16}\right)\sum_{2005}^{2020}\left(H_{d,y}/H_{r,y}\right) \quad (15)$$

can reach 12% (Fig. 4c). Two areas are concerned by these high ratios: Agadir/Casablanca/Marrakech/Oujda in Morocco and Oran/Tlemcen in Algeria. For desert sites such as Béchar and Tindouf, the cumulative dew/rain ratio presents values in the range 4 to 8%.

Yearly rainfall data (Table 4) are fitted to Eq. 14 to evidence a long term tendency. The yearly tendencies over the 16 years period undoubtedly show a decrease of yearly rainfall, with an (arithmetic) mean evolution factor $\bar{\alpha}_{r,y}$ = – 4.4 ± 0.75 $mm.yr^{-1}$. Only two inland sites (Fès, Tindouf) and one coastal site (Rabat) present a weak increase tendency on the studied period, with $\bar{\alpha}_{r,y}$ = 1.3 ± 1 $mm.yr^{-1}$.

	$H_{r,y}$ (mm)			$H_{r,i}$ (mm)			$\alpha_{r,y}$ ($mm.yr^{-1}$)	$H^0_{r,y}$ ($mm.yr^{-1}$)	$\alpha_{r,i}$ ($mm.mth^{-1}$)	$h^0_{r,i}$ ($mm.mth^{-1}$)	Yearly frequency (%)	r (%) RCP2.6 RCP8.5
Site	Mean	Minimum	Maximum	Mean	Minimum	Maximum						
Gran Canaria	112	38	281	9.3	0	113	-6.907	170.76	-0.0488	14.042	11.2	0.7 ± 0.1 0.9 ± 0.2
Fuerteventura	61	10	131	5.1	0	69	-3.059	87.33	-0.0208	7.1134	7.4	7.7 ± 0.9 9.9 ± 1.6
Agadir	294	10	1114	24.5	0	662	-8.209	364.13	-0.0534	29.678	8.2	8.2 ± 0.8 8.0 ± 0.7
Tindouf	58	4	144	4.8	0	120	0.048	57.68	0.0021	4.6384	3.2	1.2 ± 0.2 1.1 ± 0.1
Marrakech	184	68	324	15.3	0	139	-1.514	197.47	-0.0113	16.472	11.9	2.8 ± 0.2 3.3 ± 0.2
Casablanca	346	82	624	28.8	0	213	-3.743	387.17	-0.0268	31.447	16.8	6.1 ± 0.6

Preprints (www.preprints.org) | NOT PEER-REVIEWED | Posted: 24 October 2022 doi:10.20944/preprints202210.0357.v1

												6.5 ± 0.3
Rabat	488	117	1236	40.7	0	326	0.645	482.88	0.003	40.413	19.9	4.4 ± 0.4 5.1 ± 0.4
Tanger	549	99	920	45.8	0	355	-2.8744	573.48	-0.0136	47.071	21.5	2.1 ± 0.2 2.0 ± 0.2
Fès	472	130	844	39.3	0	216	3.371	443.88	0.0204	37.414	19.1	2.4 ± 0.2 2.5 ± 0.1
Al-Hoceima	302	78	562	25.2	0	255	-0.734	309.06	-0.0088	26.081	15.8	3.0 ± 0.2 3.3 ± 0.1
Béchar	116	8	276	9.67	0	236	-6.5135	171.22	-0.043	13.802	7.6	2.9 ± 0.3 3.1 ± 0.6
Oujda	255	61	760	21.2	0	466	-7.474	318.78	-0.0596	27.025	15.6	3.6 ± 0.2 4.0 ± 0.2
Tlemcen	282	153	427	23.5	0	111	-3.551	311.72	-0.027	26.068	17.8	4.0 ± 0.2 4.3 ± 0.1
Oran	331	206	534	27.6	0	144	-3.955	364.56	-0.025	30.006	18.6	2.9 ± 0.2 3.5 ± 0.2

Table 4. Yearly ($H_{r,y}$) and monthly ($H_{r,i} = H_{r,y}/12$) rainfall values from meteorological data. Mean (arithmetic), minimum and maximum values are reported for the 16 years period (2005 – 2020). The evolution of the yearly and monthly mean values are fitted to Eq. 14 with $\alpha_{r,y}$ and $H^0_{r,y}$ (yearly means), and $\alpha_{r,i}$ and $H^0_{r,i}$ (monthly means) as free parameters. Red values correspond to a decrease, blue values to an increase. r is the ratio between the yearly cumulative dew and rainfall volumes averaged over the period 2005-2100 (Eq. 15).

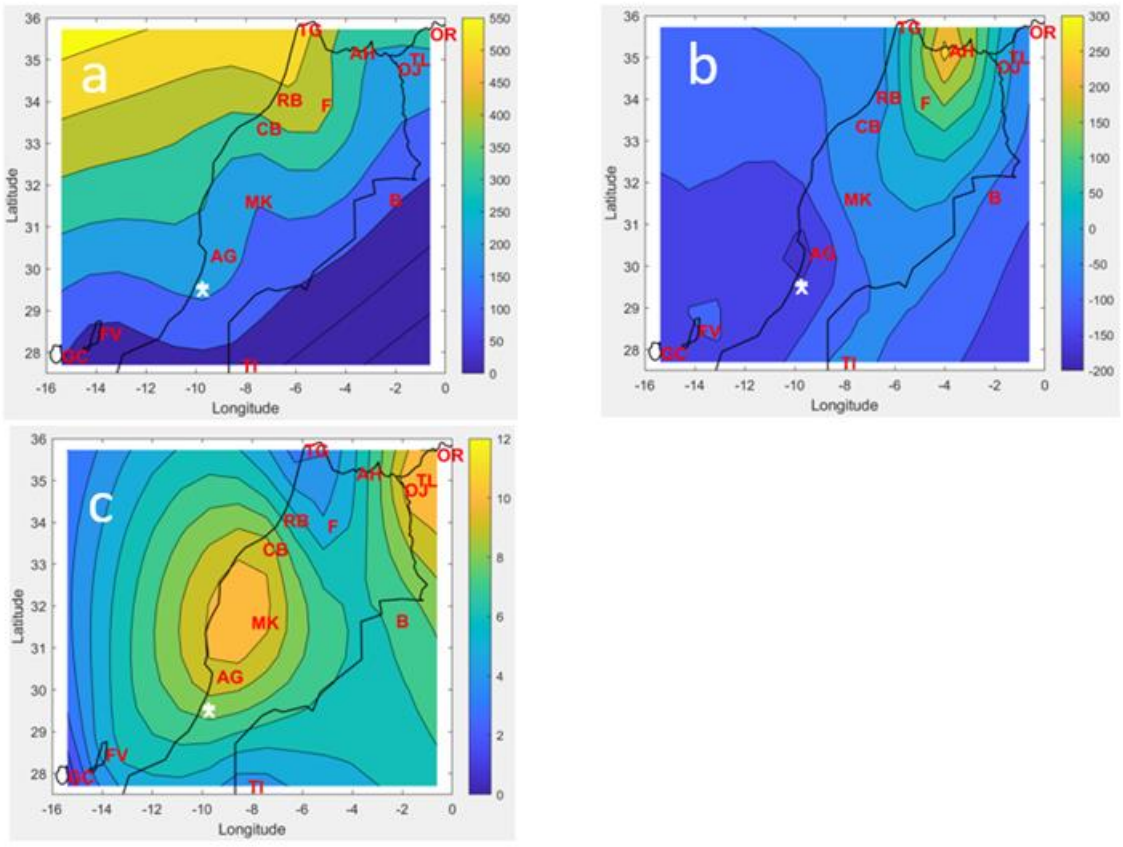

Preprints (www.preprints.org) | NOT PEER-REVIEWED | Posted: 24 October 2022 doi:10.20944/preprints202210.0357.v1

Figure 4. (a) Mean yearly rainfall (mm.yr^{-1}) during the period 2005 - 2020. (b) Yearly rainfall difference (mm.yr^{-1}) between both years 2020 and 2005. (c) Ratio *r* (%) between the means of the yearly cumulative dew and rainfall volumes over the period 2005 – 2020 (Eq. 15). Red letters: Measurement sites (see Table 1). Right and inclined crosses (very close) represent, respectively, Mirleft (43 m asl, 200 m from the coast) and Id Ouasskssou (240 m asl, 8 km from the coast), both sites studied by [11].

3.2. Projected climate evolution 2020-2100

The 5th report of the Intergovernmental Panel on Climate Change has defined future scenarios of greenhouse gas emissions, denominated the Representative Concentration Trajectories (RCP): A scenario with a minimum of greenhouse gas emissions (RCP 2.6), two scenarios of stabilization (RCP 4.5 and RCP 6.0), and one scenario with a very high level of greenhouse gas emissions (RCP 8.5). In order to estimate from 2020 to 2100 the variation of meteorological and physical variables, we have chosen to work with only the two extreme scenarios, RCP 2.6 and RCP 8.5.

The tendencies of the predicted variables are computed from the time derivative each 5 years (with one exception, see below). For dew and rain, with *dt* = 5 years, one thus considers, with $Y_y = H_{d/r,y}$ the yearly dew or rain yield or $Y_y = T_{a,y}$, the yearly averaged air temperature:

$$\dot{Y}_{dt} = \frac{dY_y}{dt} \tag{16}$$

The cumulative function of $\dot{H}_{d/r,l}$ starting in 2006 (first year available for climatic prospective data on the Copernicus-Cordex database) and ending in 2100 gives the global variation of H_i:

$$\Delta Y_y = \sum_{2006}^{2100} \dot{Y}_{dt} = Y_y(2100) - Y_y(2006) \tag{17}$$

The time step is *dt* = 5 years except between 2006 and 2009 where it is 4 years. The starting time is 2006 because it is the first available year in the Copernicus database.

3.2.1. Typical tendencies

Air temperature ($T_{a,y}$) and dew and rain yields ($H_{d,y}$, $H_{r,y}$) are computed for the past period (2005-2020) and the future (2020-2100). According to Eqs 16-17, the evolutions are compared with the measured means obtained for T_a between 1990 and 2020 [37], between

Preprints (www.preprints.org) | NOT PEER-REVIEWED | Posted: 24 October 2022 doi:10.20944/preprints202210.0357.v1

2005 and 2020 for dew yield H_d (calculation from Eq. 3) and between 1990 and 2020 for rain yield H_r [22]. One uses the following notations:

$$\begin{cases} \Delta T_a = T_a(t) - \bar{T}_a|_{1980-1990} \\ \Delta H_d = H_d(t) - \bar{H}_d|_{2005-2020} \\ \Delta H_r = H_r(t) - \bar{H}_r|_{1990-2020} \end{cases} \quad (18)$$

As an example, Figure 5 reports the evolutions for the site of Tanger. The most important influence of the RCP scenario is visible on the air temperature T_a (Fig. 5a) with increases of 0.5 to 1°C (RCP 2.6) and 3.5 to 4°C (RCP 8.5) at the end of the century. These values are in agreement with those obtained by [3]. The scenario 2.6 shows a stabilization of the temperature evolution, while the unfavorable scenario (RCP 8.5) shows, from year 2020 with acceleration after 2040, an almost linear increase over several decades (see Fig. 5a). According to previous works [38], this tendency was already observed on different area in Morocco. Temperature anomalies are indeed observed most frequently since 2010 leading in 2020 to an increase of +1.3°C in relation to the normal climatic temperature measured on the period 1981-2010. Years 2010, 2017 and 2020 are clearly the hottest years recorded since 1980.

Regarding the dew amounts, the trend is mainly decreasing (Fig. 5b and Fig. 6cd). One observes for RCP 2.6 a decrease of -0.296 mm.decade^{-1}; for RCP 8.5 the evolution becomes and -0.259 mm.decade^{-1}. Compared with 2006, dew yields should have decreased (-9.5%, RCP 2.6 and -13.6%, RCP 8.5) by the end of this century. However, for rain, one notes for RCP 2.6 an increase of rainfall between 2030 and 2090 and later a decrease to zero. Concerning RCP 8.5, one observes a weak decrease on order of -11 mm.decade^{-1} (-12%, RCP 8.5). The last scenario seems to be more credible because the decrease is already present in the measured data since the beginning of years 2000.

Sebbar et al. [39] and Driouech [40] have already highlighted a climate change identified around the end of the 1970's. As a matter of fact, a majority of meteorological stations in the mountainous region of the Middle Atlas in Morocco observed a reduction in rainfall of around 18%. Khomsi et al. [41] confirmed this evolution by the decennial study of rainfall in Morocco since the middle of the 20th century. Stations such as Rabat (-3.31 mm.decade^{-1}), Marrakech (-2.79 mm.decade^{-1}), Fez (-12.7 mm.decade^{-1}) or Tanger (-23.7 mm.decade^{-1}) are experiencing significant rainfall decreases in winter season. The situation in 2022 is particularly alarming, with very weak precipitations during the winter season.

Preprints (www.preprints.org) | NOT PEER-REVIEWED | Posted: 24 October 2022 doi:10.20944/preprints202210.0357.v1

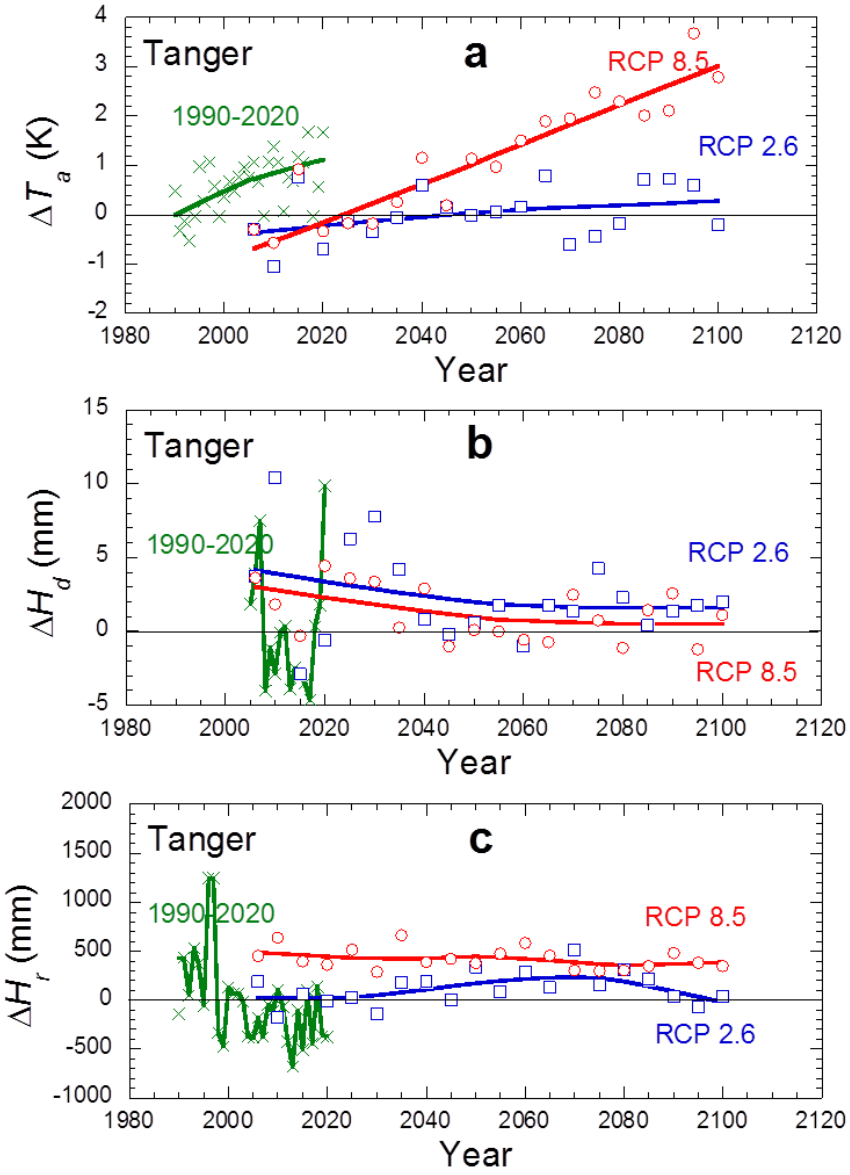

Figure 5. Predicted evolutions for Tanger (Morocco). Green crosses: Actual data of the difference with respect to the yearly mean value; blue squares: RCP 2.6 scenario; red circles: RCP 8.5 scenario. Curves are smoothened data. (a) Air temperature with respect to the 1980-1990 mean, $\Delta T_a = T_a(t) - \bar{T}_a|_{1980-1990}$ (K). (b) Dew yield $\Delta H_d = H_d(t) - \bar{H}_d|_{2005-2020}$ (mm) with respect to the 2005-2020 mean. (c) Rain precipitation $\Delta H_r = H_r(t) - \bar{H}_r|_{1990-2020}$ with respect to the 1990-2020 mean.

Figure 6 presents for years 2006 and 2100 and for both extreme RCP scenarios the monthly potential evapotranspiration PET and actual evapotranspiration ET values. Monthly $H_{d,i}$ and $H_{r,i}$ yields are also shown for comparison. One can draw the following conclusions for the evolution between 2006 and 2100.

Firstly, the yearly PET (addition of the monthly PET over the year) displays an increase over the century (Figs 6ac): Weak for the scenario RCP 2.6 (one calculates +4.0 mm.decade^{-1}),

Preprints (www.preprints.org) | NOT PEER-REVIEWED | Posted: 24 October 2022 doi:10.20944/preprints202210.0357.v1

larger for the scenario RCP 8.5 (+7.4 mm.decade^{-1}). This increase is related to the expected increase in ambient temperature (Fig. 5a). Agoumi et Debbarh [42] have already reported a PET increase between 1961 and 2004 in relation to air temperature increase, causing adverse effects on the water potential of Morocco.

Secondly, the increase in PET is distributed almost evenly over all months of the year (Figs 6ac). For RCPs 2.6/8.5, it corresponds to a monthly mean of +0.035 mm.month^{-1} and +0.065 mm.month^{-1}, respectively.

Thirdly, on observes in (Figs 6ac) that *ET*(2100) < *ET*(2006) with -15.8 mm.decade^{-1} for RCP 2.6, meaning that evaporation of water contained in the soil decreases, which looks coherent with the scenario RCP2.6 where an inversion of the climatic warming process is observed. For RCP 8.5, an exceptional rainy month of May 2100 (132 mm) leads to *ET*(2100) > *ET*(2006) but during the century, the *ET* tendency is a decrease with ET(2100) < ET(2006). Note that a source of uncertainty is the impact of the large scale climatic phenomena on *ETR* [43]. When determining *ETR* starting from ET_0 (projected reference evapotranspiration from the climatic variables), the increase of temperatures and the change of the mode of precipitations is a source of uncertainty of the hydrological models. The choice of the method can involve biases of several tens of millimetres per year [44].

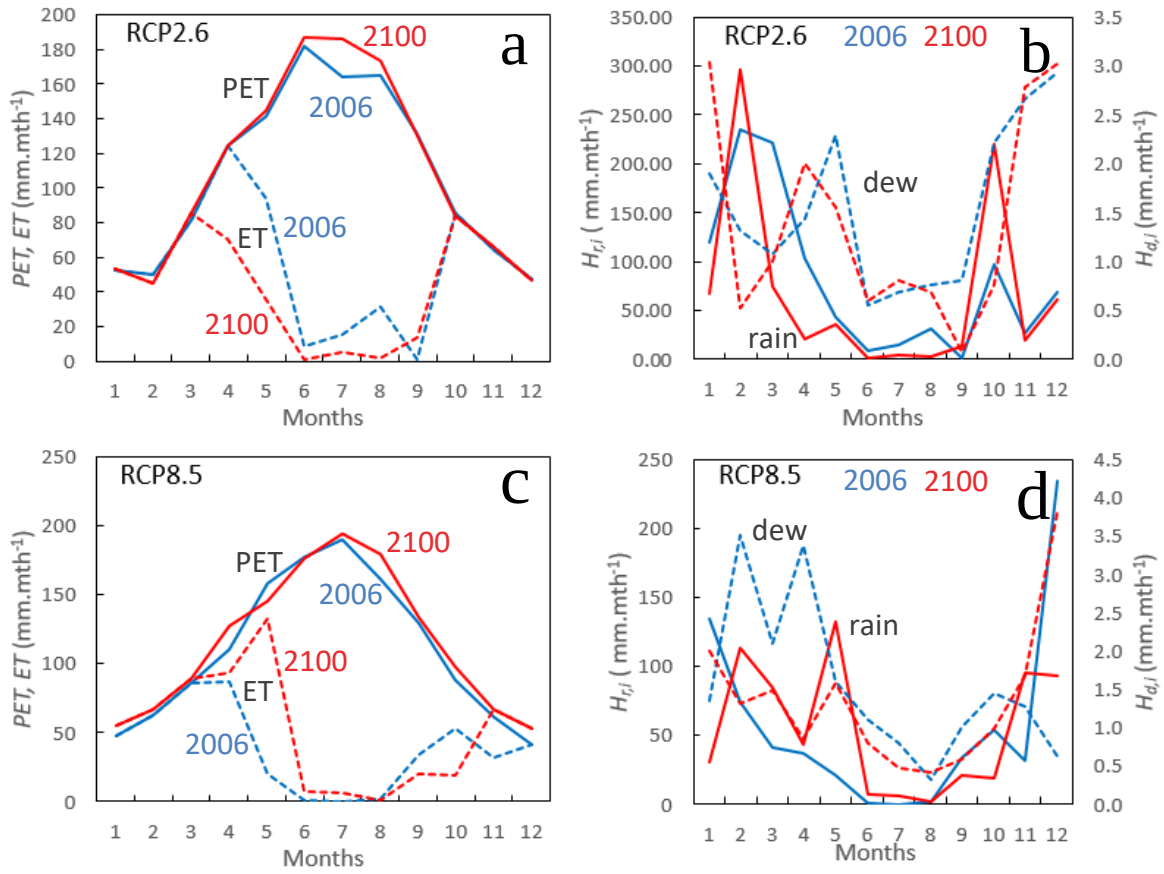

Figure 6. Variation between 2006 (blue curves) and 2100 (red curves) of the monthly mean of potential evapotranspiration PET (a, c, full lines), actual evapotranspiration ET (a, c,

Preprints (www.preprints.org) | NOT PEER-REVIEWED | Posted: 24 October 2022 doi:10.20944/preprints202210.0357.v1

interrupted lines), rain monthly means $H_{r,i}$ (b, d, full lines), and dew monthly means $H_{d,i}$ (interrupted lines). The scenario RCP 2.6 is in (a, b) and RCP 8.5 in (c, d).

3.2.2. Dew and rain maps evolution

Dew and rain maps have been computed for each RCP scenario. Figure 7 shows yearly dew and rain yields ($mm.yr^{-1}$) calculated on 4 specific years (2020, 2050, 2075 and 2100). The evolution of the dew resources during the 21^{th} century are computed from Eq. 3.

As expected, the Atlantic and Mediterranean coasts are the regions with the largest dew yields (dew > 20 $mm.yr^{-1}$). For 2020, both scenarios present the same situation. For the future, whatever is the climatic scenario, one notes a weak decrease in dew and a significant reduction in rain precipitation over the century. This decrease appears more noticeably after 2050 as if the current climate system had an inertia that any current action could not modify. As expected, the decrease in precipitation is less marked in scenario RCP 2.6. The unfavorable RCP 8.5 scenario leads to a noteworthy diminution in precipitation along the coasts but also on the foothills of the Atlas Mountains.

Preprints (www.preprints.org) | NOT PEER-REVIEWED | Posted: 24 October 2022 doi:10.20944/preprints202210.0357.v1

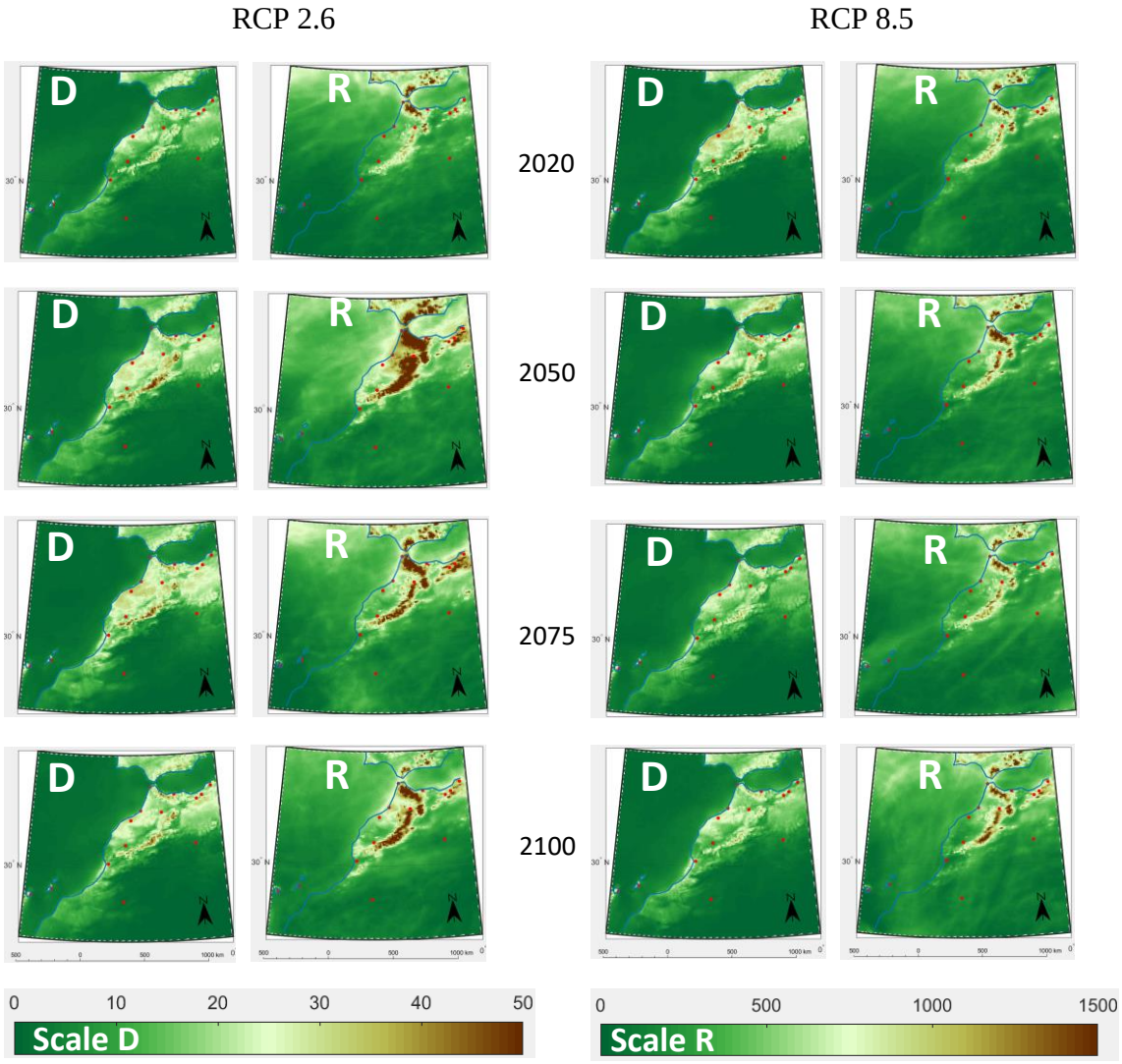

Figure 7. Projected yearly dew yields (D, mm.yr^{-1}) and rain yields (R, mm.yr^{-1}) in North-West Africa according to the RCP scenarios 2.6 (left) and 8.5 (right) for years 2020, 2050, 2075 and 2100 (from top to bottom). Red points are the airport stations described in Table 1 and Fig.1.

According to Eq. 17, Figure 8 shows the variations in yields, $\Delta H_{d/r,y}$, between 2100 and 2006 with a 5-years time step. Regarding dew, the scenario 2.6 leads to a slight increase (0 – +5 mm.yr^{-1}) for coastal areas and slight decrease elsewhere (0 – -5 mm.yr^{-1}). The mountainous area of the Atlas and the Algerian and Moroccan Sahara will clearly suffer from a marked yearly dew deficit, which can reach -10 mm. Algerian sites close to the Tunisian border will benefit from an increase in dew yields under the influence of humidity from the Mediterranean Sea (+6 to +8 mm.yr^{-1}). Unfavorable scenario RCP 8.5 exhibits a greater decrease: The whole country is hit by a decrease in dew yields, including coasts. Coastal

Preprints (www.preprints.org) | NOT PEER-REVIEWED | Posted: 24 October 2022 doi:10.20944/preprints202210.0357.v1

towns in Algeria will experience dew yield reductions of around -5 to -10 mm.yr^{-1}. Paradoxically, the desert areas of the Sahara may benefit from an increase in dew yield of a few mm (< 5 mm.yr^{-1}).

Regarding rain, most of the country will be affected by a notable drop in precipitation. The amplitude of this decrease can reach on the coast 200 mm.yr^{-1} and 400 to 500 mm.yr^{-1} on the foothills of Atlas. Only the extreme south of the country on the Mauritanian border could experience, with the RCP 8.5 scenario, a significant increase in rainfall.

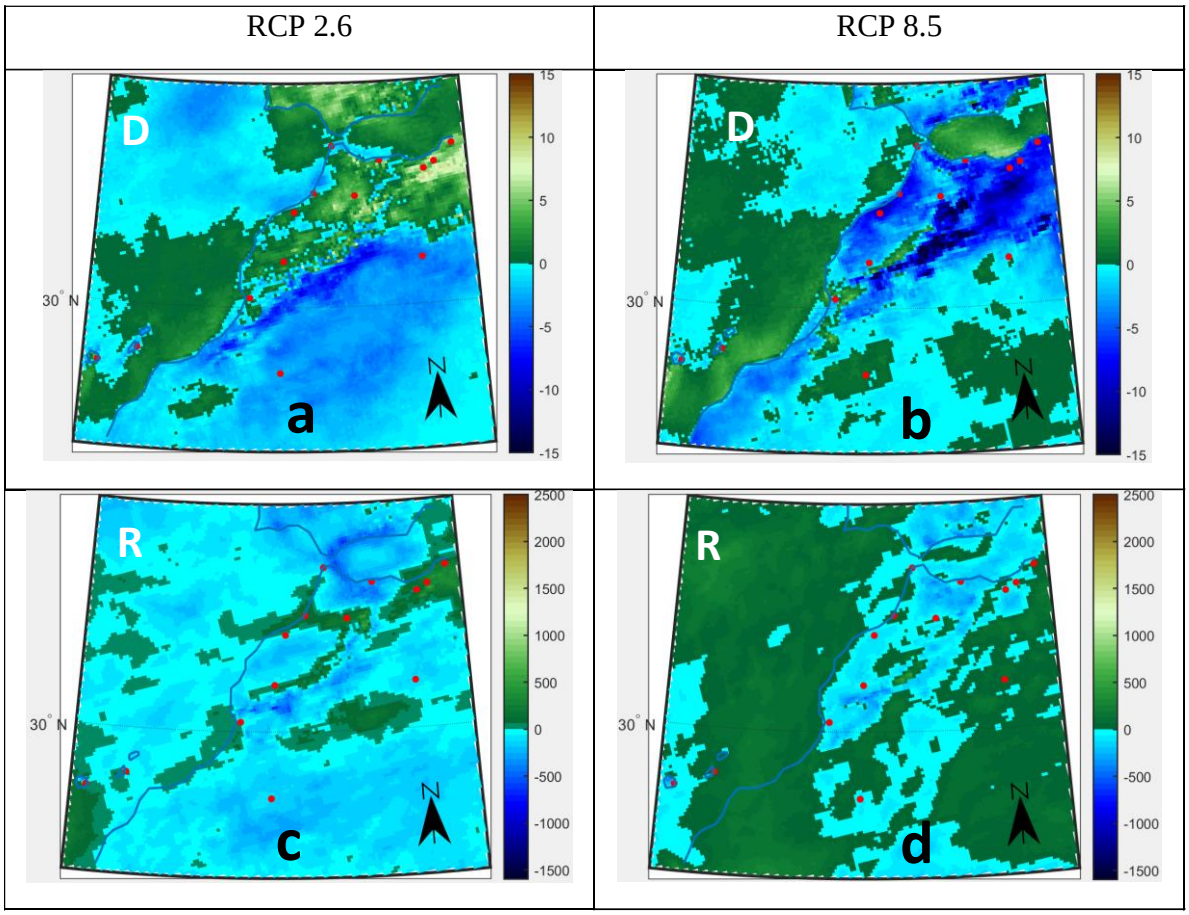

Figure 8. Spatial variation of the difference in yearly dew and rain yields $\Delta H_{d/r,y}$ between 2100 and 2006 according to (a, c) scenario RCP 2.6 and(b, d) scenario RCP 8.5. Dew: (a, b); Rain: (c, d). Red points: airport stations described in Table 1 and Fig.1.

3.3. Correlation between dew and rain amounts

3.3.1 Cumulated dew and rain yields

Analyzing the evolution of the summed values of the yearly dew ($H_{d,y}$) and rain ($H_{r,y}$) yields enables to smoothen the scattering of data and makes more apparent the comparisons. In Fig. 9 are reported the summed values within a 5 years' time step. The dew/rain ratio

Preprints (www.preprints.org) | NOT PEER-REVIEWED | Posted: 24 October 2022 doi:10.20944/preprints202210.0357.v1

$$\tau\ (\%) = \frac{\mathrm{sum}H_{d,y}}{\mathrm{sum}H_{r,y}} \tag{19}$$

is also presented.

For each studied site, both past and future periods are considered. Past period 2005-2020 (4 values, full lines), where $H_{d,y}$, $H_{r,y}$ and τ are computed from the measured data (Eq. 3), and future period 2006-2100 (20 values, interrupted lines), with parameters calculated from the predicted meteorological data according to scenarios RCP 2.6 and RCP 8.5. As examples, Fig. 9 presents the evolutions at Gran Canaria island, Casablanca and Al-Hoceima. All others results are presented in Supplementary Materials (Fig. SM1). As already noted in Section 3.2.1, one sees in Fig. 9 a general tendency to a decrease in the slopes of the evolution curves, corresponding to a decrease in dew and rain yields.

The period 2005-2020 using actual data can be compared with the RCP models. The agreement is generally good (within the exceptions of Agadir and Marrakech for dew). One notes a better agreement with the projection of the scenario RCP 8.5 in this period.

The relative contribution dew/rain as measured by r (Fig. 9), which interestingly exhibits nearly constant values during the whole period. The values, reported in Table 4, are dependent on the sites and are found in the range 1 - 10%. Small values (τ < 2%) are obtained for Gran Canaria, Tindouf, Béchar and Tanger. For Tindouf and Béchar, the low relative humidity strongly impacts dew formation (Table 3). In contrast, the small value of τ can be attributed in Tanger to the high amount of rain (the most rainy site, see Table 4). At Agadir, Casablanca and Fuerte Ventura, τ is about 8 to 10%. For Fuerte Ventura, the dew yield is almost 3 times greater (Table 3) than in Gran Canaria with rainfall which is two times less than in the other nearby island (Table 4). Agadir and Casablanca, both coastal oceanic cities, present the largest dew/rain ratios due to high dew yields and moderate rainfalls (Tables 3 and 4).

Preprints (www.preprints.org) | NOT PEER-REVIEWED | Posted: 24 October 2022 doi:10.20944/preprints202210.0357.v1

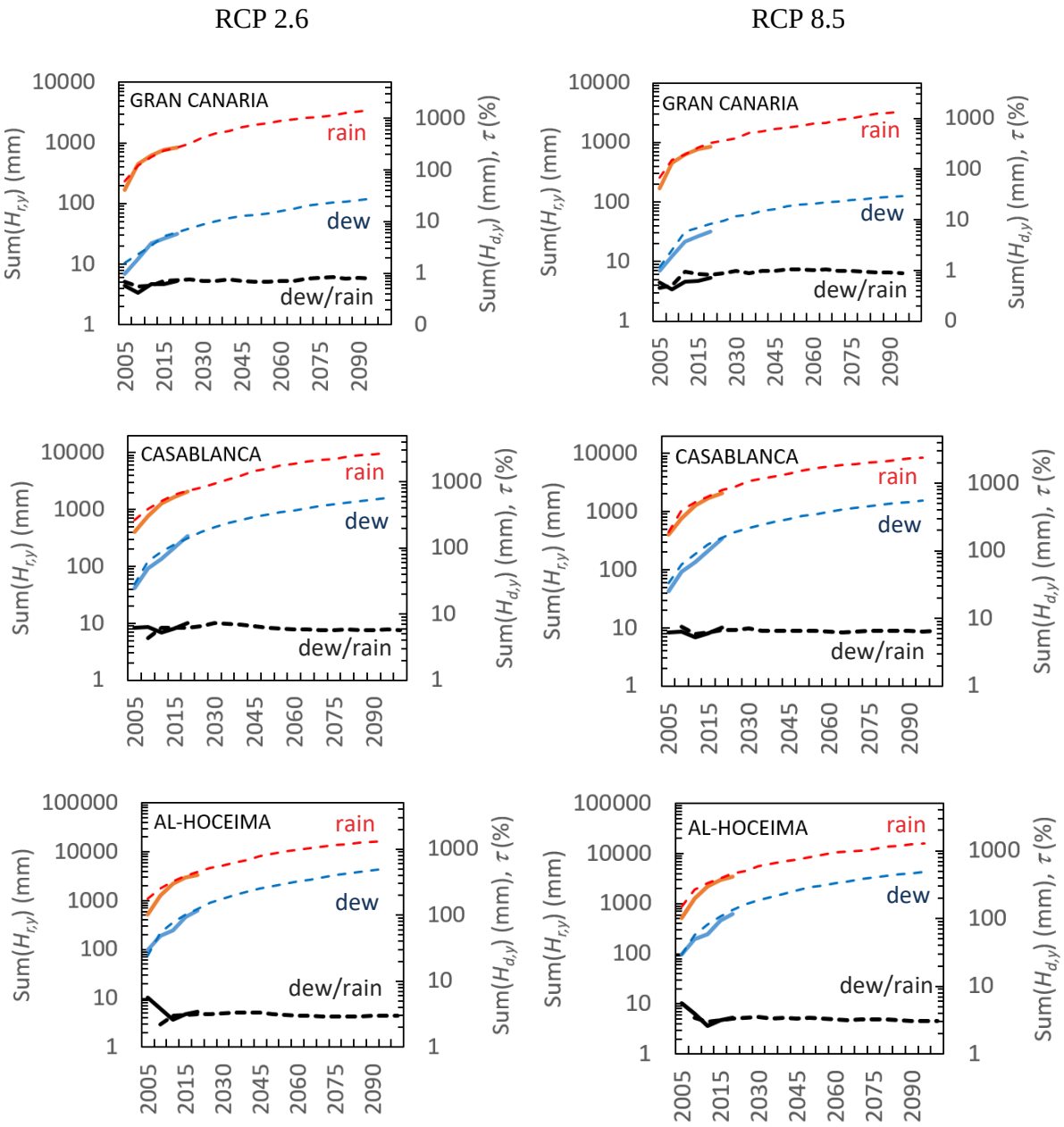

Figure 9. Semi-log plot for three studied sites (Gran Canaria, Casablanca and Al-Hoceima) of the yearly summed values for dew ($H_{d,y}$, blue, mm.yr^{-1}, right axis), rain ($H_{r,y}$, red, mm.yr^{-1}, left axis), and their ratio τ = sum($H_{d,y}$)/sum($H_{r,y}$) (black, dimensionless, right axis). The full curves correspond to the measured values (2005-2020), and the interrupted curves to predicted values (2006-2100) according to scenarios RCP 2.6 (left figures) and RCP 8.5 (right figures).

3.3.2 Dew and rain events period

Preprints (www.preprints.org) | NOT PEER-REVIEWED | Posted: 24 October 2022 doi:10.20944/preprints202210.0357.v1

Given the importance of the time period between dew and rain events for plants and small living beings [45-46], one investigates below this parameter for rain, dew, and dew plus rain. For that purpose, one considers first the histogram of rain, dew and rain plus dew events (Fig. 10). Two important parameters can be extracted, the mean time period between events, θ_0 (in days) and the maximum time period between events, θ_M (in days). The values are listed in Table 5 for dew, rain and dew + rain.

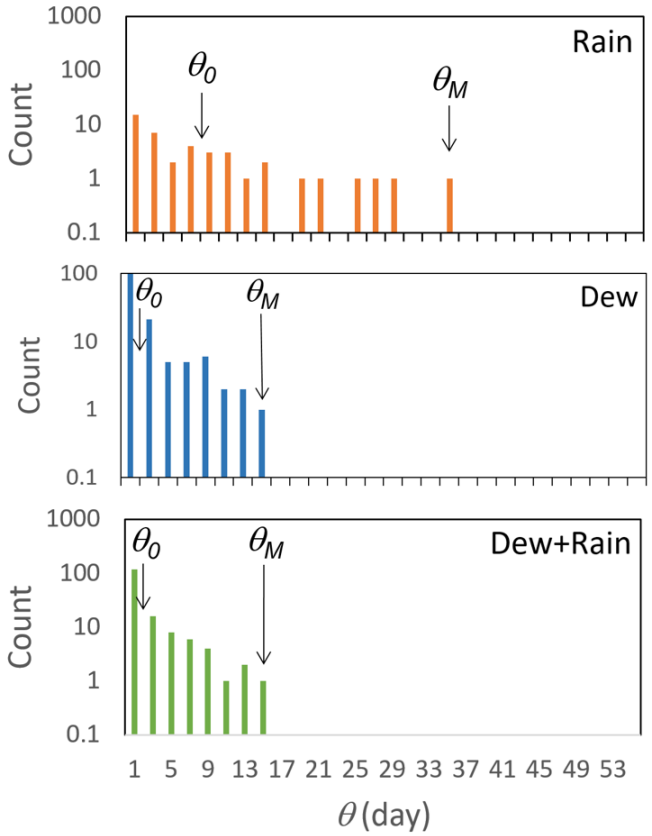

Figure 10. Typical histograms of time period θ (day) beetween (a) rain events, (b) dew events (c) rain and dew events, for the Fuerte Ventura site (Year 2010). θ_0 is the mean time and θ_M is the maximum time between events. Note that some dew or rain events can diseappear in the histogram dew + rain because dew or rain events can occur during the dew or rain time periods.

Preprints (www.preprints.org) | NOT PEER-REVIEWED | Posted: 24 October 2022 doi:10.20944/preprints202210.0357.v1

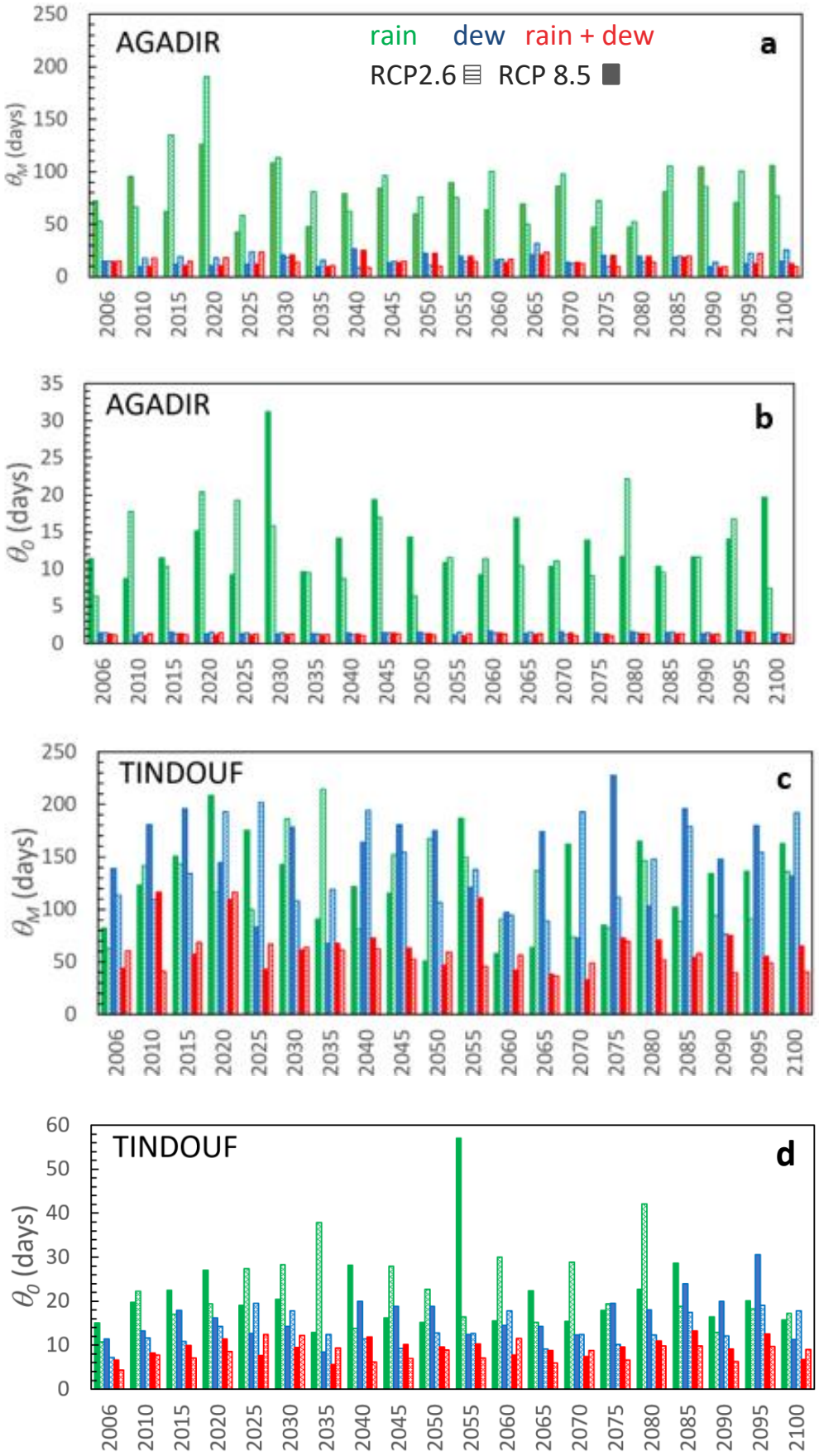

Preprints (www.preprints.org) | NOT PEER-REVIEWED | Posted: 24 October 2022 doi:10.20944/preprints202210.0357.v1

Figure 11. Evolution of lapse times θ_M and θ_0 (yearly values, 5 years timestep) for Agadir (a-b) and Tindouf (c-d) sites from 2006 to 2100), according with both RCP scenarios (RCP 2.6: textured bars; RCP 8.5: full bars). Rain is green, dew is blue and rain + dew is red.

As an example, the evolutions of yearly θ_0 and θ_M for rain, dew, and rain + dew events, are reported in Fig. 11 between 2006 and 2100 using a 5 years' time step for two sites, Agadir and Tindouf. These sites exhibit differences in climates and location (coast, continent), see Fig. 1. As expected, the lapse time between events is smaller for dew than for rain, with smaller differences in the continental site of Tindouf. This is a general observation (see Tables 3 and 4). A similar result was obtained in 4 countries in southern Africa by [30]. In addition, the timescale for mean and maximum time period between events is much larger for rain than for dew, a difference which can reach two orders of magnitudes. For both scenarios RCPs 2.6 and 8.5, θ_M (Table 5) exhibits large standard deviations in the yearly means. For rain, according to both scenarios RCPs 2.6/8.5, one notes that the maximum of times θ_M can exceed 4 months in 5 locations: Agadir (190/120 days), Rabat (79/127 days), Béchar (214/208 days), Gran Canaria (167/176 days), Fuerte Ventura (242/280 days). For dew, θ_M is maximum in the Sahara desert (Béchar and Tindouf, 174/183 and 202/228 days, respectively) and in islands (Gran Canaria, 157/193 days). The combination dew + rain allows the mean period without precipitation to be reduced by a factor of three. The conclusions are similar for the mean lapse time θ_0 (see Table 5). One notes, unsurprisingly, that the dew events determine the behavior of the dew + rain time period (Table 5).

θ_M (days)		R			D			R+D		
	Airport	**Mean**	**Min**	**Max**	**Mean**	**Min**	**Max**	**Mean**	**Min**	**Max**
RCP2.6	Gran Canaria	83.4±33.7	45.0	167.6	115.0±27.0	70.3	157.5	62.5±23.7	32.3	126.7
	Fuerteventura	135.1±45.1	74.4	242.3	40.6±12.4	26.0	79.0	36.5±10.7	21.9	57.8
	Agadir	87.5±32.3	49.9	190.6	17.2±5.5	8.8	31.6	15.0±4.6	8.8	24.0
	Tindouf	122.8±39.8	63.0	214.6	140.5±39.3	76.5	201.9	57.5±16.7	36.8	116.5
	Marrakech	40.7±10.6	22.6	62.6	26.6±7.7	13.0	41.9	20.6±4.4	12.8	26.5
	Casablanca	47.6±17.4	25.9	98.5	9.6±2.7	5.8	15.4	7.6±2.3	4.9	12.9
	Rabat	39.7±13.0	23.1	78.9	9.3±1.7	6.8	14.0	6.7±1.5	4.4	10.3
	Tanger	41.5±12.3	25.5	70.1	13.3±3.1	9.8	23.9	10.4±2.6	6.1	15.8
	Fès	26.2±6.4	15.6	38.1	18.5±7.4	10.9	39.9	12.2±3.1	6.5	19.9
	Al-Hoceima	36.9±9.9	20.5	60.1	14.2± 3.7	9.6	22.6	12.9±3.2	8.9	19.9
	Béchar	63.3±22.8	29.6	116.5	107.2±29.1	66.8	173.9	44.2±14.1	27.6	74.1
	Oujda	36.1±10.5	20.0	57.3	13.6±3.1	7.9	21.6	11.7±3.3	7.6	17.9
	Tlemcen	38.9±11.0	23.4	57.1	11.5±3.4	5.8	18.0	10.7±3.4	5.8	18.0
	Oran	38.6±11.6	24.8	70.1	10.8±2.4	6.8	16.8	8.8±2.6	4.9	14.3
	Statistics	**59.9 ± 40.4**	**15.6**	**242.3**	**39.1 ± 46.7**	**5.8**	**201.9**	**22.7 ± 20.8**	**4.4**	**126.7**
RCP8.5	Gran Canaria	91.6±30.9	41.6	176.6	98.6±31.6	60.3	193.6	62±20.6	37.0	105.5
	Fuerteventura	152.4±54.2	71.4	280.0	41.0±14.9	23.0	84.9	37.3±16.0	19.5	84.9
	Agadir	77.2±22.7	42.6	126.3	16.0±4.8	9.5	26.6	15.5±4.9	8.9	25.1
	Tindouf	125.9±43.5	51.1	208.6	148.0±44.0	67.8	227.9	65.0±23.3	33.0	116.4
	Marrakech	50.3±17.9	24.8	98.3	30.7±11.6	16.9	60.9	23.4±6.6	15.8	42.9

Preprints (www.preprints.org) | NOT PEER-REVIEWED | Posted: 24 October 2022 doi:10.20944/preprints202210.0357.v1

	Casablanca	56.4±21.6	31.1	93.5	9.4±2.0	5.8	13.5	8.3±2.4	4.9	12.8
	Rabat	58.7±26.1	24.4	127.1	8.7±2.0	5.9	13.5	6.7±1.7	4.6	11.8
	Tanger	53.8±22.4	27.4	90.9	14.8±3.4	8.8	22.6	12.3±3.9	6.8	22.6
	Fès	28.2±7.1	16.7	48.0	23.5±11.8	11.0	60.5	14.4±5.5	7.8	30.0
	Al-Hoceima	37.1±11.5	20.3	68.3	17.1±4.9	10.8	30.0	14.4±3.3	9.6	23.6
	Béchar	64.4±19.1	35.3	111.3	114.8±38.8	65.5	182.9	45.6±16.6	21.9	83.8
	Oujda	40.6±13.8	21.9	70.3	15.1±4.7	8.5	24.0	13.9±4.5	7.9	23.3
	Tlemcen	41.3±13.7	22.0	68.0	11.1±3.6	6.9	22.8	9.9±2.4	5.9	14.8
	Oran	51.8±20.2	25.5	96.6	11.2±2.6	6.8	19.8	8.5±2.2	5.5	14.8
	Statistics	**66.4 ± 42.8**	**16.7**	**280.0**	**40.0 ± 47.8**	**5.8**	**227.9**	**24.1 ± 22.2**	**4.6**	**116.4**

θ_0 (days)		R			D			R+D		
	Airport	**Mean**	**Min**	**Max**	**Mean**	**Min**	**Max**	**Mean**	**Min**	**Max**
RCP2.6	Gran Canaria	14.7±5.3	8.6	27.8	11.3±3.4	7.4	22.4	6.3±1.4	4.4	9.9
	Fuerteventura	27.3±9.3	12.8	44.9	3.3±0.6	2.6	5.0	3.0±0.5	2.3	4.3
	Agadir	12.6±4.7	6.3	22.2	1.4±0.1	1.2	1.6	1.2±0.1	1.0	1.5
	Tindouf	22.3±8.1	10.8	42.1	13.4±3.5	7.2	19.6	8.4±2.1	4.4	12.5
	Marrakech	5.4±1.3	3.2	8.8	2.1±0.3	1.3	2.8	1.5±0.2	1.0	1.9
	Casablanca	4.5±0.9	3.1	6.2	1.0±0.1	0.8	1.2	0.8±0.1	0.7	0.9
	Rabat	3.8±0.7	2.3	5.3	1.0±0.1	0.8	1.2	0.7±0.1	0.6	0.9
	Tanger	3.4±0.6	2.2	4.6	1.6±0.2	1.2	2.0	1.0±0.1	0.8	1.3
	Fès	2.6±0.4	1.6	3.3	1.1±0.1	0.9	1.2	0.9±0.1	0.7	1.0
	Al-Hoceima	3.7±0.6	2.6	4.7	1.0±0.1	0.9	1.2	0.9±0.1	0.7	1.0
	Béchar	9.7±1.7	6.5	13.3	5.0±1.2	3.4	8.0	3.4±0.7	2.5	4.7
	Oujda	3.7±0.6	2.4	4.9	1.5±0.2	1.1	1.7	1.0±0.1	0.8	1.2
	Tlemcen	3.6±0.6	2.2	4.8	1.2±0.1	1.0	1.3	0.9±0.1	0.7	1.0
	Oran	3.7±0.6	2.8	5.1	1.4±0.2	1.2	1.7	1.0±0.1	0.8	1.1
	Statistics	**8.6 ± 8.5**	**1.6**	**44.9**	**3.3 ± 4.1**	**0.8**	**22.4**	**2.2 ± 2.4**	**0.6**	**12.5**
RCP8.5	Gran Canaria	17.9±4.0	13.0	28.8	10.0±2.0	6.26	15.08	6.4±1.0	4.4	8.4
	Fuerteventura	38.3±22.3	18.9	115.1	3.1±0.3	2.60	3.65	2.9±0.3	2.5	3.3
	Agadir	13.7±5.1	8.7	31.2	1.4±0.2	1.12	1.72	1.3±0.1	1.0	1.5
	Tindouf	21.4±9.3	12.9	57.1	16.4±5.0	8.42	30.59	9.3±2.0	5.6	13.2
	Marrakech	6.0±1.0	4.2	8.0	2.4±0.4	1.51	3.40	1.7±0.3	1.1	2.4
	Casablanca	4.9±0.7	3.6	6.1	1.0±0.1	0.86	1.23	0.8±0.1	0.7	1.0
	Rabat	4.2±0.7	2.6	5.4	1.0±0.1	0.86	1.13	0.7±0.1	0.6	0.8
	Tanger	3.5±0.6	2.0	4.4	1.7±0.2	1.36	2.10	1.1±0.1	0.8	1.3
	Fès	2.8±0.4	2.0	3.8	1.1±0.2	0.82	1.53	0.9±0.1	0.7	1.3
	Al-Hoceima	3.8±0.6	2.5	4.7	1.2±0.1	0.98	1.40	1.0±0.1	0.8	1.2
	Béchar	10.9±2.5	7.8	16.4	5.2±1.1	3.26	7.36	3.6±0.7	2.6	5.1
	Oujda	3.8±0.7	2.7	5.1	1.5±0.2	1.14	1.85	1.1±0.1	0.8	1.4
	Tlemcen	3.8±0.7	2.8	5.7	1.2±0.1	0.98	1.45	0.9±0.1	0.7	1.1
	Oran	3.9±0.6	2.8	5.1	1.4±0.1	1.13	1.55	1.0±0.1	0.8	1.1
	Statistics	**9.9 ± 11.8**	**2**	**115.1**	**3.5 ± 4.5**	**0.8**	**30.6**	**2.3 ± 2.5**	**0.6**	**13.2**

Preprints (www.preprints.org) | NOT PEER-REVIEWED | Posted: 24 October 2022 doi:10.20944/preprints202210.0357.v1

Table 5. Yearly mean, minimum and maximum values for maximum time θ_M and mean time θ_0 (days) between events, considering all sites and according to both RCP scenarios between years 2006 and 2100.

3.2.3. Potential (*PET*) and real (*ET*) evapotranspirations

Moisture from atmosphere plays an important role in sustaining life in arid or semi-arid climates. For example, Pan et al. [47] concluded on the mutual enhanced effect between dew and artificially revegetation ecosystems in the arid desert ecosystem in Shapotou (China). Li et al. [48-49], Zhuang and Zhao [50] determined that dewfall can be presented as a critical source of water in deserts environments allowing to establish the sustainability of sand to stabilize planted vegetation [50]. Kidron [51] suspected dew to be a necessary water source for cyanobacteria. Büdel et al. [45] concluded a study by noting that the time frequency of rain precipitations is more important than their amount for sustaining the biological soil crusts.

The ratio between the monthly potential evapotranspiration amount (*PET*) and monthly dew yield ($H_{d,i}$) is therefore of importance and worth of investigation during the dry period (April to October). In Supplementary Materials is drawn (Figure SM2) the ratio between *PET* and $H_{d,i}$ for 4 future years (25 years step) according to the projections of the climate models RCP 2.6 and RCP 8.5. The Atlas mountain range appears as a topographic barrier that delimits two different climate behaviors. West of the mountains, the Atlantic coast benefits from oceanic moisture inputs where the $PET/H_{d,i}$ ratio can be much less than 50. Depending on the months of the dry period, this coastal zone, which also extends over the Mediterranean coast, is restricted to the immediate vicinity of the coasts. In the middle of the dry period (June, July, August), the Atlas area is characterized by an absence of dew production. In mid-season months (April, May, September, October), the $PET/H_{d,i}$ ratio can reach a value up to 300 in this area.

The trend of the $PET/H_{d,i}$ ratio strongly depends on the value of the RCP climate scenario. RCP 2.6 leads to a stable evolution between 2025 and 2100, with values $PET/H_{d,i} < 50$ in the inland, in agreement with [27]. The ratio can however reach 100 or even 150 on the southern coast of the country (south of Agadir up to the Mauritania boarder). The RCP 8.5 scenario, which exhibits a noticeable increase in ambient temperature over the century, leads to greater potential evapotranspiration and a stagnation or even a light decrease in dew yields (Fig. 6). $PET/H_{d,i}$ values can thus exceed 100 over a large part of the studied area, in particular on the Atlantic and Mediterranean coasts. The $PET/H_{d,i}$ ratio can no longer be evaluated ($H_{d,i} \rightarrow 0$) when moving to the east and south-east of the Atlas massif where the lack of relative humidity leads to a drying of the air mass and an absence of dew (Fig. 2b).

Considering now the actual evapotranspiration *ET*, with $ET \leq PET$ according to Eqs. 9-12, the comparison between *ET* and $H_{d,i}$ (Fig. 12) during the hottest months of the year show the potential interest of dew for organisms and plants living in these areas under high stress water. In August (RCP 2.6), $ET/H_{d,i} < 30$ corresponds to 18.9% (2025), 12.5% (2050), 8.6% (2075) and 15.6% (2100) of the studied area. For RCP 8.5 (July), $ET/H_{d,i} < 30$ is observed for 9.5%

Preprints (www.preprints.org) | NOT PEER-REVIEWED | Posted: 24 October 2022 doi:10.20944/preprints202210.0357.v1

(2025), 22.4% (2050), 12.3% (2075) and 27.4% (2100) of the studied area. The evolution corresponds to an *ET* increase due to the rise of the ambient temperature and the decrease of *RH*. For $ET/H_{d,i} < 10$, the area values are 7.7% ± 2.5% (RCP 2.6) and 12.0% ± 6.8% (RCP 8.5). These values highlight the interest for irrigation of native and little plants with small root zone area, which limits evaporation.

April

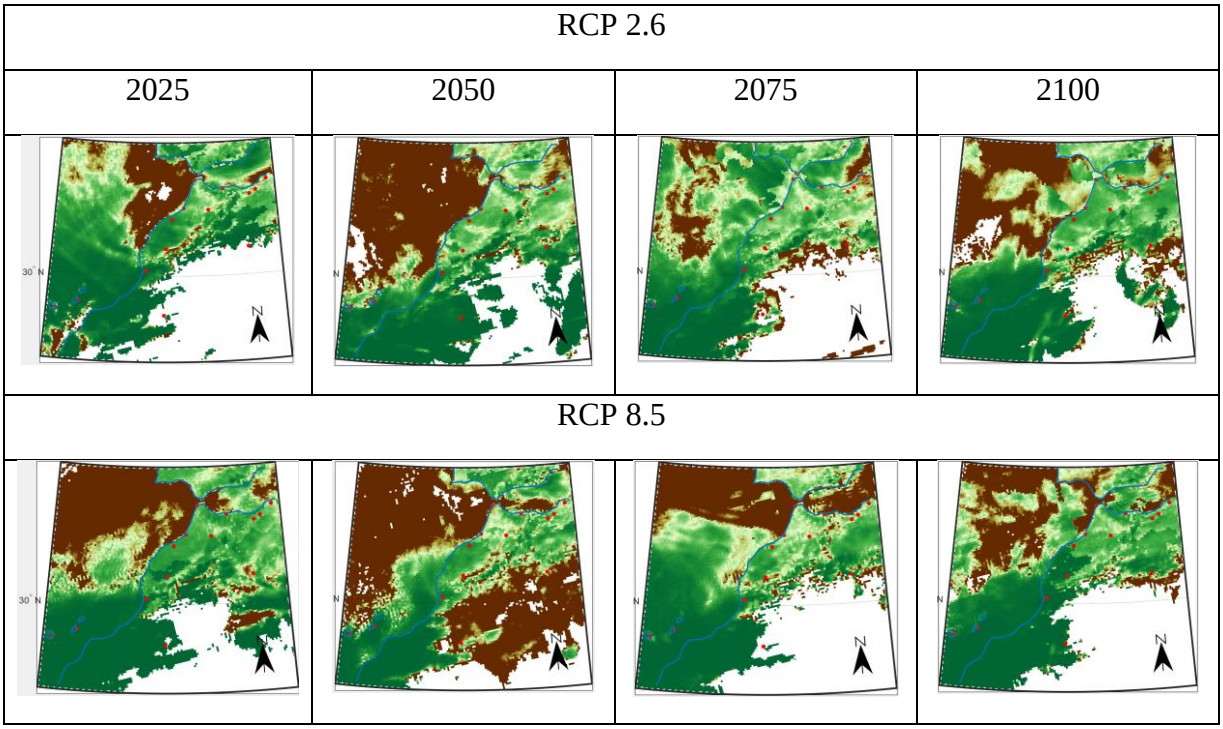

May

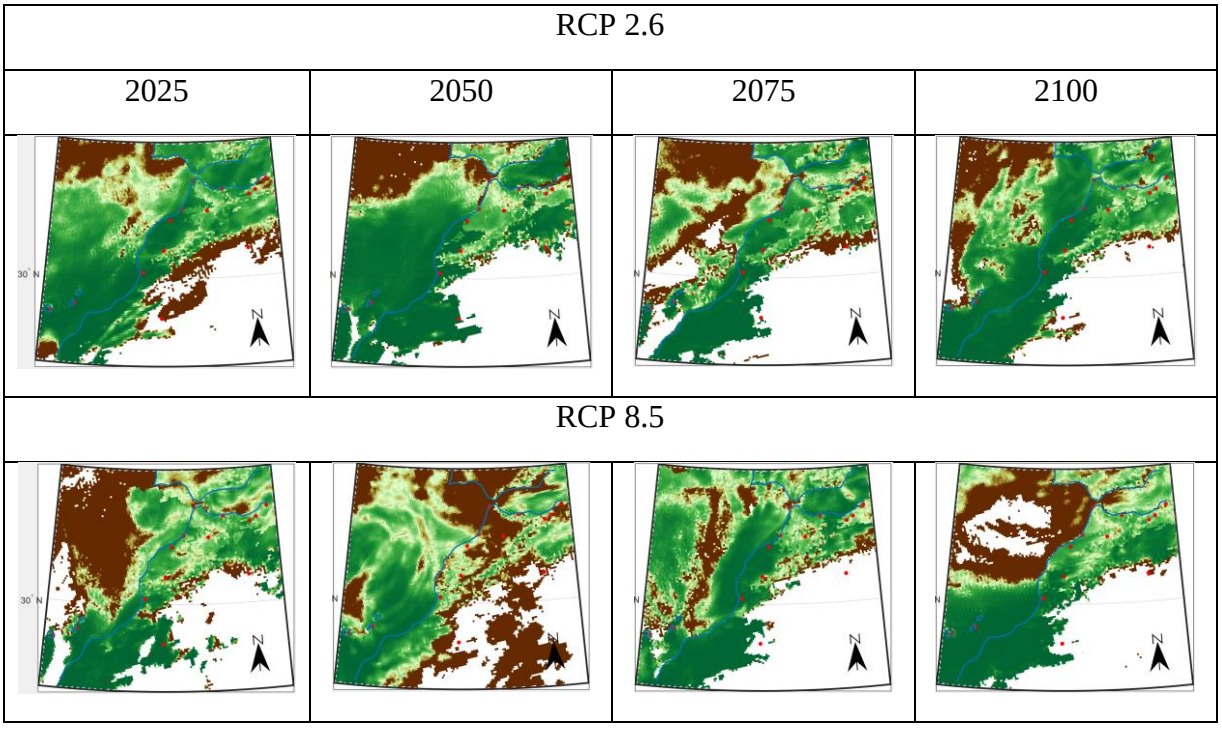

June

Preprints (www.preprints.org) | NOT PEER-REVIEWED | Posted: 24 October 2022 doi:10.20944/preprints202210.0357.v1

RCP 2.6			
2025	2050	2075	2100
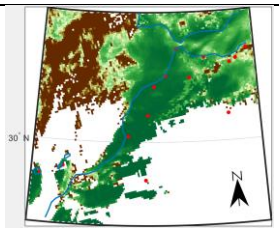	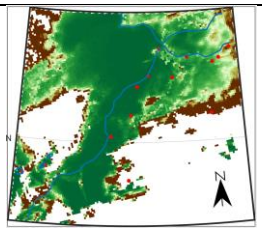	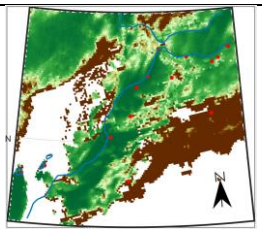	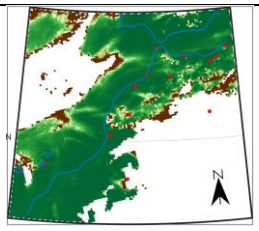
RCP 8.5			
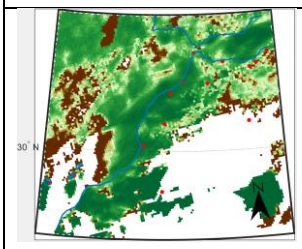	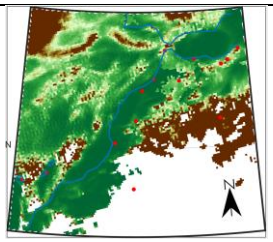	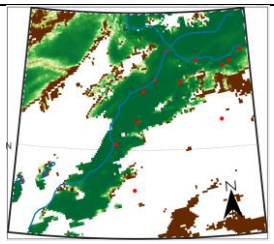	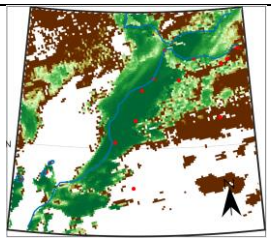

July

RCP 2.6			
2025	2050	2075	2100
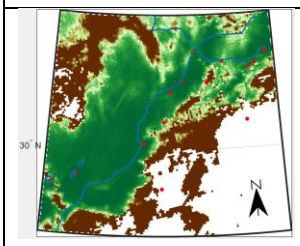	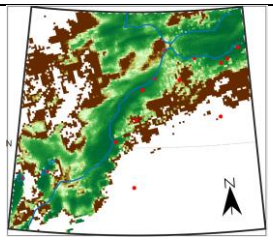	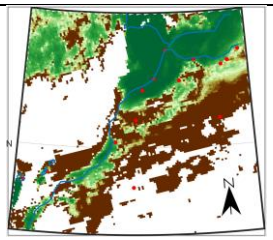	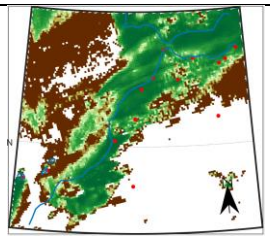
RCP 8.5			
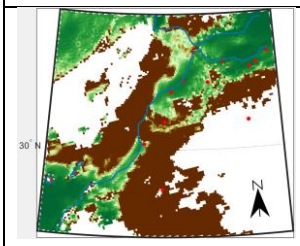	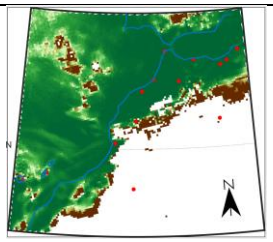	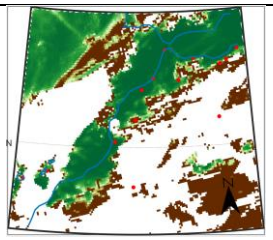	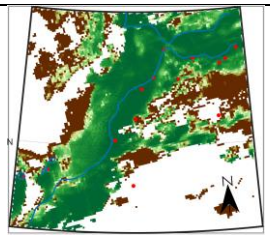

August

RCP 2.6			
2025	2050	2075	2100

Preprints (www.preprints.org) | NOT PEER-REVIEWED | Posted: 24 October 2022 doi:10.20944/preprints202210.0357.v1

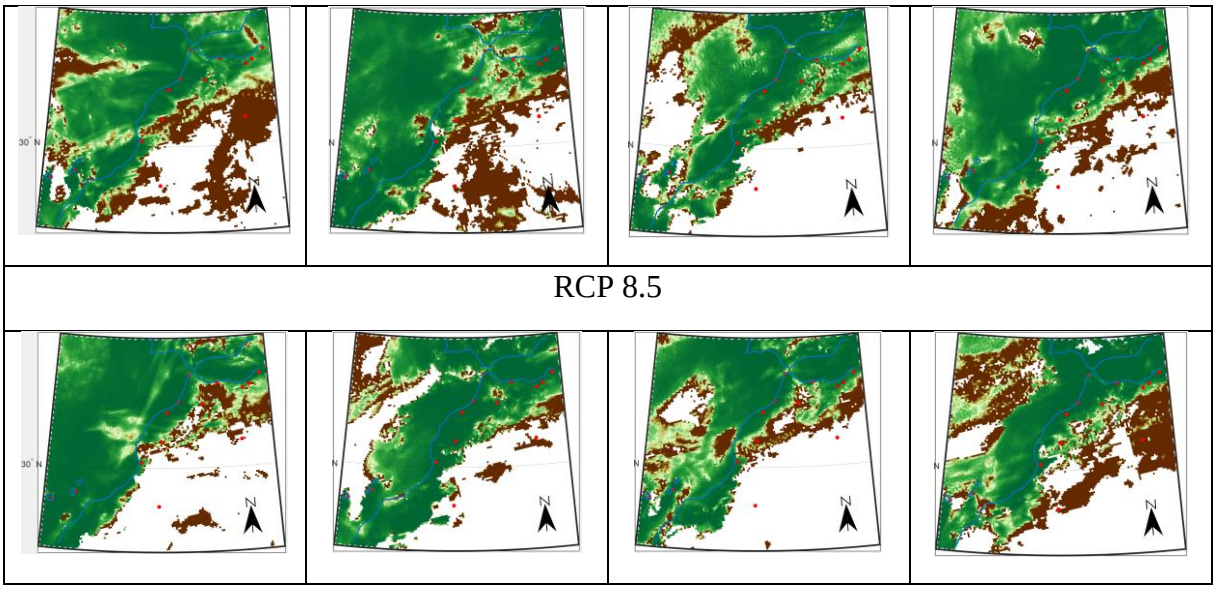

RCP 8.5

September

RCP 2.6

2025	2050	2075	2100

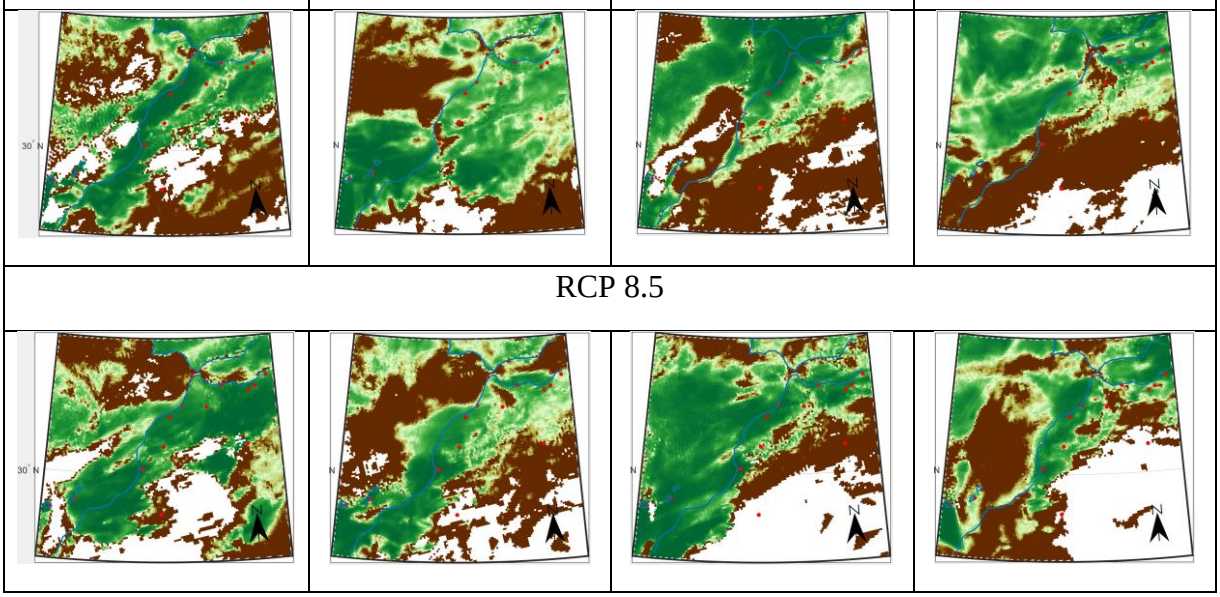

RCP 8.5

October

RCP 2.6

2025	2050	2075	2100

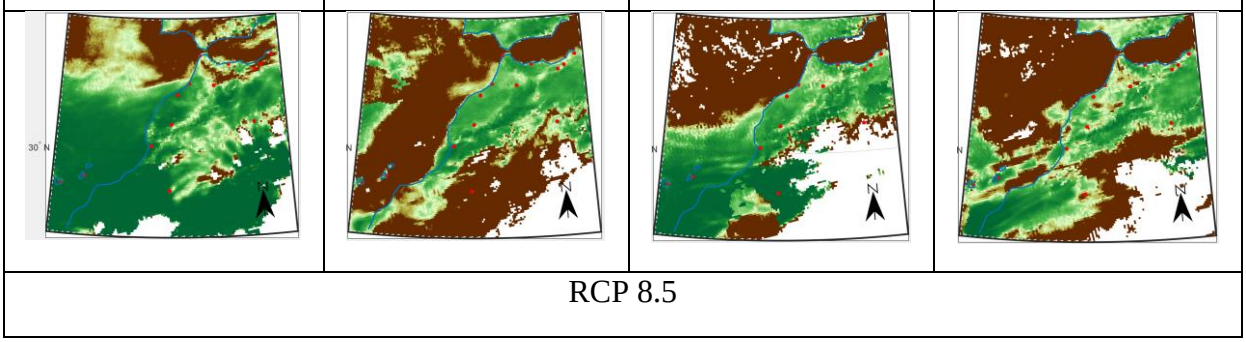

RCP 8.5

Preprints (www.preprints.org) | NOT PEER-REVIEWED | Posted: 24 October 2022 doi:10.20944/preprints202210.0357.v1

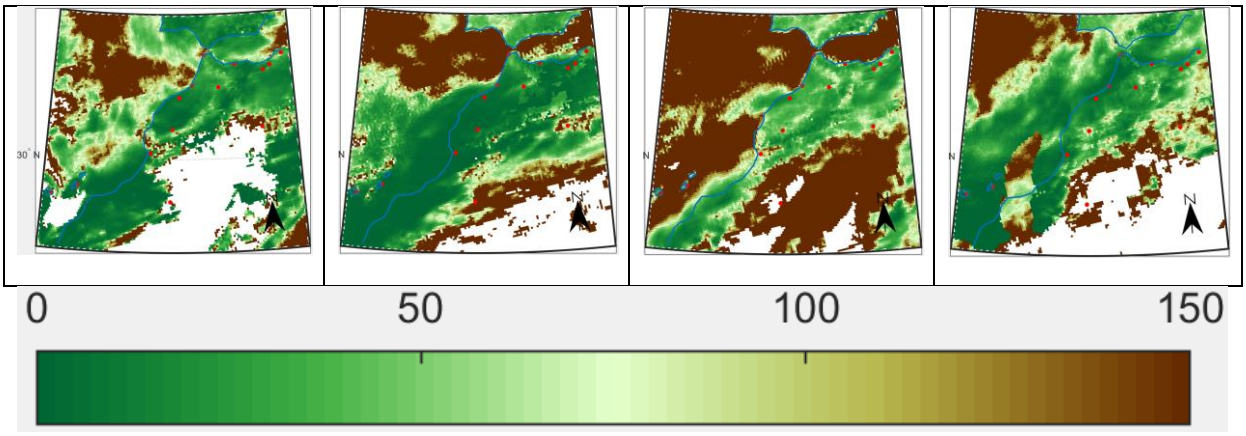

Figure 12. Ratio of monthly actual evapotranspiration and monthly dew yield ($ET/H_{d,i}$) for 4 specific years (2025, 2050, 2075, 2100) according to the projections of RCPs 2.6 and 8.5 climate models. The study is concerned with the driest period (April to October). The white pixels, mainly located S and SW, correspond to $H_{d,i}$ = 0 mm.mth^{-1}, thus $ET/H_d \rightarrow \infty$. The resolution is 12.5 × 12.5 km². Red points: Meteo stations as described in Table 1 and Fig.1.

3.4. Chemical composition

3.4.1 Previous studies

An investigation of the chemistry and biology of dew and rainwater has been reported by [18] in Mirleft (S-Morocco), a site typical of an arid environment. This work showed the following: (i) Presence of significant concentration in dew and rain of total dissolved solids, mainly due to the deposition of sea salts. (ii) Near constant neutral pH for dew and rain water. (iii) High dew and rain electric conductivity, related to the large concentration of dissolved solids. (iv) Acidity of the CO_2, SO_x and NO_x compounds neutralized by Ca^{2+} and K^+, which gives an alkaline character to dew and rainwater. (v) Balanced electro-neutrality, confirming that the analyzed ions are representative. (vi) Chemical and biological characteristics of dew and rainwater compatible with drinking water standards of the World Health Organization (WHO) after disinfection to eliminate the possible pathogenic germs present in the solutions.

3.4.2 Chemical composition: a new approach

In this section one reexamines the above data by taking into account the effect of dilution and motion of air masses. These parameters can be modified in the future, in particular dew and rain amounts are expected to decrease (see section 3.2.1) leading to change in water composition. In contrast to the previous study [18] where the means were calculated as arithmetical means [52], in the present analysis the data are volume weighted means (VWM), giving more representative values for water accumulated in a tank. The obtained value is in general close to the median value.

The volume mean is computed from the following relation:

Preprints (www.preprints.org) | NOT PEER-REVIEWED | Posted: 24 October 2022 doi:10.20944/preprints202210.0357.v1

$$VWM[X] = \frac{\sum_{i=1}^{N}(V_i X_i)}{\sum_{i=1}^{N} V_i} \quad (20)$$

where X represents the variable to be analyzed (ion concentration, electrical conductivity) and X_i and V_i are, respectively, the variable value and the water sample volume for sample i.

The data of [18] are concerned with the chemical composition of dew (17 samples) and rain (8 samples) collected at Mirleft on a standard condenser 1 m × 1 m, inclined at 30° horizontal, thermally isolated from below and covered with a low-density polyethylene foil. In this foil are imbedded a few % of TiO_2 and $BaSO_4$ microbeads, plus a surfactant insoluble with water ([53-54]; manufactured by OPUR [55]).

The materials and methods to collect and analyze water can be found in [18]. Only a summary is presented here. Dew and rainwater (not filtered) were collected in sterilized polyethylene flasks placed in a cold enclosure (temperature below 20 °C) for further analysis. pH and electrical conductivity (EC) measurements were performed on site just after water collection. They are concerned with (dew) 130 data (EC) and 133 data (pH) and (rain) 25 data for EC and pH. The following data were obtained for the samples analyzed later: chemical concentrations for the cations (Na^+, K^+, Ca^{2+}, Zn^{2+}, Cu^{2+}, Mg^{2+}, Pb^{2+} and anions (HCO_3^-, Cl^-, SO_4^{2-}, NO_3^-). The quality control/analysis (QA/QC) of measurements consists to obtain exact and reproducible results, the analysis sequence including various QC tests.

For a given dew or rain water sample, the chemical compositions have been evaluated by classical statistical indicators (min, max, mean and standard deviation). As noted above, in the present analysis the mean is volume weighted mean (VWM). Data are compared with water from a local spring water, “Sidi Ali” (the composition was taken in 2006 from [56]). “Sidi Ali” is a weakly mineralized spring water, collected in the village of Tarmilate (middle Atlas Mountains, 33°23′5″N 6°7′13″ W), a few kilometers from the town of Oulmès at 1100 m elevation (578 km from Mirleft). Water comes from precipitations and is naturally filtered by the rocks and enriched over time with mineral salts.

3.4.2.1. Dew, rain and spring water ionic concentrations

The analytical results are reported in Table 6 and the VWM concentrations of ions and cations are shown in Fig.13. For a given water sample, chemical compositions (dew or rain, in $mEq.L^{-1}$) have been evaluated by classical statistical indicators (min, max, arithmetical mean and standard deviation) and the volume weighted mean (VWM). The arithmetical mean values from [18] are generally found close to the VWM values. For dew, the major ions are by far Na^+ and Cl^-. The result is the same, but to a lesser extent, with rain. For both dew and rain, the major cations are in the order $Na^+ >> Ca^{2+} > Mg^{2+} > K^+$. The composition of the spring water “Sidi Ali” is similar, with less Na^+ and Cl^- ions concentration and an inversion between Mg^{2+} and Ca^{2+}. For dew, the concentration of Cu^{2+}, Zn^{2+} and Pb^{2+} are negligible (<

Preprints (www.preprints.org) | NOT PEER-REVIEWED | Posted: 24 October 2022 doi:10.20944/preprints202210.0357.v1

0.05 mEq.L^{-1}). For dew and rain samples, two major anions are present Cl^- >> HCO_3^- >> SO_4^{2-} ~ NO_3^-. For spring water, one notes a high concentration of SO_4^{2-} (0.979 mEq.L^{-1}), about 3 times greater than in dew and rain.

For all analyzed ions, the concentrations of cations and anions are compatible with WHO potable water standards [57-58]. As discussed by [18], the large concentration of Na^+, Mg^{2+} and Cl^- in dew and rain samples can be attributed to a marine origin of these ions, due to the close vicinity of the sampling site with the Atlantic Ocean (a specific analysis with air mass trajectories is given in sections 3.4.2.3 and 3.4.2.4).

Dew and rain samples exhibit large total hardness values (TH, French degree °f), computed from Ca^{2+} and Mg^{2+} in mg.L^{-1}. The mean VWM values are $TH_{dew} = 16.9$ (min/max: 6.1/42.7) and $TH_{rain} = 9.9$ (min/max: 2.4/20.8). These large values are mainly due to the high concentration of calcium, of terrestrial origin, and magnesium, of marine origin. Hence dew water can be considered as a medium hard water ($15 < TH\ (°f) \leq 30$) and rain water is considered as fresh water ($7 < TH\ (°f) \leq 15$). For the spring water Sidi Ali, $TH_{Sidi\_Ali} = 6.7$, making it a very fresh water ($0 < TH(°f) \leq 7$).

		DEW (17 samples)					RAIN (8 samples)					Sidi Ali
		Min	Max	Mean	SD	VWM	Min	Max	Mean	SD	VWM	(£)
	V (mL)	33	334	156	99	-	100	2230	977	649	-	-
	TH (°f)	6.1	42.7	19.6	9.8	16.9	2.4	20.8	12.0	6.0	9.9	6.7
	pH(*)	6.8	7.9	7.5	0.3	7.5	6.7	7.1	6.9	0.2	6.9	6.5 ± 0.30
	pH(**)	6.8	7.9	7.5	0.3	-	6.5	7.2	6.9	0.2	-	-
	EC (µS.cm^{-1}) (*)	59	2920	1243	936	1075	15	406	186	142	73	280 ± 20
	EC (µS.cm^{-1}) ($)	39	4230	759	755	-	15	2081	276	269	-	-
Cations	Ca^{2+}	0.831	5.398	2.442	1.162	2.005	0.368	2.526	1.540	0.655	1.447	0.624 ± 0.095
mEq.L^{-1}	Mg^{2+}	0.354	3.133	1.478	0.937	1.366	0.114	2.200	0.851	0.667	0.529	0.708 ± 0.305
	K^+	0.046	0.477	0.258	0.135	0.212	0.018	0.248	0.131	0.076	0.096	0.077 ± 0.018
	Na^+	0.766	14.280	5.476	4.757	5.384	0.265	8.193	2.990	3.022	2.306	0.992 ± 0.222
	Cu^{2+}	0.001	0.033	0.016	0.010	0.014	-	-	-	-	-	-
	Zn^{2+}	0.000	1.400	0.141	0.355	0.145	-	-	-	-	-	-
	Pb^{2+}	0.00004	0.00008	0.00005	0.00001	0.00005	-	-	-	-	-	-
Anions	Cl^-	1.716	19.539	8.573	5.740	8.056	0.699	10.908	4.147	3.342	2.777	0.542 ± 0.141
mEq.L^{-1}	NO_3^-	0.088	0.464	0.257	0.111	0.230	0.039	0.490	0.226	0.131	0.210	0.003 ± 0.002
	SO_4^{2-}	0.115	1.127	0.419	0.275	0.366	0.026	0.995	0.351	0.276	0.338	0.979 ± 0.625
	HCO_3^-	1.000	1.400	1.141	0.150	1.117	-	-	-	-	-	1.234 ± 0.251

(*) chemical analysis samples: 17 for dew and 8 for rain

(**) all samples: 133 for dew and 27 for rain

($) all samples: 130 for dew and 15 for rain

(£) calculated from [56]

Preprints (www.preprints.org) | NOT PEER-REVIEWED | Posted: 24 October 2022 doi:10.20944/preprints202210.0357.v1

Table 6. Chemical analysis of dew and rain samples from Mirleft (Morocco, May 1, 2007 – April 30, 2008). The concentrations are expressed in mEq.L^{-1} and are compared with a local spring water ("Sidi Ali", produced at Oulmès, Morocco). The electric conductivity is at 25 °C.

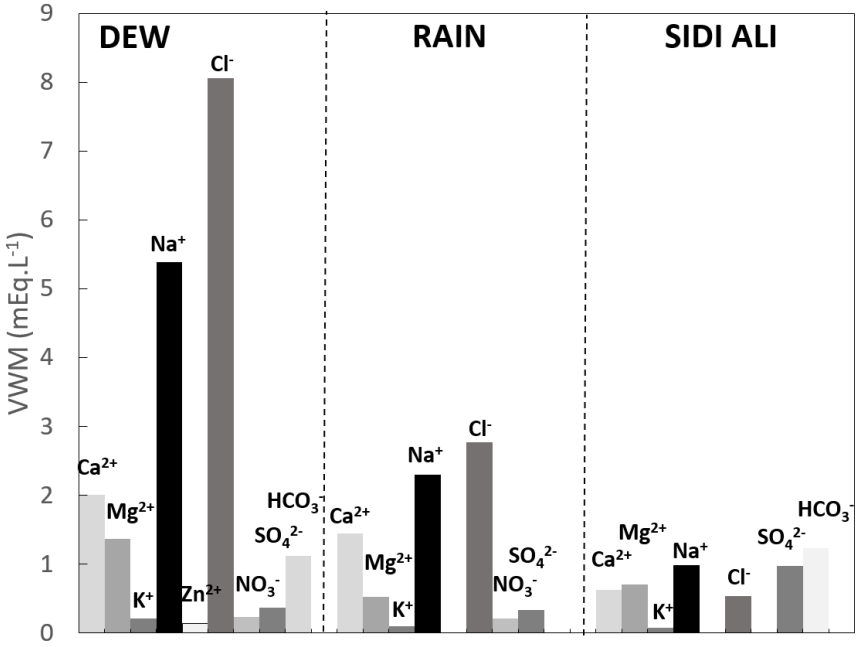

Figure 13. Dew and rain water mean concentrations (mEq.L^{-1}, VWM). The Sidi Ali spring water composition is given for comparison.

3.4.2.2. Effect of water volume

Figure 14a correlates the electric conductivity for dew and rain, corresponding to the total ion concentration in water, with the collected volume per unit surface, *h* (mm). Notes the different scales and *h*-ranges for dew and rain. The EC decrease with *h* is weaker in rain for *h* > 2 mm, where the dilution effect with the deposited aerosols becomes to saturate at the concentration of ions in solution in the rain drops. In Fig. 14 ions of ocean and continent origin in dew and rain are also shown. Quite generally, smaller volumes match with larger ionic concentrations, corresponding to the same dilution effect observed in EC [59-60]. This effect implicitly means that the concentration of aerosols and gases deposited from the ambient air keeps roughly constant in the atmosphere. This is of course not always the case and the ionic concentration and EC should also depend on the air mass trajectories, as discussed in sections 3.4.2.3 (dew) and 3.4.2.5 (rain). Exceptions to the general dilution effect are thus observed. Note that the concentration of ions of gas adsorption origin (SO_4^{2-}, NO_3^-) exhibit a weaker tendency to decrease with volume because there is nearly no dilution effect, the kinetics of

 doi:10.20944/preprints202210.0357.v1

adsorption being very fast. The next sections will however show that this dilution effect is dominant in the analyses.

Windspeed indirectly modifies the dew yield by the effect of dilution (Fig. 14f), with higher wind speed giving lower dew yield and higher EC or ion concentration. This effect is inverted with respect to rain yield, where higher wind speed corresponds to higher water yield and lower EC or ion concentration. One notes that the dilution effect is, however, also present in rain for the small rain yields, which complicates the analysis (see Section 3.4.2.4 for further discussions).

Preprints (www.preprints.org) | NOT PEER-REVIEWED | Posted: 24 October 2022 doi:10.20944/preprints202210.0357.v1

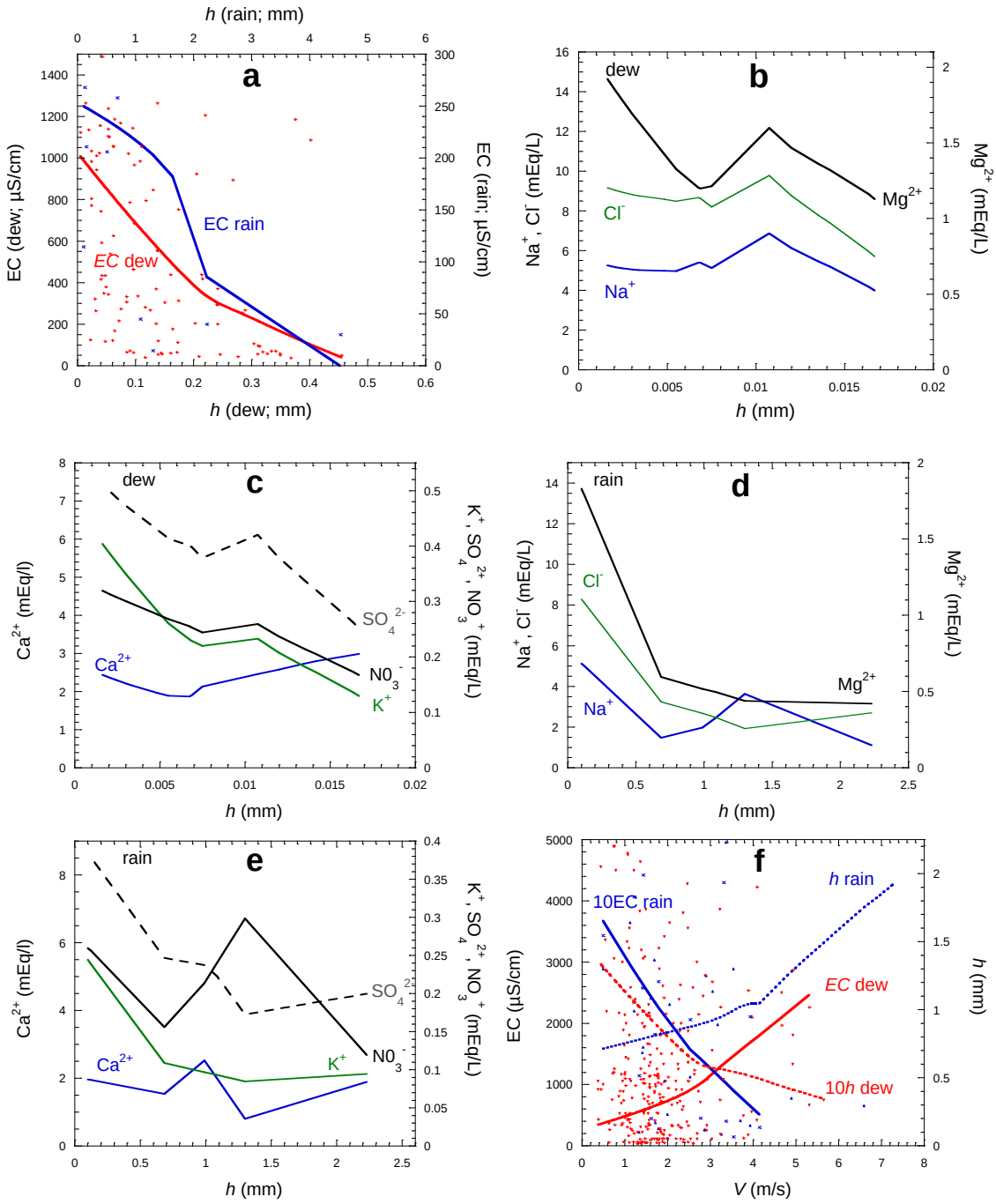

Figure 14. (a) Variation of dew and rain electric conductivity EC with dew or rain volume per unit surface area, *h* (mm). Dew: red, lower abscissa; rain: blue, higher abscissa. (b) Correlations with *h* of the sea salts concentrations in dew (Na^+, Cl^-: left ordinate; Mg^{2+}: right ordinate). (c) Same, but with continental ions concentrations (Ca^{2+}: left ordinate; K^+, NO_3^-, SO_4^{2-}: right ordinate). (d) Same as (b) for rain ions of sea origin. (e) Same as (c) for rain ions of continental origin. (f) Correlated variations of EC and *h* with wind speed *V* at 10 m elevation for dew and rain. All curves in (a-f) are smoothed fit of single values.

Preprints (www.preprints.org) | NOT PEER-REVIEWED | Posted: 24 October 2022 doi:10.20944/preprints202210.0357.v1

3.4.2.3. Dew air flux backward trajectories

The backward trajectory of a point of the atmosphere can be calculated by the Hysplit model [61]. One can thus determine the path of a particle of air during the hours or days that preceded its analysis. We have used this model to determine the backward trajectories for the study site [62] during the 24 hours preceding the day of dew collection, taken at 6:00 in the morning.

The air mass that crosses Mirleft is characterized by a mixed origin, oceanic and continental (desert). Dew volume and composition is mostly affected by the relative humidity, aerosols and dissolved gases in the atmospheric boundary layer. We thus consider the path of air masses at 500, 100, 10 m above the collection site. Since dew does not form when wind comes from desert because *RH* is too small (Fig. 2b), its chemical composition will be mainly of ocean or mixed ocean / continental origin. Some typical backward trajectories are shown in Fig. 15.

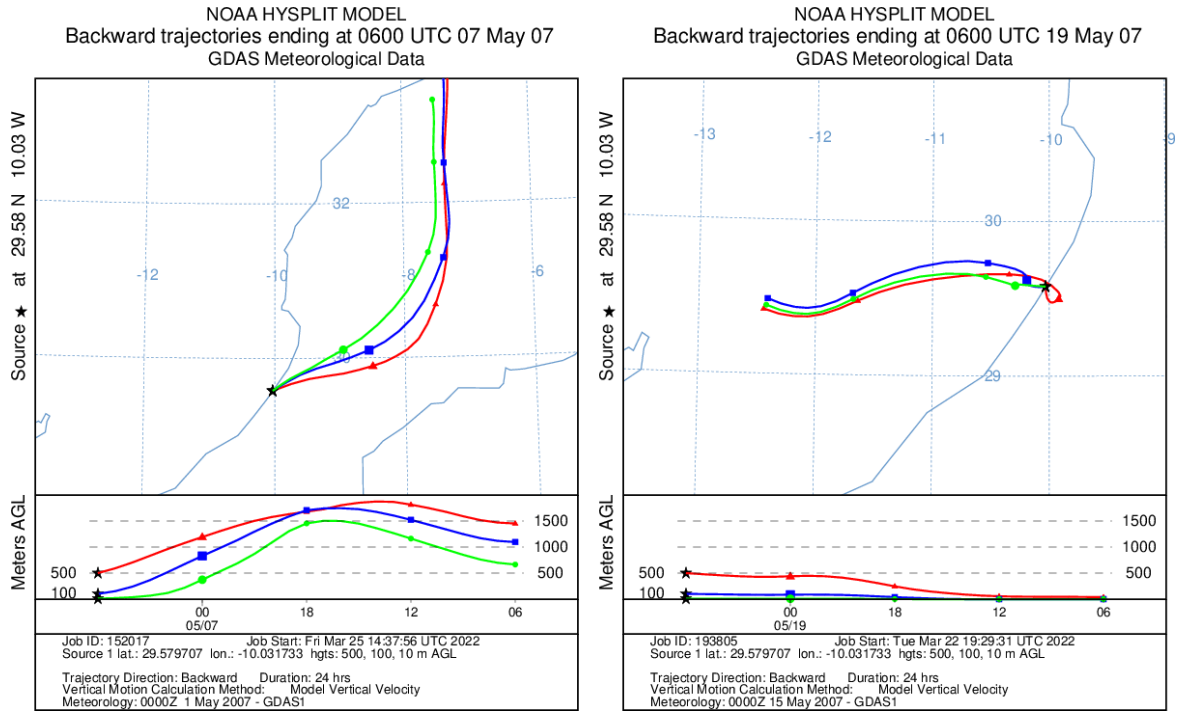

Preprints (www.preprints.org) | NOT PEER-REVIEWED | Posted: 24 October 2022 doi:10.20944/preprints202210.0357.v1

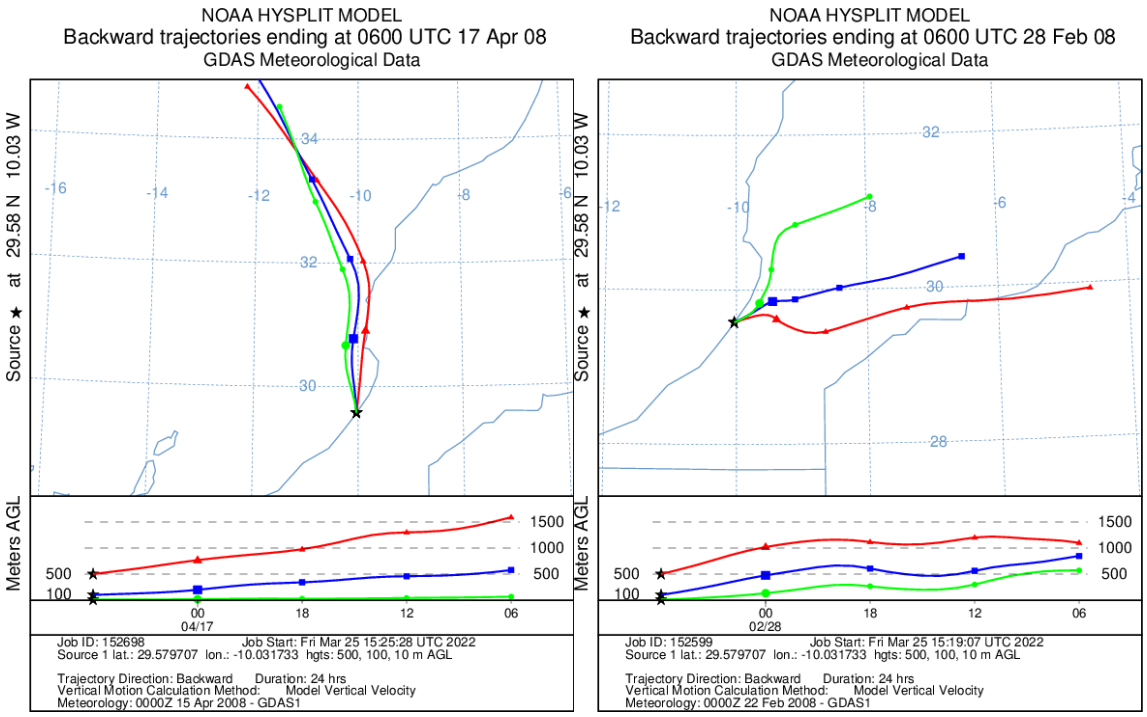

Figure 15. Some typical 24 hours low elevation air mass backward trajectories from Mirleft at 6:00 corresponding to dew events. Data are every 6 hours. From [62].

Figure 16a reports the concentration of major ions of ocean origin (Na^+, Cl^-, Mg^{2+}) and the volume of dew per unit surface area (h) as a function of mean air mass direction during 24 h. It was checked that this mean direction was well correlated with the direction of air masses at 6:00. For humid air coming between W and N, the dew yield is substantial and the concentration of ocean ions corresponds to an effect of dilution, the largest volumes corresponding to smaller concentrations. For directions between N and E, the concentrations of ocean ions rather follow the dew volume, with the largest volumes, the largest ions concentrations, as discussed in section 3.4.2.2 and Fig. 14. The lowest data correspond to directions 10 - 45° as in Fig. 15 on 28 Feb. 2008. Here one sees that the air masses are following a continental path, thus explaining the low dew yield related to a low RH and low, ocean-dominant, ion concentrations. For other continental directions larger than 50°, the dew yield is higher with larger ocean ion concentration, meaning that the air masses before 24h should have also come from the ocean.

Figure 16b is concerned with major ions of continental or anthropic origin (Ca^{2+}, K^+, SO_4^{2-}, NO_3^-). The main variation in concentration of aerosols (Ca^{2+}, K^+) is a dilution effect, with higher concentrations for smaller volumes. Concerning gases (SO_4^{2-}, NO_3^-), in majority of anthropic origin (although SO_4^{2-} can also be of marine origin), their concentration is less sensitive to the effect of dilution because of their fast absorption dynamics. The variation with air mass direction is different from that of ions of ocean origin and rather follows an increase for directions larger than 22°, corresponding to continental origins.

Preprints (www.preprints.org) | NOT PEER-REVIEWED | Posted: 24 October 2022 doi:10.20944/preprints202210.0357.v1

The variation of EC and pH are shown in Fig. 16c, together with the dew yield *h*. The EC value roughly follows a dilution effect. Concerning pH, its value generally increases when the dew volume decreases. It corresponds to the highest concentrations of Ca^{2+} and K^{+}, ions which react with the acidic ions SO_4^{2-} and NO_3^{-} to increase the pH.

In the future, scenarios RCP 2.6 and RCP 8.5 lead to a decrease in dew yield but should not lead to main changes (Fig. 6). It means that moist air, which gives rise to dew condensation, will continue to flow from the ocean. One therefore does not expect major changes in the chemistry of dew.

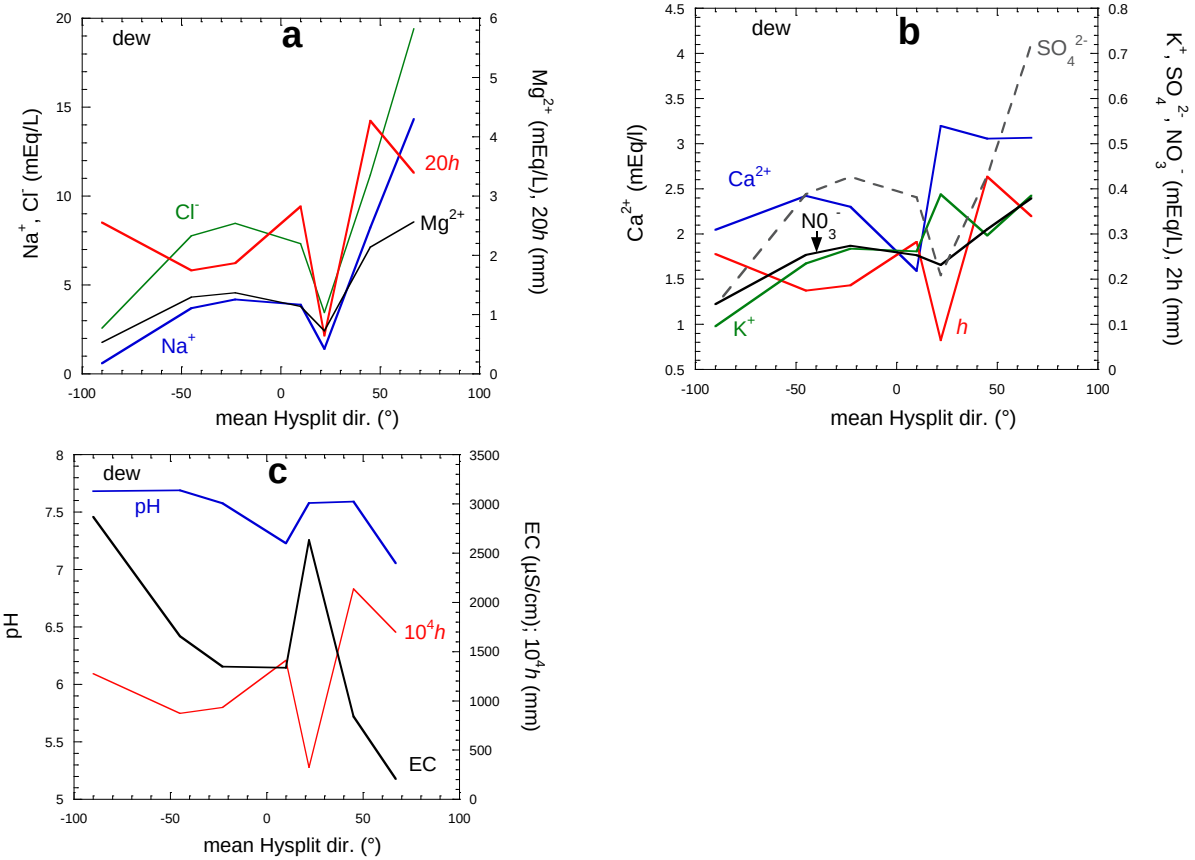

Figure 16. Dew main ions concentrations, electric conductivity, pH and volume per unit area *h* (mm) correlated variations with the 24 h. mean air mass directions from Hysplit. (a) Concentration of main ions of ocean origin (Na^{+}, Cl^{-}, Mg^{2+}, in $mEq.L^{-1}$). (b) Concentration of main ions of continental origin (Ca^{2+}, K^{+}, SO_4^{2-}, NO_3^{-}, in $mEq.L^{-1}$). (c) EC and pH. All curves are smoothed fit of single values.

3.4.2.4. Dew seasonal variations

In Figs. 17c and 17d are reported, respectively, the monthly evolution of ions (Na^{+}, Cl^{-}, Mg^{2+}) of sea origin and ions (Ca^{2+}, K^{+}, SO_4^{2-}, NO_3^{-}) of continental origin, together with the rain yield *h*. The concentrations are seen to simply follow a dilution effect, that is, higher concentration for lower dew yield. The season dependence is thus the inverse of the dewfall

Preprints (www.preprints.org) | NOT PEER-REVIEWED | Posted: 24 October 2022 doi:10.20944/preprints202210.0357.v1

volume evolution, smaller ion concentrations in winter and higher in summer. Figure 17e shows that the dew pH is rather stable with time around ≈ 7, while the electric conductivity obviously follows the major ions concentration behavior, being smaller in winter and larger in summer.

One expects for the future evolution described by the scenarios RCP 2.6 and RCP 8.5 a decrease in dew yield. This decrease is not related to a major change in the air masses. One therefore expects with a lower dew volume a higher concentrations of ions from aerosols (Na^+, Cl^-, $Ca^{2+,}$ K^+). The other ions coming mainly from anthropic gases (SO_4^{2-}, NO_3^-), it is probable that their concentration will also increase.

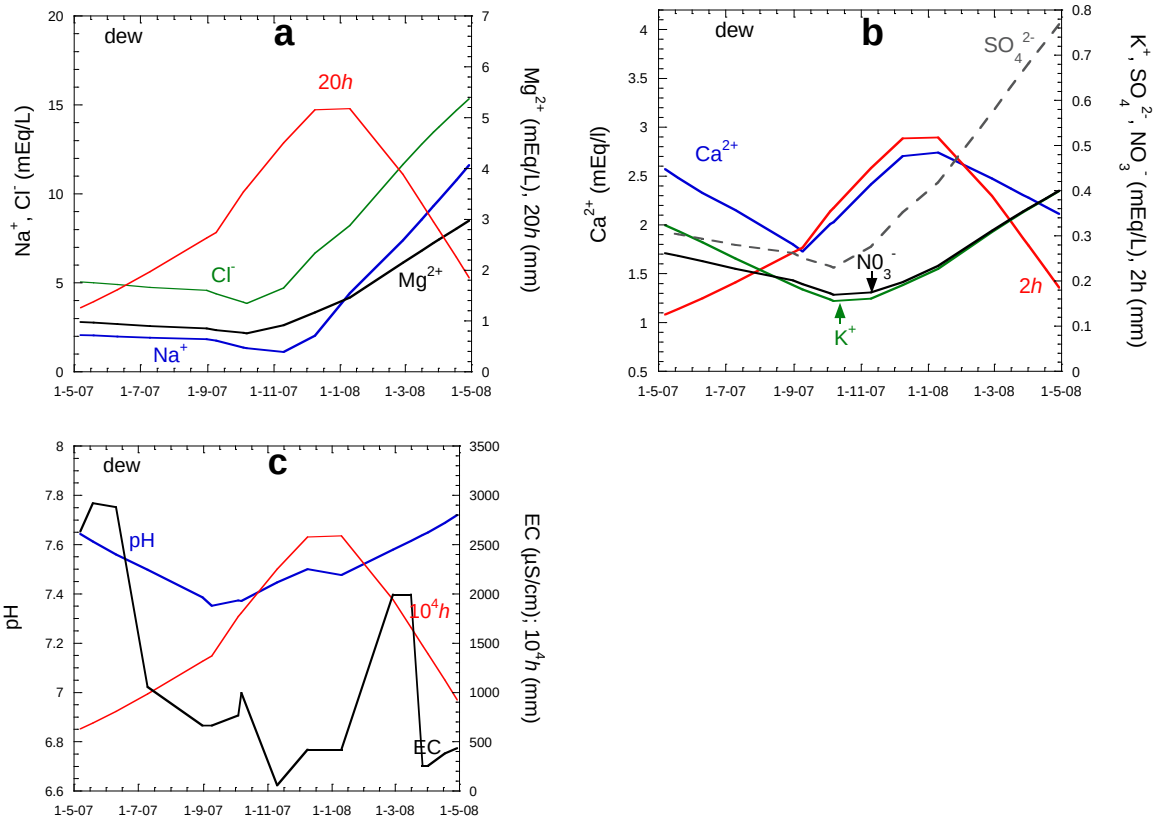

Figure 17. Evolution of dew ions. (a) Comparative evolution of sea ions concentrations and dew volume per unit area *h* (mm). (b) Same as (a) but with continental ions. (c) Evolution of electric conductivity EC (µS.cm^{-1}), pH and *h* (mm). All curves are smoothed fit of single values.

3.4.2.5. Rain air flux backward trajectories

Morocco is on the south border of the mid-latitude area of depression systems issued from Newfound Land and Iceland, which habitually cross the North Atlantic Ocean. Rain yields are then low and gradually decrease from north to south. It results that wind during rainy days

Preprints (www.preprints.org) | NOT PEER-REVIEWED | Posted: 24 October 2022 doi:10.20944/preprints202210.0357.v1

mainly comes from S to N. Figure 18 reports some typical backward trajectories corresponding to rain events.

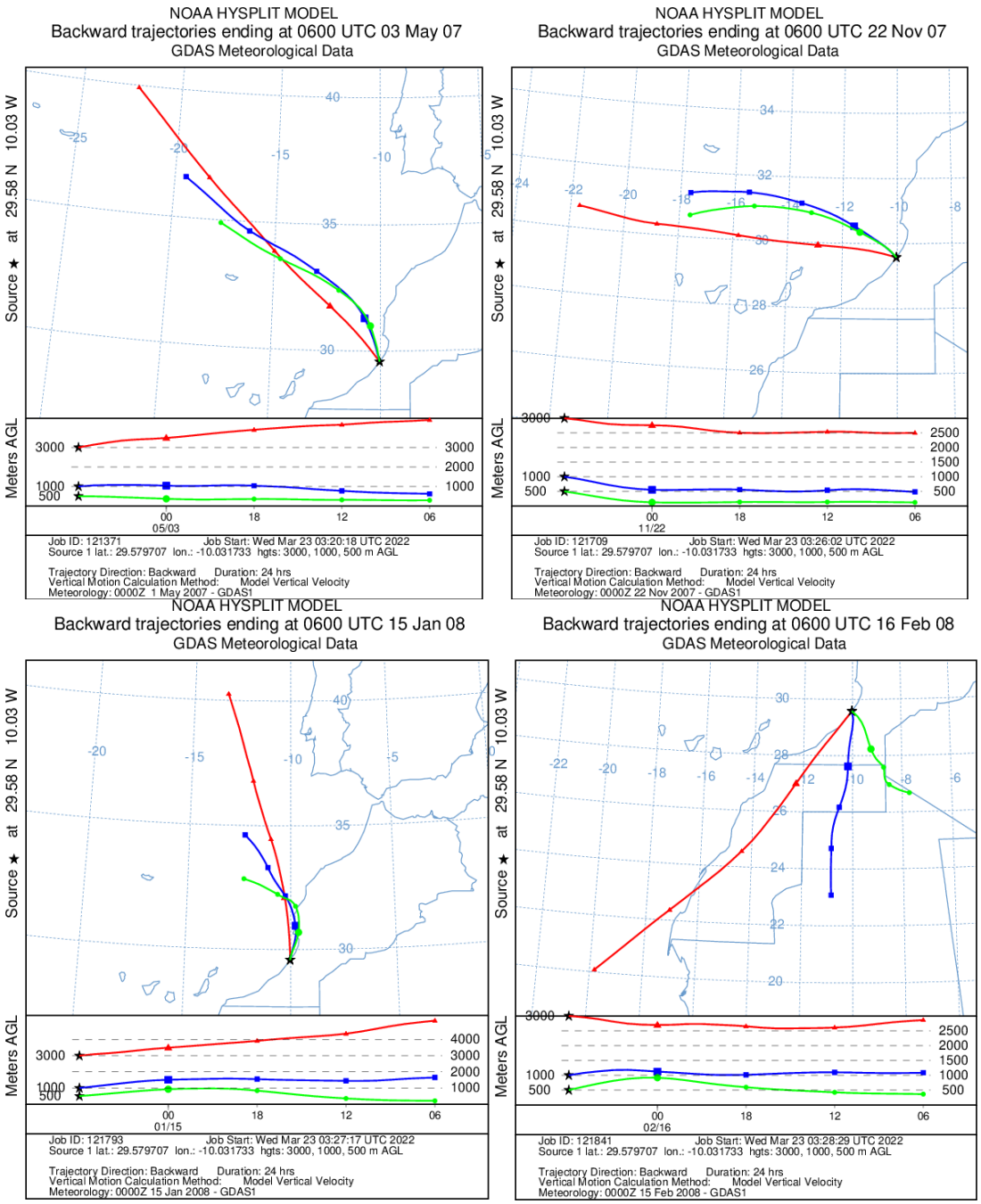

Figure 18. Some typical 24 hours low elevation air mass backward trajectories from Mirleft at 6:00 (data every 6 hours) corresponding to rain events. From [62].

The variation of concentration of ions of marine origin (Na^+, Cl^-, Mg^{2+}) together with the rain volume per surface area, *h*, is presented in Fig. 19a as a function of mean air mass direction

Preprints (www.preprints.org) | NOT PEER-REVIEWED | Posted: 24 October 2022 doi:10.20944/preprints202210.0357.v1

during the last 24 h. As for dew, the main variation is due to an effect of dilution, with higher ion concentration when *h* is lower. Figure 19b, concerning the ions (Ca^{2+}, K^+, SO_4^{2-}, NO_3^-) of continental origin (except some marine contribution for SO_4^{2-}) shows a dilution effect for the aerosols contribution (Ca^{2+}, K^+), the same effect seen with the ions of marine origin, with the higher rain volume, the lower ion concentration. Ions coming from gas adsorption (SO_4^{2-}, NO_3^-) display a less marked dependence with the rain volume as discussed above in section 3.4.2.2.

The rain EC and pH variations with mean air masses directions (Fig. 19c) show a general dissolution dependence on rain volume *h.* EC and pH values have a tendency to rise when the rain volume decreases. It corresponds to a dissolution effect and, for the pH, a higher concentration of Ca^{2+} and K^+ ions, reacting with the acidic ions SO_4^{2-} and NO_3^-, increases the pH value.

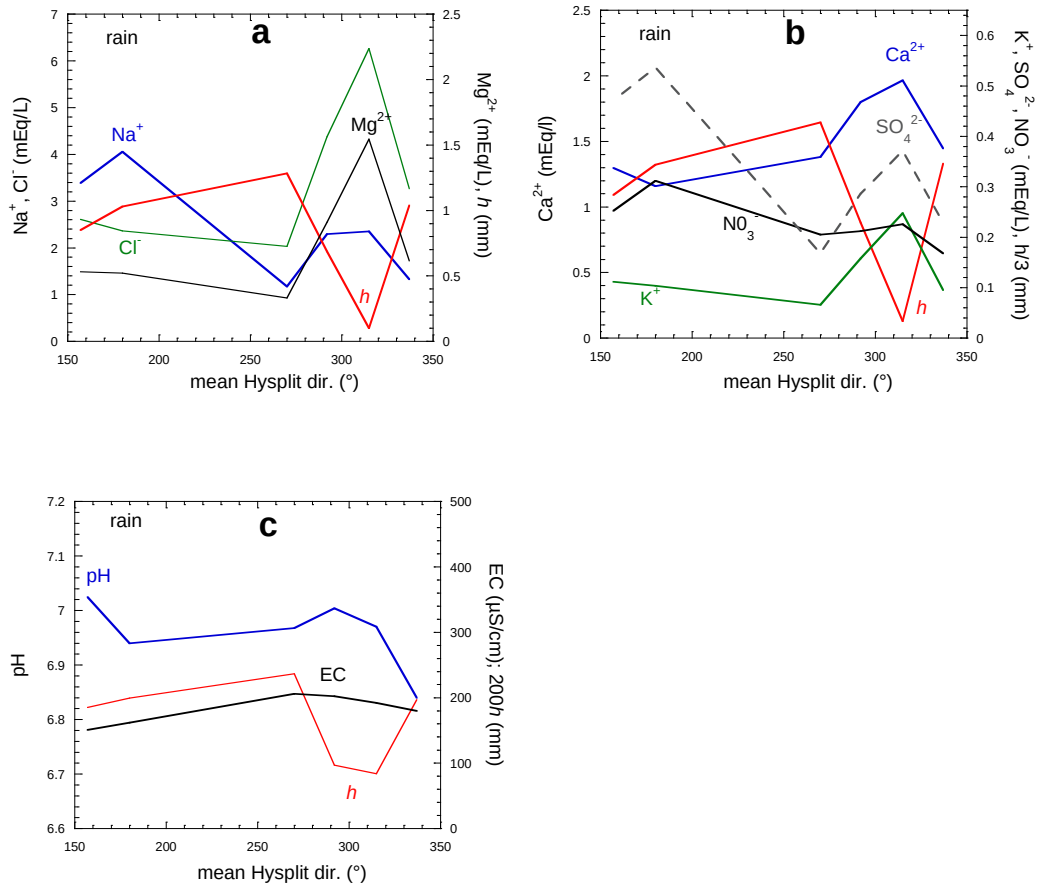

Figure 19. Correlated variations with the 24 h. mean air mass directions from Hysplit, of main rain ions concentrations, electric conductivity EC, pH and dew volume per unit area *h* (mm). (a) Concentration of main ions of ocean origin (Na^+, Cl^-, Mg^2) and *h*. (b) Concentration of main ions of continental origin (Ca^{2+}, K^+, SO_4^{2-}, NO_3^- and *h).* (c) EC, pH and *h* variation. All curves are smoothed fit of single values.

3.4.2.6. Rain seasonal variations and volume dependence

Preprints (www.preprints.org) | NOT PEER-REVIEWED | Posted: 24 October 2022 doi:10.20944/preprints202210.0357.v1

Although the number of analyzed rain samples is relatively low for ion concentrations, one can nevertheless draw some general conclusions. Figures 20a,b report, respectively, the evolution of ions (Na^+, Cl^-, Mg^{2+}) of sea origin and ions (Ca^{2+}, K^+, SO_4^{2-}, NO_3^-) of continental origin, together with the rain yield *h*. The concentrations are seen to simply follow the rain yield dependence, that is, higher concentration for smaller *h*. The season dependence is thus the inverse of the rainfall volume evolution, smaller ion concentrations in winter and higher in summer. Figure 20c shows that rain pH is rather stable around ≈ 7, while the electric conductivity roughly follows the total ion concentration behavior with rain yield, being smaller in winter and larger in summer.

The *future evolution* is driven by the scenarios RCP 2.6 and RCP 8.5. They lead to a decrease in rain volumes yield but should not lead to major changes in the pathways of depressions across the Ocean. One therefore expects with the lower rain volume higher concentrations of ions from aerosols (Na^+, Cl^-, Ca^{2+}, K^+). The other ions coming mainly from anthropic gases (SO_4^{2-}, NO_3^-), it is likely that their concentration will not decrease.

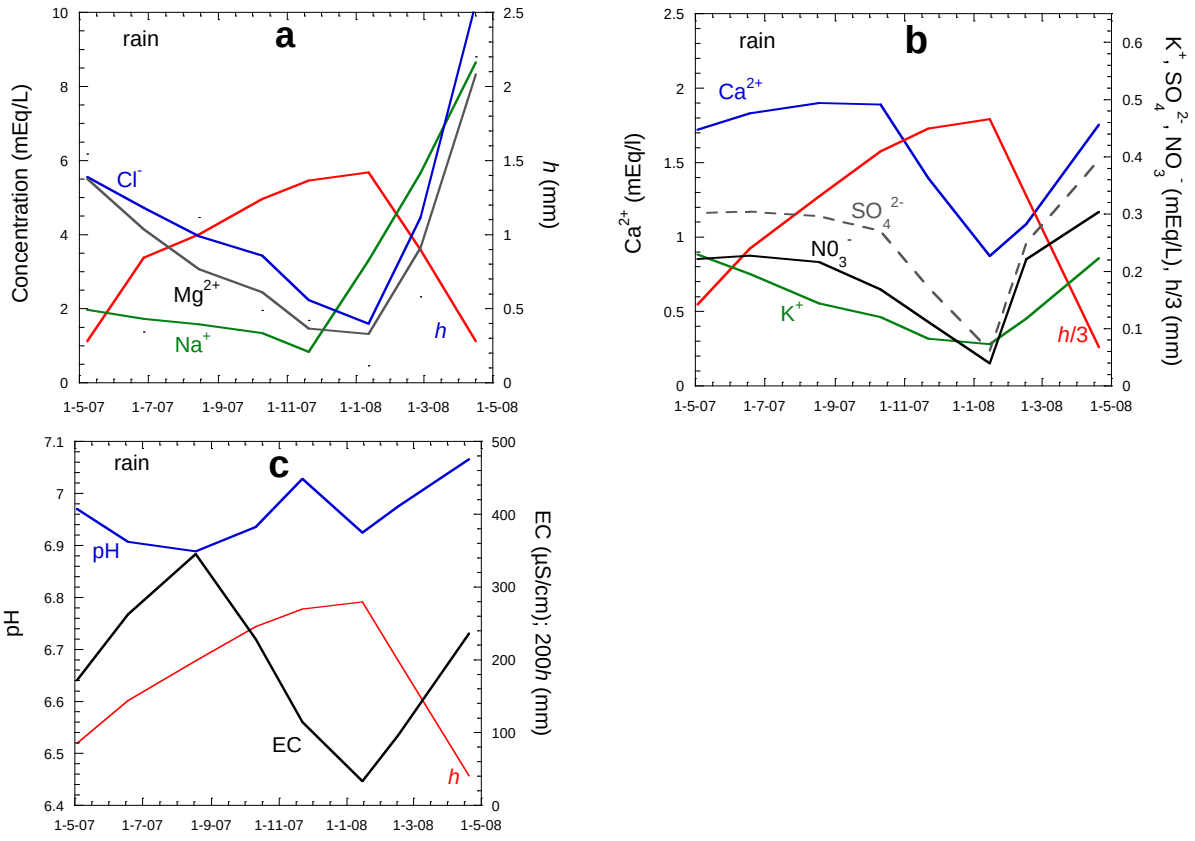

Figure 20. Evolution of rain ions. (a) Comparative evolution of sea anions and cations concentrations and rain volume per unit area *h* (mm). (b) Same as (a) but with continental ions. (c) Evolution of electric conductivity EC (µS.cm^{-1}), pH and rain volume per unit area *h* (mm). All curves are smoothed fit of single values.

Preprints (www.preprints.org) | NOT PEER-REVIEWED | Posted: 24 October 2022 doi:10.20944/preprints202210.0357.v1

4. Conclusion

This paper firstly aims to study the evolution of dew, rain and evapotranspiration in the NW of Africa (Morocco and a part of desert and coastal Algeria). The time periods are concerned with the past years 2005-2020 using existing data, and future years for the period 2020-2100. For the latter are used the low and high emissions representative concentration pathway (RCP) scenarios, RCP 2.6 and RCP 8.5.

One notes than the relative contribution of dew with respect to rain can reach 12% in the coastal and near coastal regions of SW Morocco (Agadir/Casablanca/Marrakech/Oujda) and NW regions of Algeria (Oran/Tlemcen). For desert sites such as Béchar and Tindouf, the cumulative dew/rain ratio presents values in the range 4 to 8%.

It appears that the evolution from 2005 to 2100 leads to a notable continuous decrease in rain precipitation. However, one notes for RCP 2.6 an increase of rainfall between 2030 and 2090 and later a decrease to zero. Concerning RCP 8.5, one observes a decrease on order of -14 mm.decade^{-1}. The last scenario seems to be more credible because the decrease is already existent since the beginning of years 2000. The amplitude of this decrease is maximum on the coast and on the foothills of Atlas. Only the extreme south of the country on the Mauritanian border could experience, with the RCP 8.5 scenario, a significant increase in rainfall.

One also observes a diminution in dew yields along a NW/SE axis. This decrease is strongly correlated with a corresponding decreasing in relative humidity (up to 7%). The areas from the Atlantic coast to the Saharan desert are gradually impacted by this reduction. Concerning the Sahara Desert, one also observes a decrease in dew yields, especially from the highlands (Atlas Mountains) towards SW. More generally, there is a tendency to see a reduction in dew yields with increasing distance from the sea, located W and N, correlated with a diminution in nocturnal relative humidity from NW to SE.

Concerning evapotranspirations, the increase of temperatures and the change of the mode of precipitations is a source of uncertainty. However, one can reasonably state that the potential evapotranspiration PET displays an increase over the century, weak for the scenario RCP 2.6 (+4.0 mm.decade^{-1}), larger for the scenario RCP 8.5 (+7.4 mm.decade^{-1}). This increase is related to the expected rise in ambient temperature. One also observes that the actual evapotranspiration ET is lower in 2100 than in 2006, with -15.8 mm.decade^{-1} for RCP 2.6. For RCP 8.5, an exceptional rainy month of May 2100 leads to ET(2100) > ET(2006) but during the century, the ET tendency rather shows a slow decrease.

When compared with the dew yield H_d, the potential evapotranspiration strongly depends on the value of the climate scenario. However, one can reasonably state that RCP 2.6 leads to stability between 2025 and 2100, with values PET/H_d < 50 in the inland, in agreement with [27]. The ratio can reach 100 or 150 on the southern coast of the area. The RCP 8.5 scenario unsurprisingly exhibits a greater potential evapotranspiration and a stagnation or even a light decrease in dew yields, leading to values of the ratio PET/$H_{d,i}$ > 100 over a large part of the territory, in particular on the Atlantic and Mediterranean coasts. Considering the comparison between the actual evapotranspiration ET as compared with dew yields, the ratio can reach ET/H_d < 30 for 10 to 20 % of the studied area, highlighting the potential interest of dew for

 doi:10.20944/preprints202210.0357.v1

organisms and plants living in these areas during the hottest months of the year. For ratios ET/H_d < 10, the concerned areas are near 8% (RCP 2.6) and 12 % (RCP 8.5).

The second part of the study was concerned with chemical data in dew and rain in the representative site of Mirleft (south Morocco). Dew and rain samples exhibit major cations in the order Na^+ > Ca^{2+} > Mg^{2+} > K^+, similar to the spring water "Sidi Ali". The ion concentration in rain and spring water is about two times less than in dew water. The concentrations of Cu^{2+}, Zn^{2+} and Pb^{2+} are negligible. For all analyzed ions, the concentrations of cations and anions are compatible with WHO standards for potable water. The large concentration of Na^+, Mg^{2+} and Cl^- in dew and rain samples can be attributed to the marine origin of these ions, due to the close vicinity of the sampling site with the Atlantic Ocean as confirmed by the air mass trajectories.

The main variation in concentration of aerosols (Na^+, Mg^{2+}, Cl^-, Ca^{2+}, K^+) is a dilution effect, with higher concentrations for smaller volumes. Concerning gases (SO_4^{2-}, NO_3^-), in majority of anthropic origin, their concentration is less sensitive to the effect of dilution because of their fast absorption dynamics. The seasonal variations of the ionic concentrations in dew and rain thus mainly follow a volume dilution dependence, with higher concentration for lower dew and rain volumes; it is thus the inverse of the water volume evolution, with smaller ion concentrations in winter and higher in summer. Due to the expected diminution in dew and rain volumes according to the RCPs 2.6 and 8.5, it is anticipated that the water ionic concentration of dew and rain will increase in the future.

Acknowledgments

References

1. Tramblay, Y., Badi, W., Driouech, F., El Adouni, S., Neppel, L., Servat, E., **2012**. Climate change impacts on extreme precipitation in Morocco. *Glob. Plan. change*, 82-83, 104-114.

2. Schilling, J., Hertig, E., Tramblay, Y., Scheffran, J., **2020**. Climate change vulnerability, water resources and social implications in North Africa. *Reg. Environmental Change*, 20, Article number 15.

3. Schilling, J., Freier, K.P., Hertig, E., Scheffran, J., **2012**. Climate change, vulnerability and adaptation in North Africa with focus on Morocco. *Agriculture, Ecosys. and Environ.*, 156, 12-26.

4. Terink, W., Immerzeel, W.W., Droogers, P., **2013**. Climate change projections of precipitation and reference evapotranspiration for the Middle East and Northern Africa until 2050. *Int. J. Clim.*, https://doi.org/10.1002/joc.3650.

5. Harbouze, R., Pellissier, J-P., Rolland, J-P., Khechimi, W., **2019**. Rapport de synthèse sur l'agriculture au Maroc. *CIHEAM-IAMM (research report in French)*. pp.104. ⟨hal-02137637v2⟩

6. Werz, M., Conley, L., **2012**. Climate Change, Migration, and Conflict in Northwest Africa. Rising dangers and policy options across the arc of tension. Heinrich Boll Stiftung, Center for Amirican Progress, report, 84p.

7. Desmidt, S., **2021**. Climate change and security in North Africa. Focus on Algeria, Morocco and Tunisia. *Cascades*, 1-44.

8. Beysens, D., Milimouk, I., **2001**. The case for alternative fresh water sources (in French). Science Et Changements planétaires/*Sécheresse* 11 (4), 281–288.

9. Monteith, J.L., **1957**. Dew. *Q. J. R. Meteorol. Soc*. 83 (357), 322–341.

10. Beysens, D., Dew water. **2018**, book, River Publishers, 200p.

11. Lekouch, I., Lekouch, K., Muselli, M., Mongruel, A., Kabbachi, B., Beysens, D., **2012**. Rooftop dew, fog and rain collection in southwest Morocco and predictive dew modeling using neural networks. *J. Hydrol*., 448-449, 60-72.

12. Beysens, D., **2016**. Estimating dew yield worldwide from a few meteo data. *Atmos. Res*., 167, 146–155.

13. Nakicenovic, N., Swart, R., **2000**. *GIEC, Special Report on Emissions Scenarios*. (Eds.), Cambridge University Press, UK. 570p.

14. Moss, R.H., Edmonds, J.A., Hibbard, K.A., Manning, M.R., Rose, S.K., Van Vuuren, D.P., Kram, T., **2010**. The next generation of scenarios for climate change research and assessment. *Nature* 463 (7282), 747–756.

15. Van Vuuren, D.P., Edmonds, J., Kainuma, M., Riahi, K., Thomson, A., **2011**. The Representative Concentration Pathways: an overview. *Clim. Change*, 109, 5-31.

16. Taylor, K.E., Stouffer, R.J., Meehl, G.A., **2012**. An overview of CMIP5 and the experiment design. *Bull. Am. Meteorol. Soc*. 93 (4), 485–498.

17. ECMWF, **2021**. https://cds.climate.copernicus.eu/cdsapp#!/dataset/projections-cordex-domains-single-levels?tab=overview

18. Lekouch, I., Muselli, M., Kabbachi, B., Ouazzani, J., Melnytchouk-milimouk, I., Beysens, D., **2011**. Dew, fog, and rain as supplementary sources of water in south-western Morocco. *Energy*, 36, 2257-2265.

19. Beck, H.E., Zimmermann, N.E., McVicar, T.R., Vergopolan, N., Berg, A., Wood, E.F., **2018**. Present and future Köppen-Geiger climate classification maps at 1-km resolution. *Scientific data*, 5, 180214.

20. Zeroual, A., Assani, A., Meddi, M., Alkama, R., **2019**. Assessment of climate change in Algeria from 1951 to 2098 using the Köppen–Geiger climate classification schem. *Climate Dynamics*, DOI: 10.1007/s00382-018-4128-0.

21. Pal Arya, S., **1988**. Introduction to Micrometeorology. *Acad. Press*, San Diego, 307p.

22. Weather Underground database, **2021**, https://www.wunderground.com (accessed on 13 February 2021)

23. NOAA. **2022a**. Available online: https://www.forecast.weather.gov (accessed on 13 February 2021).

24. Muselli, M., Clus, O., Ortega, P. Milimouk, I., Beysens, D., **2020**. Physical, chemical and biological characteristics of dew and rain water during the dry oceans on of tropical islands. *Atmos*., 12, 69.

25. Météociel database, **2021**. https://www.meteociel.fr (accessed on 13 February 2021)

26. Trosseille, J., Mongruel, A., Royon, L., Beysens, D., **2022**. Effective surface emissivity during dew water condensation. *Int. J. Heat and Mass Transf*. 183, 122078.

27. Tomaszkiewicz, M., Najm, A., Beysens, D., Alameddine, I., Zeid, EB, El-Fadel, M., **2016**. Projected climate change impacts upon dew yield in the Mediterranean basin. *Sci. Total. Environ*., 566-567, 1339-1348.

28. Martinez, W.A., Melo, C.E., Melo, O.O., **2017**. Median Polish Kriging for space–time analysis of precipitation. Spat. Stat., 19, 1-20.

29. Pue, J.D., Botula, Y.D., Nguyen, P.M., Meirvenne, M.V., Cornelis, W.M., **2021**. Introducing a Kriging-based Gaussian Process approach in pedotransfer functions: Evaluation for the prediction of soil water retention with temperate and tropical datasets. *J. Hydrol.*, 597, 125770.

30. Muselli, M., Beysens, D. **2021**. Mapping past, present and future dew and rain water resources for biocrust evolution in southern Africa. *J. Hydrol. and hydromechanics*, 69, 4, 400-420.

31. Amani, A., Lebel, T., **1997**. Lagrangian Kriging for the estimation of Sahelian rainfall at small time steps. *J. Hydrol*., 192, 125-157.

32. Lima, C.H.R., Kwon, H.H., Kim, Y.T., **2021**. A Bayesian Kriging model applied for spatial downscaling of daily rainfall from GCMs. *J. Hydrol*., 597, 126095.

33. Turc, L. **1961**. Evaluation des besoins en eau d'irrigation, évapotranspiration potentielle. *Annales agronomiques*, 12 (I), p. 13-49 (in French).

34. Rawls, W. J., Brakensiek, D. L., Saxton, K. E., **1982**. Estimation of soil water properties, *Trans. ASAE*, 25, 1316–1320, p. 1328.

35. El Mansouri, B., **2004**. Calcul de la réserve utile des sols pour une gestion rationnelle des eaux de l'irrigation. Recherche et Développement en Gestion Intégrée des Ressources Hydriques au Sud-Est du Maroc, Conférence internationale, Ouarzazate, Maroc.

36. Aoubouazza, M., **2017**. Influence des propriétés hydrodynamiques du sol sur la sensibilité au dépérissement du cèdre dans le causse moyen-atlasique central marocain. *Rev. Mar. Sci. Agron. Vét.*, 5 (3), 293-303.

37. Infoclimat, **2021**. https://www.infoclimat.fr/.

38. MarocMétéo, **2021**. Etat du climate en 2020 (in French). Report of the Equipment, transport, logistic and water Minister.

39. Sebbar, A., Hsaine, M., Fougrache, H., Saloui, A., Badri, W., **2020**. Impact du changement climatique sur la région montagneuse du moyen Atlas au Maroc. XXXIII^{ème} Colloque de l'Association Internationale de Climatologie, Rennes (France), 619-624.

40. Driouech, F., **2010**. Distribution des précipitations hivernales sur le Maroc dans le cadre d'un changement climatique : descente d'échelle et incertitudes. PhD, Institut National Polytechnique de Toulouse.

41. Khomsi, K., Mahe, G., Tramblay, Y., Sinan, M., Snoussi, M., **2015**. Trends in rainfall and temperature extremes in Morocco. *Nat. Hazards Earth Syst. Sci. Discuss*., 3, 1175–1201.

42. Agoumi, A., Debbarh, A., **2005**. Ressources en eau et bassins versants du Maroc : 50 ans de développement (1955-2005). In 50 ans de développement humain et perspectives 2025 : Cadre naturel, environnement et territoires. 9-58.

43. Douville, H., Ribes, A., Decharme, B., Alkama, R., Sheffield, J., **2013**. Anthropogenic influence on multidecadal changes in reconstructed global evapotranspiration. *Nat. Clim. Change*, 3, 59–62.

44. Bartholomeus, R.P., Stagge, J.H., Tallaksen, L.M., Witte, J.P.M., **2015**. Sensitivity of potential evaporation estimates to 100 years of climate variability. *Hydrol. Earth Syst. Sci*. 19, 997–1014.

45. Büdel, B., Darienko, T., Deutschewitz, K., Dojani, S., Friedl, S., Mohr, K.I., Salisch, M., Reisser, W., Weber, B. **2009**. Southern African biological soil crusts are ubiquitous and highly diverse in drylands, being restricted by rainfall frequency. Microb. Ecol., 57:229–247.

46. Raggio, J., Green, A., Pintado, A., Sancho, L.G., Büdel, B., **2021**. Functional performance of biocrust across Europe and its implications for drylands. *J. Arid Environ*., 186, 104402.

47. Pan, Y., Wan, X., Zhang, Y., **2010**. Dew formation characteristics in a revegetation-stabilized desert ecosystem in Shapotou area, northern China. *J. Hydrol*., 387, 265–272.

48. Li, S., Bowker, M.A., Xiao, B., **2021a**. Biocrust enhance non rainfall water deposition and alter its distribution in dryland soils. *J. Hydrol*., 595, 126050.

49. Li, S., Xiao, B., Kidron, G.J., **2021b**. Moss-dominated biocrust enhance water vapor sorption capacity of surface soil and increase non-rainfall water deposition in drylands. *Geoderma* 388, 114930.

50. Zhuang, Y., Zhao, W., **2017**. Dew formation and its variation in Haloxylon ammodendron plantations at the edge of a desert oasis, northwestern China. *Agric. For. Meteorol*., 247, 541–550.

51. Kidron, G.J., **2019**. The enigmatic absence of cyanobacterial biocrust from the Namib fog belt: Do dew and fog hold the key? *Flora*, 257, 151416.

52. Lekouch, I., Muselli, M., Melnytchouk-milimouk, I., Beysens, D., **2021**. *Private communication*.

53. Nilsson, T., Vargas, W.E., Niklasson, G.A., Granqvist, C.G., **1994**. Condensation of water by radiative cooling. *Renewable Energy* 5, 310 - 317.

54. Nilsson, T., **1996**. Initial experiments on dew collection in Sweden and Tanzania. *Sol. En. Mat. Solar Cells* 40, 23-32.

55. OPUR, **2021**. Organisation pour l'Utilisation de la Rosée. www.opur.fr

56. Olive, P., Dassargues, A., Grière, O., Ruthy, I., El Youbi, A., **2006**. Caractérisation isotopique des eaux de granite et de l'auréole métamorphique d'Oulmès (Maroc central). Integrated Water Resources management and Challenges of the Sustainable Development, GIRE3D: International Congress on Integrated Water Resources management and Challenges of the Sustainable Development, http://hdl.handle.net/2268/3459.

57. WHO, **2017**. WHO Guidelines for drinking-water quality (GDWQ).

58. WHO, **2022**. WHO Guidelines for drinking-water quality (GDWQ).

59. Chang, T.Y., Kuntasal, G., Pierson, W.R. **1986**. Night-time N2O5/NO3 chemistry and nitrate in dew water", *Atmos. Environ*., 21, 1345–1351.

60. Beysens, D., Ohayon, C., Muselli, M., Clus, O. **2006**. Chemical and biological characteristics of dew and rain water in an urban coastal area (Bordeaux, France). *Atmos. Environ*., 40, 3710-3723.

61. Draxler, R.R., Rolph, G.D. **2010**. HYSPLIT (HYbrid Single-Particle Lafrangian Integrated Trajectory) Model, access via http://www.arl.noaa.gov/ready/hysplit4.html.

62. NOAA. **2022b**. http://www.arl.noaa.gov/ (accessed on April 2022)

63. Goovaerts, P., **1997**. Geostatistics for natural resources evaluation. *Oxford university press*, New York, 500p.

64. Bargaoui, Z., Chebbi, A., **2009**. Comparison of two Kriging interpolation methods applied to spatiotemporal rainfall. *J. Hydrol*., 365, 56-73.

 doi:10.20944/preprints202210.0357.v1

65. Lepioufle, J.M., Leblois, E., Creutin, J.D., **2012**. Variography of rainfall accumulation in presence of advection. *J. Hydrol*., 464-465, 494-504.

66. Van de Beek, C.Z., Leijnse, H., Torfs, P.J.J.F., Uijlenhoet, R., **2012**. Seasonal semi-variance of Dutch rainfall at hourly to daily scales. *Adv. Water Resour*., 45, 76-85.

67. Rahmawati, N., **2020**. Space-time variogram for daily rainfall estimates using rain gauges and satellite data in mountainous tropical Island of Bali, Indonesia (Preliminary Study). *J. Hydrol*., 590, 125177.

Appendix A – The Kriging method

Kriging is a stochastic spatial interpolation method which predicts the value of a natural phenomenon at non-sampled sites by an unbiased, minimal variance linear combination of observations of the phenomenon at nearby sites. The Kriging tool assumes that the distance or direction between the sample points reflects a spatial correlation that can explain the surface variations. The Kriging tool applies a mathematical function to all points, or certain determined points, located within a specific radius. It determines the output value of each location.

The Kriging tool is particularly suitable for cases where it is known that there is a spatial correlation of distance or a directional deviation in the data. Kriging deduces, by weighting existing readings, the probable values of unmeasured locations. To calculate the interpolated data $\hat{Z}(s_0)$ at a specific location s_0, the general formula of ordinary Kriging (OK) method consists of a weighted sum of the data [63]:

$$\hat{Z}(s_0) = \sum_{i=1}^{P} \lambda_i Z(s_i)$$

Here $Z(s_i)$ corresponds to the measured value at the i^{th} location, λ_i the ponderation coefficient to determine and relate to the i^{th} location, s_0 the predicted location and p the number of measured data.

With the Kriging method, the λ_i weighted coefficients are not only based on the distance between the surveyed points and the forecast location, but also on the general spatial organization of the surveyed points. To use the spatial arrangement in the weighing, the spatial autocorrelation is quantified. Thus, in ordinary Kriging, the weighting λ_i depends on the distance from the forecast location and the spatial relationships between the values recorded around it.

The experimental semi-variogram can be estimated from point pairs:

Preprints (www.preprints.org) | NOT PEER-REVIEWED | Posted: 24 October 2022 doi:10.20944/preprints202210.0357.v1

$$\hat{\gamma}(h) = \frac{1}{2n(h)} \sum_{i=1}^{n(h)} [Z(s_i) - Z(s_i + h)]^2$$

Where

$$n(h) = Card\{(s_i, s_j) / |s_i - s_j| \approx h\}$$

with *Card* representing the number of elements for the given condition.

Classically, estimated semi-variogram are fitted by a spherical variogram model as proposed in previous studies on rainfall spatial estimation [64-67].

When the coordinates of the ground weather stations (e.g. Mirleft or Id Ouasskssou) do not correspond exactly to a kriging point, we have considered the nearest grid point to determine the estimated values.

Preprints (www.preprints.org) | NOT PEER-REVIEWED | Posted: 24 October 2022 doi:10.20944/preprints202210.0357.v1

Supplementary materials

SM1: Yearly summed values of dew and rain with their ratio

Fig. SM1 shows in a semi-log plot the yearly summed values of dew and rain with their ratio for the studied sites, except Gran Canaria, Casablanca and Al-Hoceima, reported in Fig. 9.

RCP 2.6 RCP 8.5

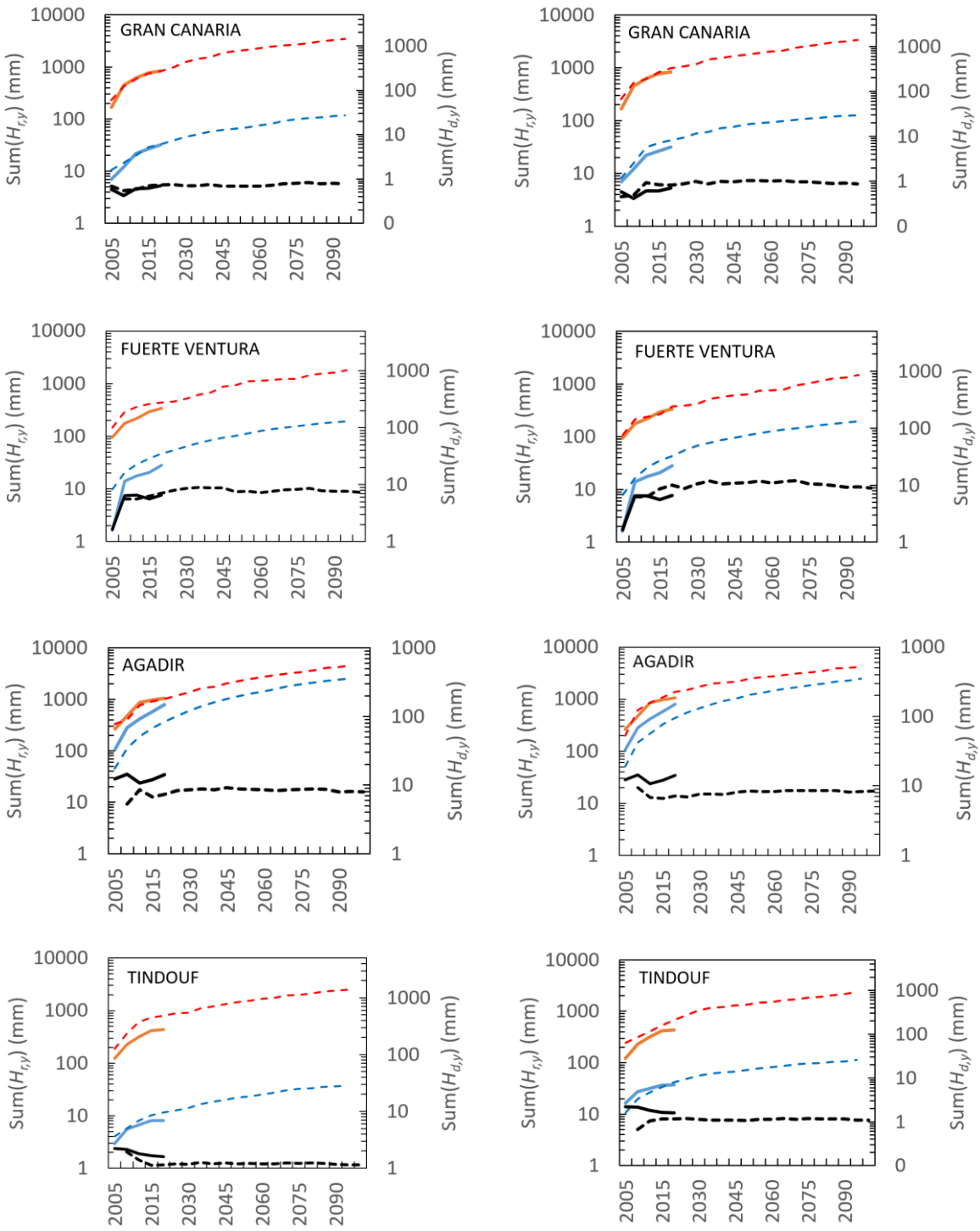

Preprints (www.preprints.org) | NOT PEER-REVIEWED | Posted: 24 October 2022 doi:10.20944/preprints202210.0357.v1

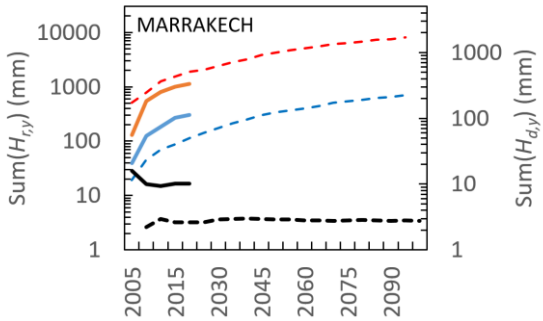

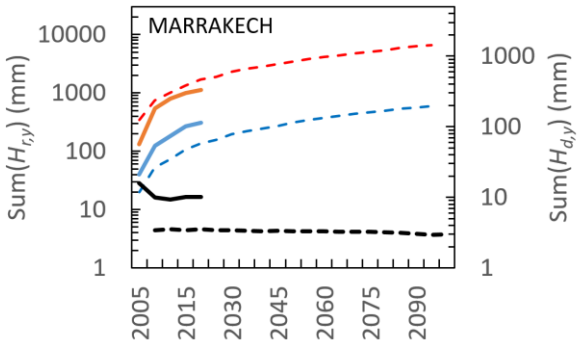

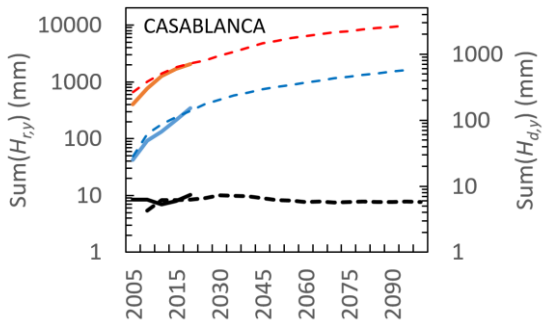

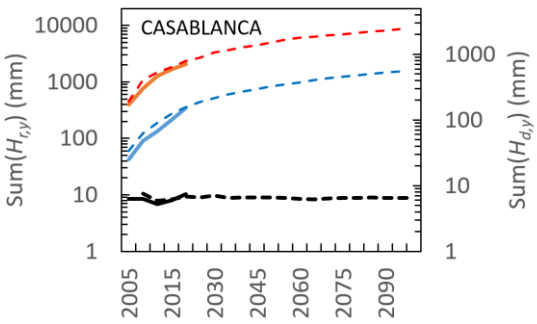

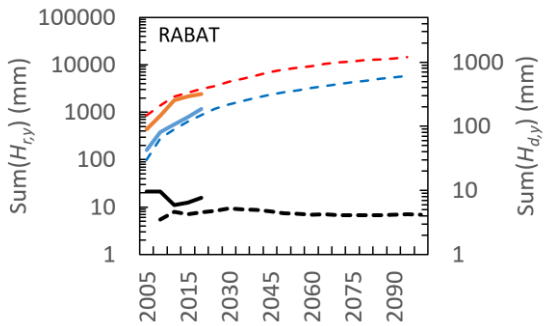

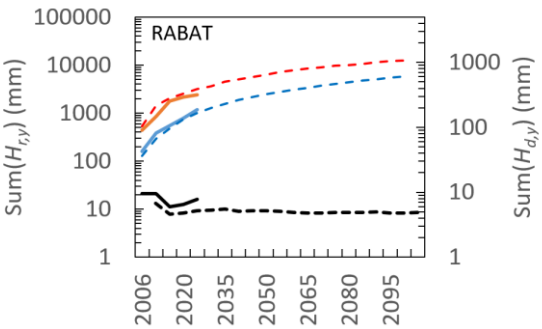

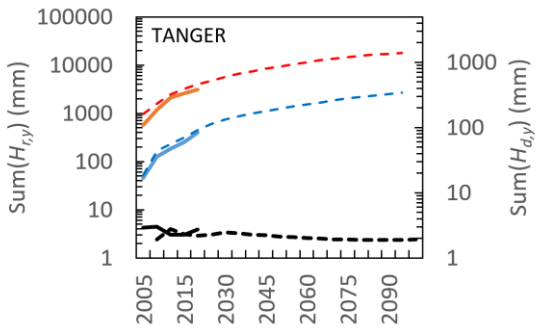

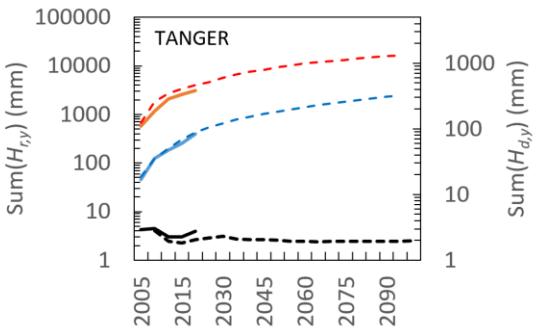

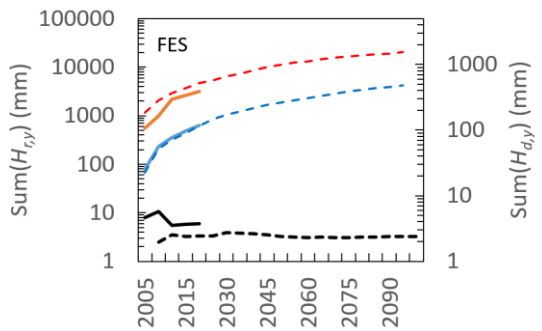

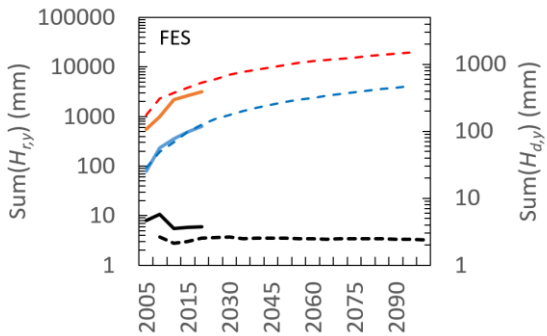

Preprints (www.preprints.org) | NOT PEER-REVIEWED | Posted: 24 October 2022 doi:10.20944/preprints202210.0357.v1

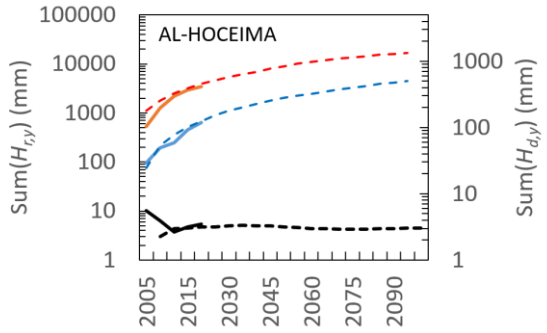

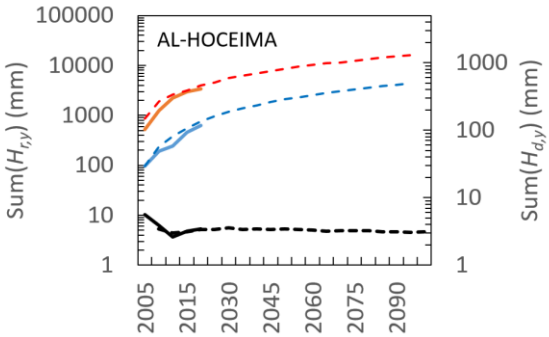

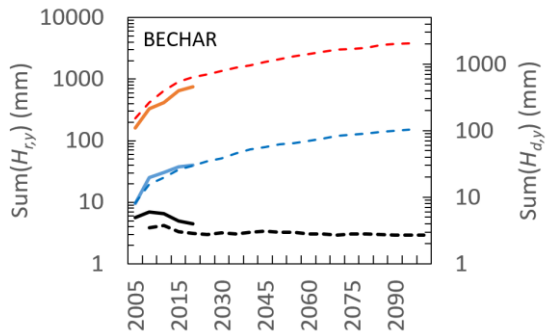

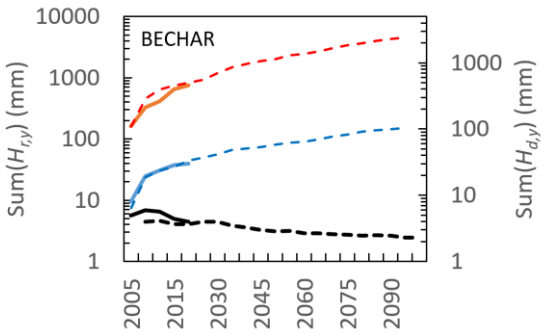

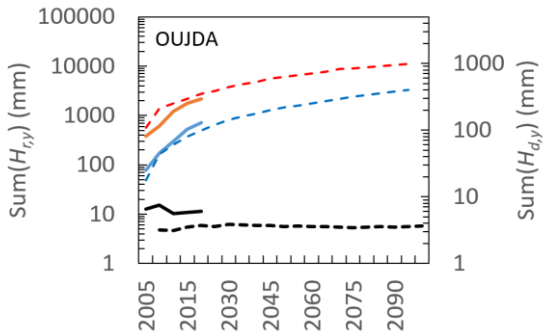

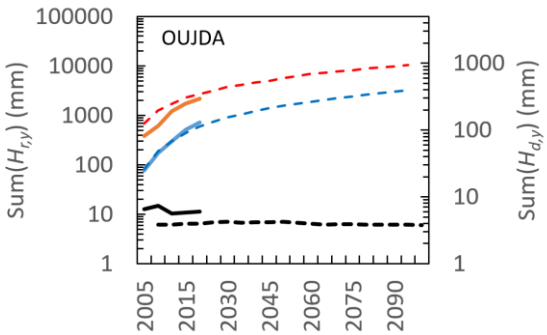

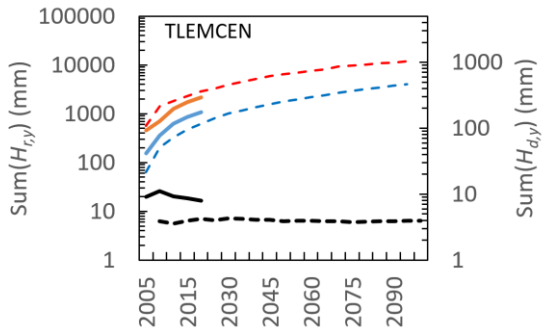

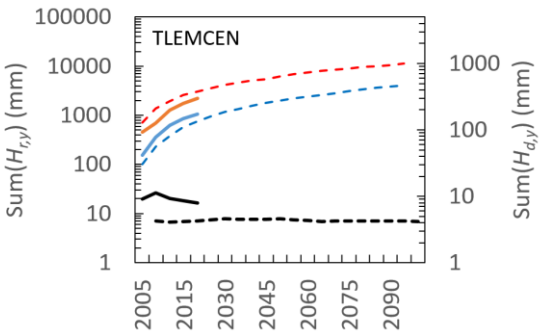

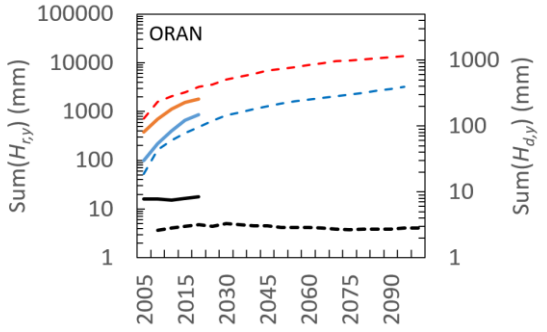

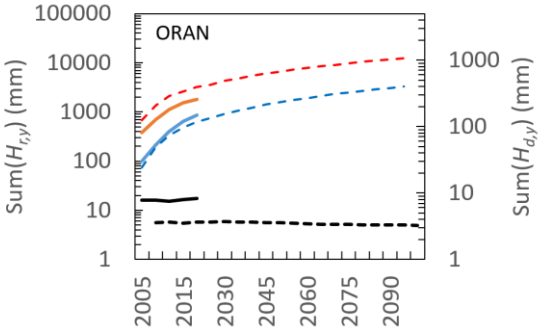

Preprints (www.preprints.org) | NOT PEER-REVIEWED | Posted: 24 October 2022 doi:10.20944/preprints202210.0357.v1

Figure SM1. Semi-log plot for the studied sites of yearly summed values for dew ($H_{d,y}$, blue, mm.yr^{-1}, right axis) and rain ($H_{r,y}$, red, mm.yr^{-1}, left axis) and ratio τ = sum($H_{d,y}$)/sum($H_{r,y}$) (black, dimensionless, right axis). The full curves correspond to the measured values (2005-2020), and the interrupted curves to predicted values (2006-2100) according to scenarios RCP 2.6 (left figures) and RCP 8.5 (right figures).

Preprints (www.preprints.org) | NOT PEER-REVIEWED | Posted: 24 October 2022 doi:10.20944/preprints202210.0357.v1

SM2: Evolution of the ratio potential evapotranspiration / dew yield

Figure SM2 shows the ratio of monthly potential evapotranspiration *PET* to monthly dew yields $H_{d,i}$,), PET / $H_{d,i}$, for years 2025, 2050, 2075, 2100 according to the projections of the climate models RCP 2.6 and RCP 8.5. The study is concerned with the driest period, April to October.

April

RCP 2.6			
2025	2050	2075	2100
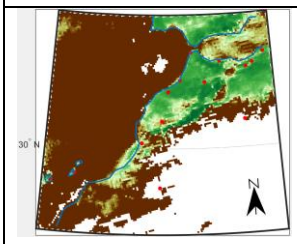	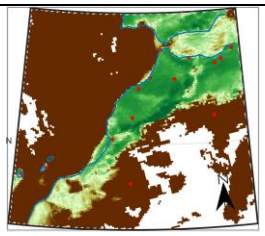	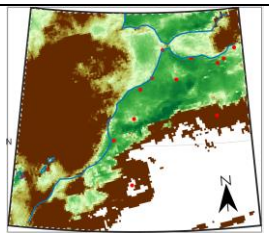	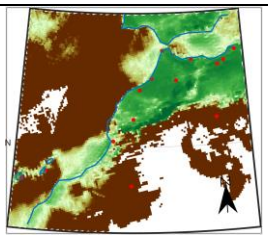
RCP 8.5			
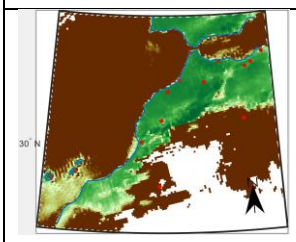	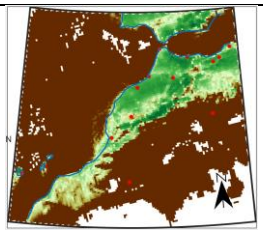	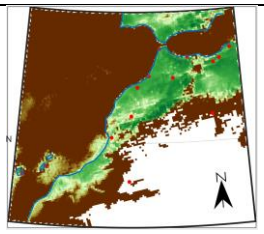	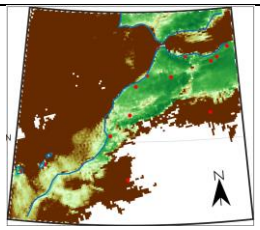

May

RCP 2.6			
2025	2050	2075	2100
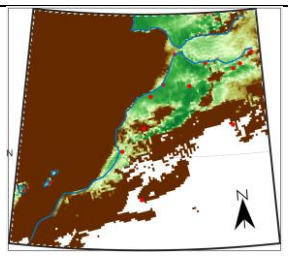	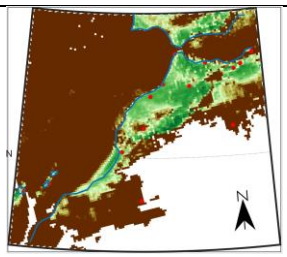	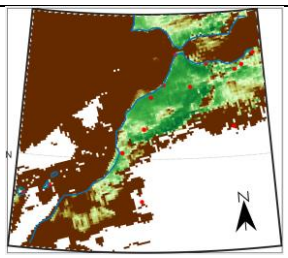	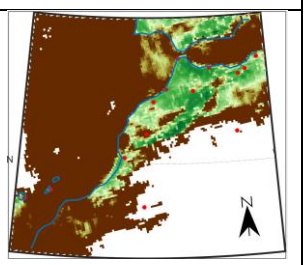
RCP 8.5			

Preprints (www.preprints.org) | NOT PEER-REVIEWED | Posted: 24 October 2022 doi:10.20944/preprints202210.0357.v1

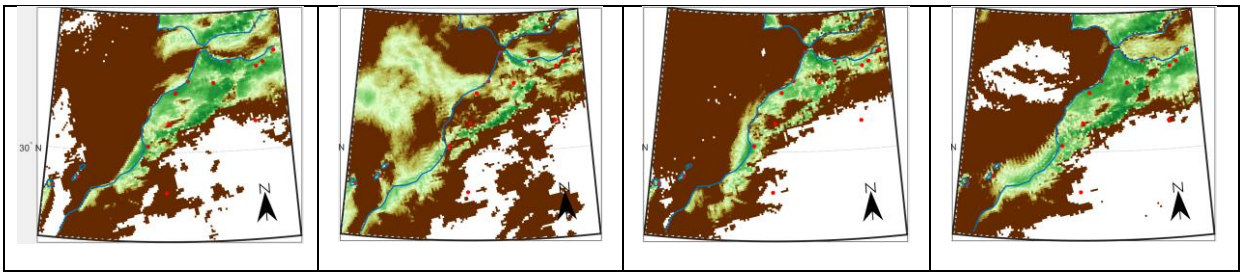

June

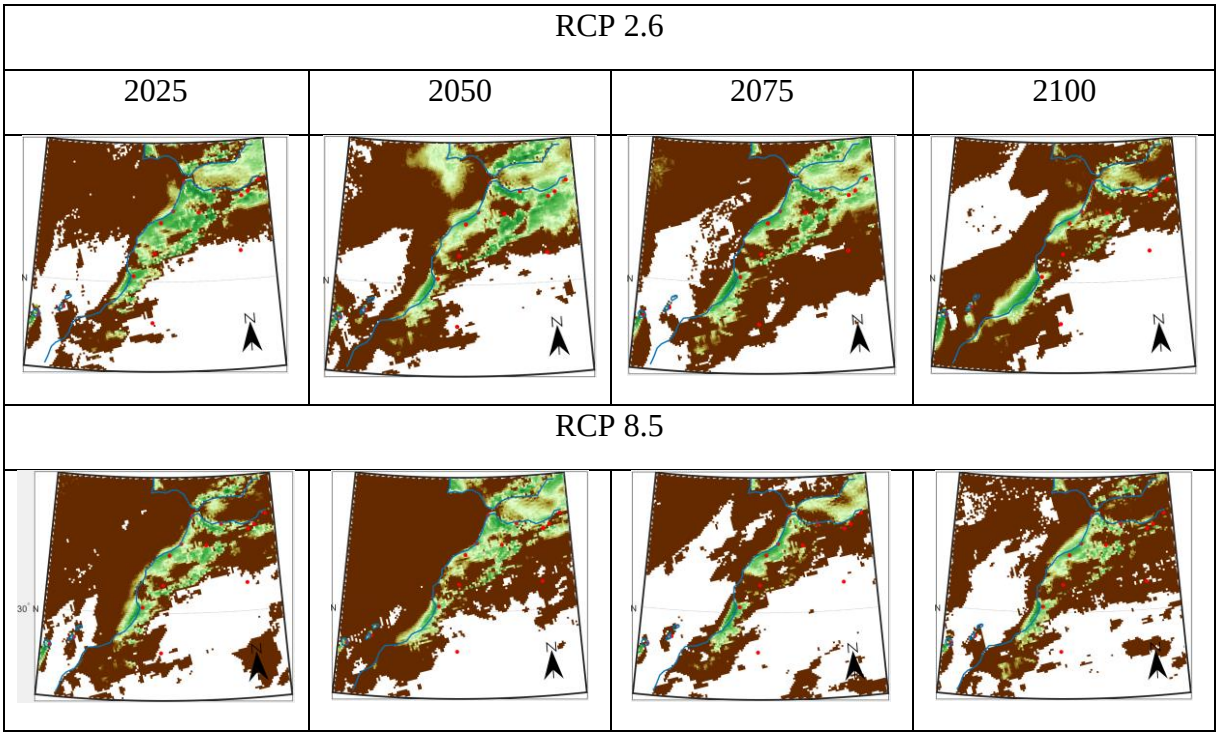

July

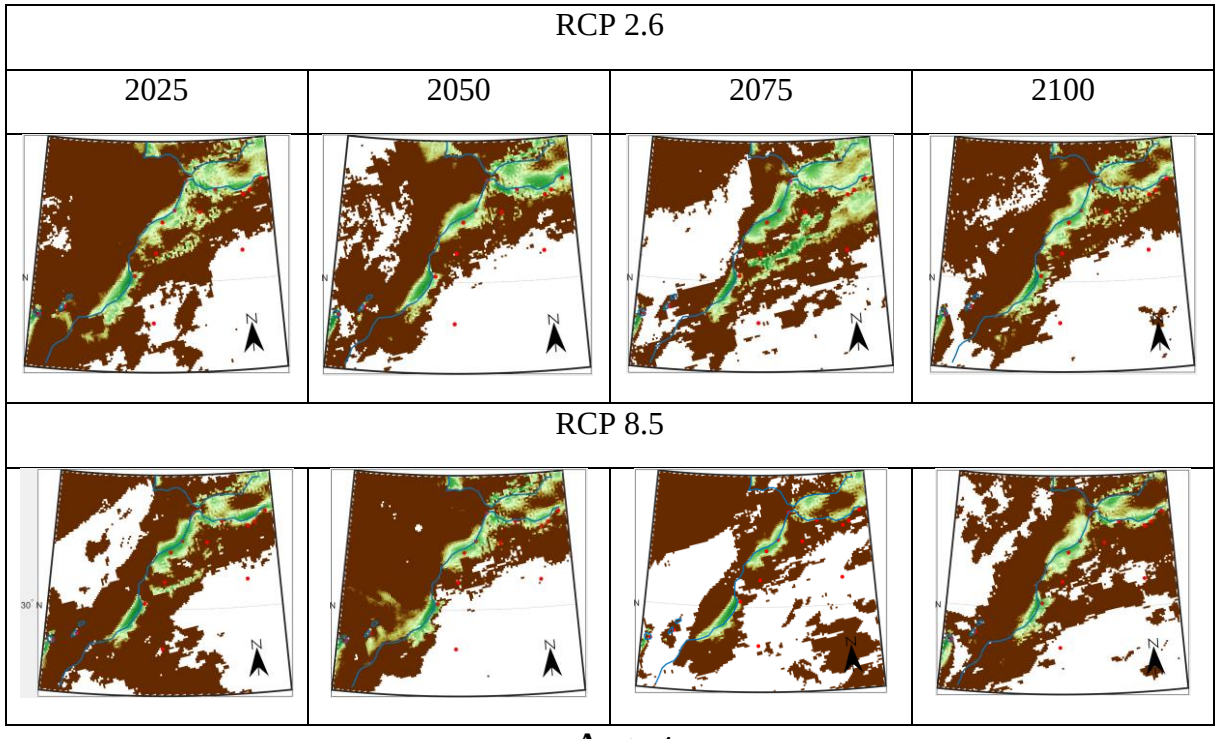

August

Preprints (www.preprints.org) | NOT PEER-REVIEWED | Posted: 24 October 2022 doi:10.20944/preprints202210.0357.v1

RCP 2.6			
2025	2050	2075	2100
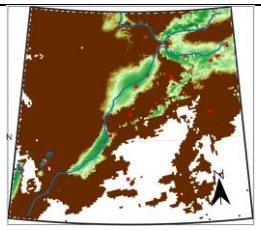	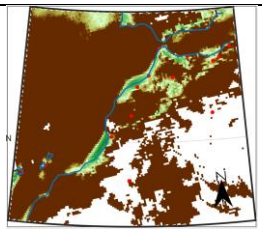	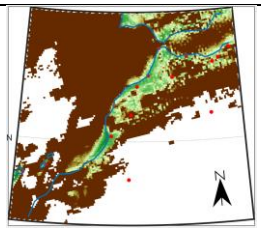	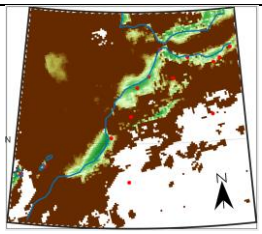
RCP 8.5			
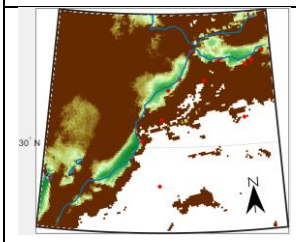	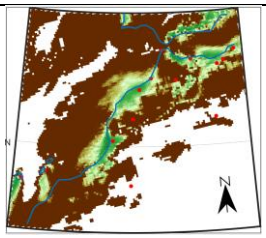	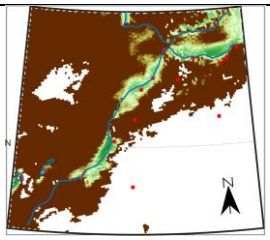	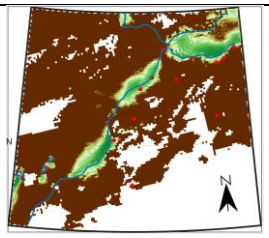

September

RCP 2.6			
2025	2050	2075	2100
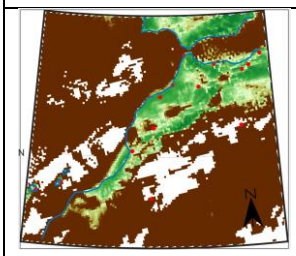	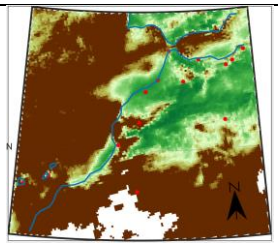	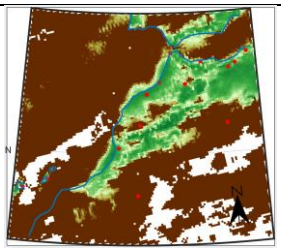	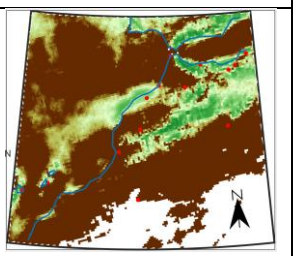
RCP 8.5			
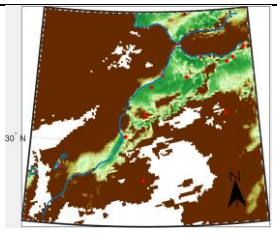	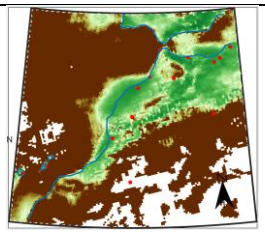	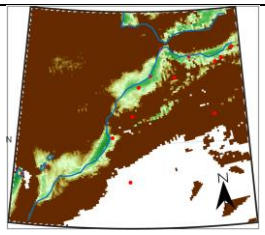	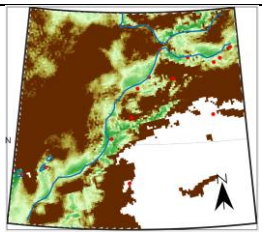

October

RCP 2.6			
2025	2050	2075	2100

Preprints (www.preprints.org) | NOT PEER-REVIEWED | Posted: 24 October 2022 doi:10.20944/preprints202210.0357.v1

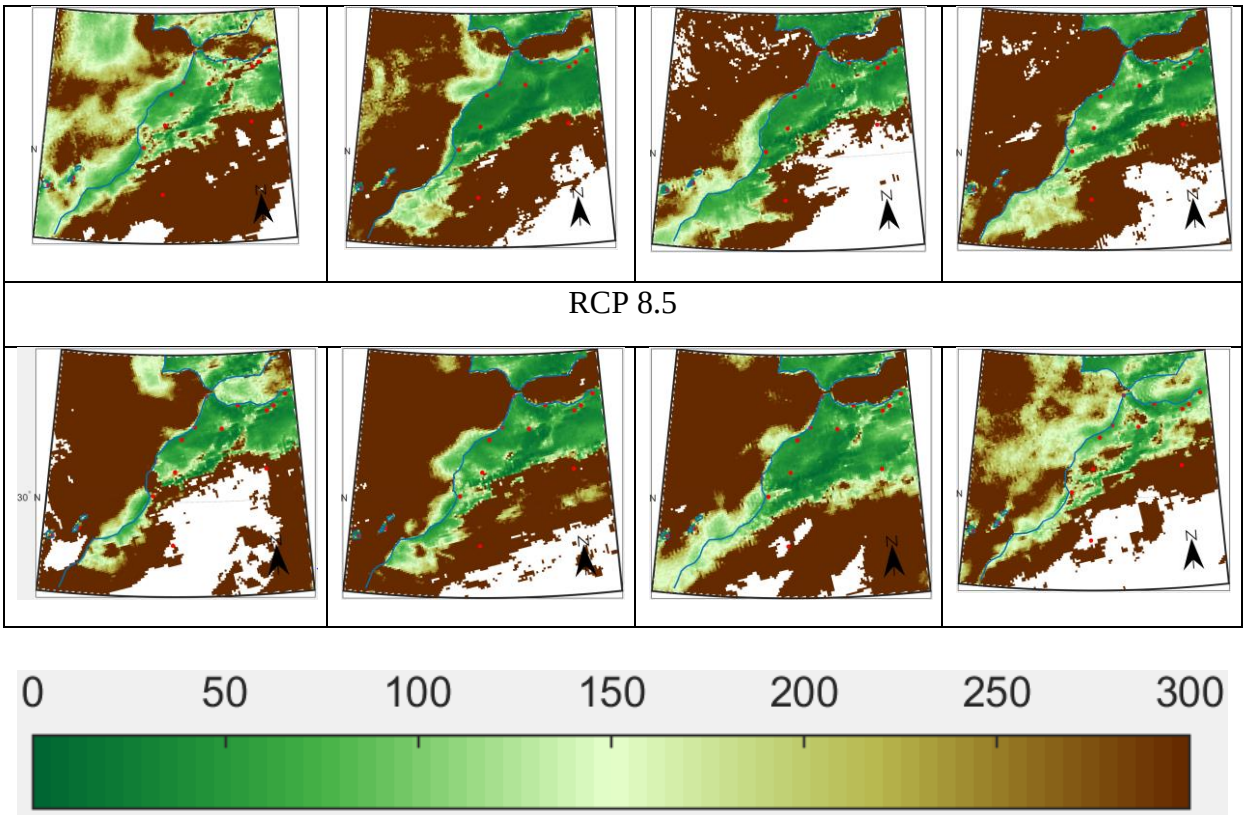

Figure SM2. Ratio PET / $H_{d,i}$ of monthly potential evapotranspiration PET (mm) to monthly dew yields $H_{d,i}$, (mm) for 4 specific years (2025, 2050, 2075, 2100) according to RCP 2.6 and 8.5 scenarios. The study considers data in the driest period (April to October). The white pixels mainly located S and SW correspond to $H_{d,i}$ = 0 mm, so $PET/H_{d,i} \rightarrow \infty$. The resolution is 12.5 × 12.5 km². Red points: airport stations described in Table 1 and Fig.1.